University of Nevada, Reno

Active Faulting in the Northern Walker Lane and Post-Earthquake Reconnaissance in the Central Walker Lane, Nevada and Eastern California

A dissertation submitted in partial fulfillment of the requirements for the degree of
Doctor of Philosophy in Geology

by

Conni L. De Masi

Richard D. Koehler/Dissertation Advisor

December 2021

THE GRADUATE SCHOOL

We recommend that the dissertation
prepared under our supervision by

Conni L. De Masi

entitled

Active Faulting in the Northern Walker Lane and Post-Earthquake Reconnaissance in the Central Walker Lane, Nevada and Eastern California

be accepted in partial fulfillment of the
requirements for the degree of

Doctor of Philosophy

Richard D. Koehler, Ph.D.
Advisor

Amanda Keen-Zebert, Ph.D.
Committee Member

Kenneth D. Adams, Ph.D.
Committee Member

Paula Noble, Ph.D.
Committee Member

Adam Csank, Ph.D.
Graduate School Representative

David W. Zeh, Ph.D., Dean
Graduate School

December, 2021

ABSTRACT

The Walker Lane is a region of diverse tectonic activity situated along the Pacific-North American plate boundary. Unmapped and under characterized faults within the northern Walker Lane are associated with large uncertainties in the location and frequency of potential earthquakes in the greater Reno, Nevada metropolitan area. Mapping of primary and secondary earthquake features in post-event studies help understand the location of faulting and amount of damage associated with earthquakes in the central Walker Lane.

Two fault systems in the northern Walker Lane are the Petersen Mountain fault located in the North Valleys region of Reno, and the Bonham Ranch fault in the Smoke Creek Desert of Pleistocene Lake Lahontan in the northern Walker Lane. A paleoseismic trench was excavated across the Petersen Mountain fault to document evidence for faulting and determine the timing of earthquake events. Optically stimulated luminescence dating methods were applied to faulted alluvial fan deposits exposed in the trench. For the Bonham Ranch fault, Uncrewed Aerial Vehicle (UAV) flight surveys were conducted in three locations to investigate differences between topographic scarps formed by tectonic displacement and shoreline processes. Cross cutting relations between the different scarp types combined with stratigraphic observations from outcrops were used to assess the timing of tectonic displacement across the fault.

Additionally, UAV surveys were conducted during post-earthquake rapid response reconnaissance in the central Walker Lane immediately following the 15 May 2020 M6.4 Monte Cristo, Nevada and 8 July 2021 M6.0 Antelope Valley, California earthquakes. The drone flights assisted ground crews in determining where to look for

surface rupture, earthquake secondary effects, and associated damage. These data provided insight into the amount and style of surface deformation immediately following the earthquake events, and the locations of faulting in the central Walker Lane.

These studies help answer questions pertaining to the locations and effects of earthquakes in these regions. By incorporating UAV technology into tectonic studies, hi-res aerial images for mapping and Structure From Motion models can be created, and result in a permanent archive of post-earthquake surface damage as well as provide means to measure paleo and modern surface rupture offsets applicable to seismic hazard characterization.

To my family.

ACKNOWLEDGEMENTS

Several people have played an important role in my successful completion of this Ph.D. research. First, I would like to thank my advisor, Rich Koehler, who supported both my academic and professional adventures. Thank you for showing me the ropes on being a geomorphic surgeon, how to cut open the Earth and investigate the unknown below the surface in pursuit of understanding earthquake events. Also, thank you for letting me take over the drone, my photographic and video skills have been expanded to new heights. I also thank my committee members- Amanda Keen-Zebert from DRI, Ken Adams from DRI, Paula Noble from DGSE and Adam Csank from DG- for your support and suggestions during this process. I am especially grateful to Amanda for the years of stimulating discussion and guidance in and outside the OSL lab.

Thank you to Seth Dee from NBMG for assisting me in the paleoseismic trenches, and to Christina Neudorf from the Optically Stimulated Luminescence Lab at DRI. I have learned so much from both of you and our discussions. To my office mates over the years: Colin Chupik and CJ McNeil, thank you for distracting me in the Q-lab with wonderful conversations and assisting me in the field.

I thank the University of Nevada, Reno, the Nevada Bureau of Mines and Geology, the Desert Research Institute, the National Science Foundation, the Geological Society of America, and the Soroptimist Foundation of Truckee Meadows for a variety of funding opportunities that allowed me to pursue both research and professional development endeavors throughout my PhD.

I want to recognize that the land in which I conducted my research is the traditional homelands of the Numu (Northern Paiute), Wašiw (Washoe), and Newe (Western Shoshone); and the private property of the John Espil Sheep Company and Ripple Ranch. I appreciate the opportunity to learn on their territory. I also thank the California Department of Water Resources, Bureau of Land Management and National Forest Service for obtaining land use permits and sharing data.

Finally, I would like to thank my family and friends who supported me through it all. To Mom, Dad and Sister, I am very grateful to have had your encouragement all these years while pursuing my higher education. To my friends, you helped me keep going even though I doubted myself at times, thank you for the positive energy.

TABLE OF CONTENTS

ABSTRACT i

DEDICATION iii

ACKNOWLEDGEMENTS iv

LIST OF TABLES ix

LIST OF FIGURES x

INTRODUCTION 1
  Chapter 1 Summary 4
  Chapter 2 Summary 5
  Chapter 3 Summary 6
  References 7

CHAPTER 1: EARLY DEVELOPMENT OF STRIKE-SLIP FAULTING: PALEOSEISMIC STUDY ALONG THE PETERSEN MOUNTAIN FAULT, NORTHERN WALKER LANE, NEVADA 10
  Abstract 10
  1. Introduction 11
    1.1. Previous studies along the Petersen Mountain fault 14
  2. Methods 15
  3. Results 16
    3.1. Mapping observations, geometry and kinematics of faults 16
    3.2. Petersen Mountain trench site 18
    3.3. Trenching observations and stratigraphic framework 19
    3.4. Age of sediments 22
  4. Discussion 23
    4.1. Characteristics and timing of faulting 23
    4.2. Displacement across the Petersen Mountain Fault Zone and its role in the evolution of the northern Walker Lane 26
  5. Conclusions 28
  Acknowledgements 29
  References 30
  Figures 35
  Appendix A. Supplementary OSL data 51
  Appendix B. Supplementary trench data. 58

CHAPTER 2: DECIPHERING SHORELINES FROM SCARPS: FAULT TRACE MAPPING AND PALEOSEISMIC INVESTIGATION OF THE BONHAM RANCH FAULT ZONE, NORTH OF RENO, NEVADA 63
- Abstract 63
- 1. Introduction 64
- 2. Background 66
  - 2.1. Bonham Ranch fault 66
  - 2.2. Smoke Creek Desert 69
  - 2.3. Quaternary lake history of the Smoke Creek Desert 70
  - 2.3. Shoreline and fault scarp morphology 72
- 3. Methods 74
- 4. Results 75
  - 4.1. Drone models 75
  - 4.2. Scarp morphology 76
  - 4.3 Stratigraphy in Smoke Creek channel 77
- 5. Discussion 78
- 6. Conclusions 80
- Acknowledgements 80
- References 81
- Figures 87

CHAPTER 3: THE APPLICATION OF UNMANNED AERIAL SYSTEMS IN POST-EARTHQUAKE GROUND DEFORMATION SURVEYS: EXAMPLES FROM THE M6.4 MONTE CRISTO, NEVADA AND M6.0 ANTELOPE VALLEY, CALIFORNIA EARTHQUAKES 102
- Abstract 102
- 1. Introduction 103
- 2. Regional Tectonic Setting and Recent Earthquakes 104
  - 2.1. Central Walker Lane and The Mina Deflection 104
  - 2.2. Faults near Antelope Valley, California 106
  - 2.3. Monte Cristo Range Earthquake 107
  - 2.4 Antelope Valley Earthquake 108
- 3. Methods 109
- 4. Results 111
  - 4.1. 2020 Monte Cristo Range earthquake 111
  - 4.2. 2021 Antelope Valley earthquake 113
- 5. Discussion 115
- 6. Conclusions 117
- Acknowledgements 117
- References 118
- Figures 122

APPENDIX C: EXPANDED OSL METHODS AND RESULTS FROM THE PETERSEN MOUNTAIN FAULT PALEOSEISMIC TRENCH STUDY FROM CHAPTER 1. 146
  1. Introduction and Background 147
  2. Methods 148
    2.1. Field collection methods 148
    2.2. Laboratory procedure methods 148
    2.3. Analysis 149
    2.4. Age models 150
  3. Results 150
  4. Discussion and Conclusion 151
  Acknowledgements 152
  References 152
  Figures 157

FINAL SUMMARY, CONCLUSIONS AND RECOMMENDATIONS 167
  Summary 167
  Concluding Remarks 167
    Chapter 1 167
    Chapter 2 168
    Chapter 3 169

LIST OF TABLES

Chapter 1

Table 1. Sample data used to calculate dose rates and luminescence ages 50

Appendix A Table 1. SAR protocols applied in this study 52

Appendix B Table 1. Unit descriptions for stratigraphic deposits 61

Appendix B Table 2. Soil descriptions from the south wall of the trench 62

Appendix B Table 3. Orientations of faults and fractures.. 63

Chapter 3

Table 1. Monte Cristo Range Earthquake UAV survey... 145

Appendix C

Table C1. SAR protocols 165

Table C2. OSL age data 166

LIST OF FIGURES

Chapter 1

Figure 1. Regional hillshade map of the northern Walker Lane 35

Figure 2. Hillshade map of the North Valleys 37

Figure 3. Lidar shaded relief map of area showing major fault traces............................ 38

Figure 4. Detailed geologic map 39

Figure 5. Lidar hillshade map of the area around the paleoseismic trench site 41

Figure 6. Drone photography 42

Figure 7. Log of Petersen Mountain trench exposure 44

Figure 8. Photographs of soils in trench 46

Figure 9. Schematic models 48

Appendix A Figure A1. Graph of CAM age as a function of water content 53

Appendix A Figure A2. Weighted histogram and kernel density estimate plot 54

Appendix A Figure A3. Radial plot 56

Appendix B Figure B1. Log of Petersen Mountain north wall trench 58

Appendix B Figure B2. Enlarged trench photo orthomosaic of south wall 59

Chapter 2

Figure 1. Shaded relief map of the northern Walker Lane... 87

Figure 2. Satellite image of Smoke Creek Desert 88

Figure 3. Satellite image of Sheepshead Spring 89

Figure 4. Late Pleistocene highstands of Lake Lahontan 90

Figure 5. Satellite image with UAV mission flight sites 91

Figure 6. UAV flight mission site A models 92

Figure 7. UAV flight mission site B models 93

Figure 8. UAV flight mission site C models 94

Figure 9. UAV DTM for flight mission sites A and B 95

Figure 10. Scarp profiles from UAV sites A and B 96

Figure 11. UAV DTM for flight mission sites A and B 97

Figure 12. Scarp profiles from UAV sites C 98

Figure 13. Map of shorelines and faults in the Sheepshead Spring 99

Figure 14. Tephra layers found in Smoke Creek 100

Figure 15. Map of tephra localities along Smoke Creek 101

Chapter 3

Figure 1. Regional map of the Walker Lane 122

Figure 2. Shaded relief map of the Central Walker 123

Figure 3. Image of the ray cloud in Pix4D Mapper 125

Figure 4. Pix4D Mapper models 126

Figure 5. Digital Terrain Model of surface deformation 127

Figure 6. Slope and contour map 129

Figure 7. Drone image of surface rupture produced during earthquake 130

Figure 8. Field photos of fractures from the M6.5 Monte Cristo Range earthquake 131

Figure 9. UAV aerial view of surface deformation found along Highway 95 132

Figure 10. Field photos of radial fractures along Highway 95 134

Figure 11. UAV aerial images of liquefaction features 136

Figure 12. Evidence of surface movement in Mill Creek Canyon 138

Figure 13. Images of landslide in Mill Creek Canyon 140

Figure 14. Oblique view drone images of the “old landslide” 141

Figure 15. Images of freshly disturbed soil 143

Figure 16. Pictures taken along the dirt road that goes through the “old landslide” 144

Appendix C

Figure C1. Log of Petersen Mountain trench 157

Figure C2. Field photos of tube OSL collection 159

Figure C3. Field photos of block OSL collection 160

Figure C4. Lab procedures in red safelight 161

Figure C5. Dose recovery test graph 163

Figure C6. Dose response curve 164

Figure C7. KDE and radial plots 165

INTRODUCTION

In the Walker Lane, approximately 15-25% of the Pacific-North American plate boundary strain is accommodated east of the Sierra Nevada through a combination of normal oblique slip on the Sierra Nevada frontal fault system, dextral slip along northwest trending faults in the northern Walker Lane, and oblique normal slip on north trending faults along the western margin of the Basin and Range province (Faulds et al., 2005, Wesnousky, 2005; Hammond et al., 2011). However, timing and recurrence of past earthquakes along many faults the region is uncertain, contributing to uncertainties in seismic hazard models and assessment of seismic risk to regional communities.

North of Reno, Nevada dextral shear is transferred from the Sierra Nevada rangefront across a right step (through a region known as the North Valleys) to the Walker Lane defined by the left-stepping Pyramid, Warm Springs Valley, and Honey Lake faults. The North Valleys consist of a series of north-striking east dipping faults including the Last Chance, Petersen Mountain, Fred's Mountain, and Spanish Springs Valley faults. Geodetic studies indicate that up to 7 mm/yr of dextral shear is distributed across the northern Walker Lane (Hammond et al., 2011) in the vicinity of Reno decreasing to about 4-5 mm/yr near Honey Lake Valley (Bormann, 2013). Geodetic studies of the North Valleys estimate that north striking faults collectively accommodate 0.9-1.2 mm/yr of extension and <0.3 mm/yr of dextral slip (Bormann, 2013). Right oblique displacement has been documented along north-trending normal faults within the North Valleys, as well as along faults northeast of the Walker Lane including the Dry Valley-Smoke Creek, and Bonham Ranch fault zones (Weick, 1990; Bell and Ramelli, 2009; De Masi et al., 2021).

Studies along these faults of Pleistocene age help to provide constraints on the number, timing, and recurrence of late Pleistocene earthquakes. For the Pyramid Lake fault, Briggs et al. (2004) determined that at least four earthquakes have occurred since the desiccation of Lake Lahontan (~15 ka) using elevations of high stand shorelines, and recent trenching along the Warm Springs Valley fault, indicate the occurrence of three to four late Pleistocene earthquakes with an inferred recurrence of 2,500-3,000 yrs (Chupik et al., 2021). A study by Adams et al. (2008) compared spatial-temporal relationships between shoreline elevation records in the Lahontan basin to consider if lake-level fluctuations across the Pleistocene-Holocene controlled the distribution of archaeological sites, as fluctuating shorelines indicate a change in either climate or changes in rate of tectonics. While this body of research does not look at changes of shoreline elevations directly, a part of this research is to distinguish fault scarps from shorelines and to use known shoreline elevation highstands as age control for the timing of fault scarp formation.

The central Walker Lane, another region with frequent earthquakes in this study, is located south of Reno, NV and accommodates dextral shear between the eastern Sierra Nevada and westernmost Basin and Range provinces (Bennett et al., 1999). Geodetic measurements record ~7-8 mm/yr of northwest directed dextral shear (Hammond & Thatcher, 2007; Hammond et al., 2011). The central Walker Lane contains the Mina Deflection, an area of diffuse seismicity with earthquakes commonly occurring on left-lateral faults (Ryall and Priestly, 1975). The Mina Deflection is the location for the epicenter of the Monte Cristo Range earthquake, one of two earthquakes documented in this study. The Monte Cristo Range earthquake occurred within a spatial gap between major historical surface rupturing earthquakes to the northeast and south (Beanland and Clark, 1994; Bell et al., 1999). North of the Mina Deflection, near Topaz Lake, is the location for the Antelope Valley earthquake. The epicenter was located in a southwestern sub-basin of Antelope Valley, CA along the south end of Slinkard Valley fault, an east-dipping normal fault with a slip rate of ~.5 mm/yr (Pierce, 2019). The success of previous studies in obtaining slip rate and earthquake recurrence intervals has been motivation for the fault studies in this dissertation. Several other faults are within the 30 km-80 km seismic hazard zone within the Reno-Sparks metropolitan area (Andersen et al., 2018). Targeted faults addressed in this dissertation are the Petersen Mountain fault and Bonham Ranch fault. The Petersen Mountain and Bonham Ranch faults are located in fault zones that seem to exhibit both normal and transform motion, thus increasing our knowledge on where and when earthquakes occur and their role in the tectonic development of faulting in the northern Walker Lane region of the Pacific-North American Plate boundary.

Multiple methods were used to gather information for determining the earthquake history along the faults in this research. Field mapping, trenching methods, use of UAS, and OSL dating and relative dating methods were applied to the three projects that make up this body of work. The data acquired for this dissertation answers questions related to where and when earthquakes occur, the topographic and morphological differences between shorelines and fault scarps, and how this research can reduce the risk and toll of geohazards.

Chapter 1 Summary

Chapter 1 titled, "Early development of strike-slip faulting: Paleoseismic study along the Petersen Mountain fault, northern Walker Lane, Nevada", is a paleoseismic study that takes place in the northern Walker Lane. The Petersen Mountain fault is in the North Valleys region north of Reno, Nevada. It was previously mapped as a normal fault. Results from this study based on trenching indicate that alluvial fan and boulder deposits have been juxtaposed laterally along the fault. OSL dates indicate a difference in age for units on either side of the fault and place at least one earthquake as having occurred in the late Pleistocene. Work from this chapter was published and presented:

1. 2021: **De Masi, C**., Koheler., R., Dee., S., and Keen-Zebert, A., 2021, Early development of strike-slip faulting: Paleoseismic study along the Petersen Mountain fault, northern Walker Lane, Nevada, Journal of Quaternary Science. p 1-12.
2. 2019: Koehler, R.D., Dee, S., and **De Masi, C**., 2019, New Lidar Mapping and Paleoseismic Characterization of the Petersen Mountain Fault Zone, North of Reno, NV, Final Technical Report, U.S. Geological Survey National Earthquake Hazards Reduction Program (Award # G18AP00007).
3. 2019: **De Masi, C**., Koehler, R.D., Dee, S., Chupik, C., Castillo, C., Kleber, E., and Keen-Zebert, A., 2019, New observations on the paleoseismic history and sense of slip along the Petersen Mountain fault, north western Nevada. Presented at the Cordilleran section meeting of the Geological Society of America, Portland, OR, May 16, 2019.

4. 2019: **De Masi, C**., Koehler, R.D., Dee, S., Chupik, C., Castillo, C., and Kleber, E., 2019, Paleoseismic trench investigation of the Petersen Mountain fault, North Valleys-Reno, Nevada. Presented at the annual meeting of the Seismological Society of America, Seattle, WA, April 23-26, 2019.

Chapter 2 Summary

Chapter 2 is titled, "Deciphering shorelines from scarps: Drone modeling and paleoseismic investigation of the Bonham Ranch Fault Zone, North of Reno, Nevada". For this study, the types of landforms distributed along the Bonham Ranch fault were assessed to evaluate the timing of earthquakes, important for better understanding the faults earthquake potential. The Bonham Ranch fault is in the Smoke Creek Desert of Pleistocene Lake Lahontan in the northern Walker Lane, an area of active normal faulting. Several drone surveys were conducted along the fault to model and assess the origin of topographic scarps. Stratigraphic analysis with comparison studies were conducted to determine the differences between fault scarps and shoreline features such as wave-cut terraces. Previously reported ages associated with highstand levels of the paleoshorelines, cross cutting relations with faults, and tephra deposits were used to evaluate the timing of earthquakes. Based on these comparisons, there has been at least one earthquake along the Bonham Ranch fault that post-dates the Younger Dryas shoreline (~12 ka) and likely post-dates the Neopluvial period shorelines of mid-Holocene age. Work from this project was presented:

1. 2021: **De Masi, C**., and Koehler, R.D., 2021, Deciphering shorelines from scarps: Fault trace mapping and paleoseismic investigation of the Bonham Ranch Fault

Zone, North of Reno, Nevada. Presented at the Cordilleran Online section meeting of the Geological Society of America, Reno, NV, May 12th-14th, 2021.

2. 2021: **De Masi, C**., 2021, Unmanned Aerial Vehicle mapping and paleoseismic investigation of the Bonham Ranch Fault Zone, North of Reno, Nevada. Presented at the Association of Environmental and Engineering Geologists Great Basin Chapter Student Night Reno, NV, 8 April 2021.

Chapter 3 Summary

Chapter 3 is titled, "The application of Uncrewed Aerial Systems (UAS) in post-earthquake ground deformation surveys: Examples from the M6.4 Monte Cristo, Nevada and M6.0 Antelope Valley, California earthquakes". This chapter describes details on the use and application of UAS and UAVs in post-earthquake disaster rapid response surveying including drone flight mission specifications and model processing methods. Results from this chapter provide information on the amount and style of surface deformation with the use of UAV imagery and DTM models for the Monte Cristo Range earthquake, as well as the distribution of secondary effects found within a landslide from the Antelope Valley earthquake. Work from this project was incorporated into a regional rupture map compilation and published and presented:

1. 2021: *In review,* dePolo, C., and **De Masi, C**., Editor for volume Koehler, R.D., Photo-Documentation of the Damage and Effects Caused by the May 15, 2020 Monte Cristo Range, Nevada Earthquake, Nevada Bureau of Mines and Geology Special Publication.
2. 2021: *In progress for publication*, **De Masi, C**., and Koehler, R.D., The application of Unmanned Aerial Systems in post-earthquake ground deformation

surveys: Use of UAS for the M6.4 Monte Cristo, Nevada and M6.0 Antelope Valley, California earthquakes..Considering submission to online journal *Frontiers of Remote Sensing.*

3. 2021: Dee, S., Koehler, R.D., Elliott, A.J., Hatem, A.E., Pickering, A.J., Pierce, I., Seitz, G.G., Collett, C.M., Dawson, T.E., **De Masi, C**., dePolo, C.M., Hartshorn, E.J., Madugo, C.M., Trexler, C.C., Verdugo, D.M., Wesnousky, S.G., and Zachariasen, J., Surface Rupture Map of the 2020 M6.5 Monte Cristo Range earthquake, Esmeralda and Mineral counties, Nevada. Nevada Bureau of Mines and Geology Map 190, 2 sheets, scale 1:14,000, 26 p.
4. 2021: Motamed, R., Ryan, M., Lambeth, G., Toth, J., Parks, M., Garcia, F., Bassal, P.C., Pease, J., and Koehler, R.D., and **De Masi, C**., as contributor, 2021, Preliminary report on geotechnical aspects of the May 15th 2020 magnitude 6.5 Monte Cristo Range Earthquake in Nevada, Geotechnical Extreme Events Reconnaissance, Report GEER-71.

References

Adams, K. D, Goebel, T., Graf, K., Smith, G., Camp, A., Briggs, R., and Rhode, D., 2008, Late Pleistocene and Early Holocene lake-level fluctuations in the Lahontan Basin, Nevada: Implications for the distribution of archaeological sites. Geoarchaeology-an International Journal - GEOARCHAEOLOGY. 23. 608-643. 10.1002/gea.20237.

Anderson, J.G., Koehler, R.D., Abercrombie, R., Kamran Ahdi, S., Angster, S., Bormann, J., Brune, J.N., Dee, S.M., dePolo, C., Dickenson, S.E., Dunn, M., Faulds, J.E., Hammond, W.C., Hatch, R., Kell, A., Kent, G., Kreemer, C., Louie, J., Pierce, I., Ruhl, C.J., Smith, K.D., Taylor, W., Wesnousky, S.G., Wong, I.,; A Seismic Hazards Overview of the Urban Regions of Nevada: Recent Advancements and Research Directions. Seismological Research Letters; 90 (4): 1577–1583. doi: https://doi.org/10.1785/0220180357.

Angster, S., Huang, W., Wesnousky, S.G., Kent, G., Nakata, T. and Goto, H., 2014, Earthquake size and slip rate of the Pyramid Lake fault zone near Reno, Nevada, NEHRP Final Technical Report, G13AP00033, 22 p.

Beanland, S., and Clark, M.M., 1994, The Owens Valley fault zone, eastern California, and surface faulting associated with the 1872 earthquake: U.S. Geological Survey Bulletin 1982, 32 p.

Bell, J.W., dePolo, C.M., Ramelli, A.R., Sarna-Wojcicki, A.M., and Meyer, C.E., 1999, Surface faulting and paleoseismic history of the 1932 Cedar Mountain earthquake area, west-central Nevada, and implications for modern tectonics in the Walker Lane: Geological Society of America Bulletin, v. 111, p. 791–807.

Bell, J.W., and Ramelli, A.R., 2009, Active fault controls at high-temperature geothermal sites: Prospecting for new faults, GRC Transactions, vol. 33, p. 425-429.

Bormann, J., 2013, New insights into strain accumulation and reléase in the central and northern Walker Lane, Pacific-North American plate boundary, California and Nevada, USA, Ph.D. dissertation, August 2013, University of Nevada, Reno.

Briggs, R.W. and Wesnousky, S.G., 2004, Late Pleistocene fault slip rate, earthquake recurrence, and recency of slip along the Pyramid Lake fault zone, northern Walker Lane, United States: Journal of Geophysical Research-Solid Earth, v. 109, no. B8, 16 p.

Christenson, G.E., and Purcell, C., 1985, Correlation and age of Quaternary alluvial-fan sequences, Basin and Range province, southwestern United States, in Weide, D.L., ed., Soils and Quaternary Geology of the southwestern United States: Geological Society of America Special Paper 203, p. 115-122.

Chupik, C., Koehler, R., and Keen-Zebert, A., 2021, Complex Holocene Fault Ruptures on the Warm Springs Valley Fault in the Northern Walker Lane, Nevada–Northern California. Bulletin of the Seismological Society of America *2021*; doi:https://doi.org/10.1785/0120200271.

Dee, S., Ramelli, A.R., and Koehler, R.D., 2018, Pilot paleoseismic investigation of faults in the North Valleys, Reno, NV, Final Technical Report, U.S. Geological Survey National Earthquake Hazards Reduction Program (Award # G16AP00060).

De Masi, C., Koheler., R., Dee., S., and Keen-Zebert, A., 2021, Early development of strike-slip faulting: Paleoseismic study along the Petersen Mountain fault, northern Walker Lane, Nevada, Journal of Quaternary Science. Vol. 36, No. 3, p. 403-414.

Faulds, J.E., Henry, C.D., and Hinz, N.H., 2005, Kinematics of the northern Walker Lane: An incipient transform fault along the Pacific-North American plate boundary, Geology, 33, 505-508.

Gold, R.D., Briggs, R.W., Crone, A.J., DuRoss, C.D., 2017, Refining fault slip rates using multiple displaced terrace risers-An example from the Honey Lake fault, NE California, USA, Earthq and Planetary Science Letters, v. 477, p. 134-146.

Gold, R.D., dePolo, C.M., Briggs, R.W., Crone, A.J., and Gosse, J., 2013, Late Quaternary slip-rate variations along the Warm Springs Valley fault system, northern Walker Lane, California- Nevada border, Bulletin of the Seismological Society of America, v. 103, no 1, p. 542-558.

Hammond, W.C., Blewitt, G., and Kreemer, C., 2011, Block modeling of crustal deformation of the northern Walker Lane and Basin and Range from GPS velocities, J. Geophys. Res. B Solid Earth Planets 116, p. 1-28.

Koehler, R.D., 2018, Active faulting in the North Valleys region of Reno, Nevada: A distributed zone within the northern Walker Lane, Geomorphology special volume on paleoseismology, https://doi.org/10.1016/j.geomorph.2018.09.015

Laymon, C., Quattrochi, D., Malek, E., Hipps, L., Boettinger, J., McCurdy, G., 1998, Remotely-sensed regional-scale evapotranspiration of a semi-arid Great Basin desert and its relationship to geomorphology, soils, and vegetation, Geomorphology, Volume 21, Issues 3–4, p. 329-349.

Pierce, I., 2019, Active Faulting in the Central Walker Lane, Ph.D. dissertation, University of Nevada, Reno, 116 p.

Ryall, A.S., and Priestly, K., 1975, Seismicity, secular strain, and maximum magnitude in the Excelsior Mountains area, western Nevada and eastern California: Geological Society of America Bulletin, v. 86, p. 1585–1592.

Turner, R., Koehler, R.D., Briggs, R.W., and Wesnousky, S.G., 2008, Paleoseismic and slip-rate observations along the Honey Lake fault zone, northeastern California, Bulletin of the Seismological Society of America, 98, 4, 1730-1736.

Weick, 1990, Structural, tectonic, and Quaternary study of the eastern Madeline Plains, California and southwestern Smoke Creek Desert, Nevada, M.S. thesis, University of Nevada, Reno, 160 p., 5 plates.

Wesnousky, S.G., 2005, Active faulting in the Walker Lane, Tectonics, 24, TC3009.

Chapter 1

Early development of strike-slip faulting: Paleoseismic study along the Petersen Mountain fault, northern Walker Lane, Nevada

Conni De Masi[1], Rich Koehler[1], Seth Dee[1], and Amanda Keen-Zebert[2]

[1]University of Nevada Reno, Nevada Bureau of Mines and Geology, and [2]Desert Research Institute

Abstract

Characterizing youthful strike-slip fault systems within transtensional regimes is often complicated by the presence of tectonic geomorphic features produced by normal faulting associated with oblique extension. The Petersen Mountain fault in the northern Walker Lane tectonic province exhibits evidence of both normal and strike slip faulting. We present results of geologic and geomorphic mapping, and paleoseismic trenching that characterize the fault's style and sense of deformation. The fault consists of two major traces. The western trace displaces colluvial, landslide, and middle to late Pleistocene alluvial fans and is associated with aligned range front saddles, linear drainages, and oversteepened range front slopes. The eastern trace is associated with a low linear bedrock ridge, a narrow graben, right deflected stream channels, and scarps in late Pleistocene alluvial fan deposits. A trench on the eastern trace of the fault exposed a clear juxtaposition of disintegrated granodiorite bedrock against sand and boulder alluvial fan deposits across a steeply east dipping fault. The stratigraphic evidence supports the occurrence of at least one late Pleistocene earthquake with a component of lateral displacement. As such, the Petersen Mountain fault accommodates part of the ~7mm/yr of dextral shear distributed across the northern Walker Lane.

1. Introduction

The evolution of continental transform systems is complex due in part to inherited pre-existing structures and the partitioning of deformation on faults with various orientations and sense of motion (e.g. Peltzer and Tapponier, 1988; Wilcox et al., 1973). In California and western Nevada, both dip-slip and lateral motion is accommodated on faults within the San Andreas fault system (Castillo and Ellsworth, 1993; Kelsey and Carver, 1988; Hornafius et al., 1986), as well as the Walker Lane and Eastern California Shear Zone (Sturmer and Faulds, 2018; Dixon and Xie, 2018; Trexler, 2000; Faulds and Henry, 2008; Wesnousky, 2005a; 2005b; Schermer et al., 1996; Richard 1993). These studies highlight activity on variably oriented faults within regions of right-lateral shear. Wesnousky (2005b) attributed the relatively more complex, discontinuous and broader system of faults composing the Walker Lane to lower cumulative slip, as compared to the San Andreas fault, and a component of extensional motion. In a study of the 2013 M7.7 Balochistan, Pakistan earthquake, Barnhart et al. (2015) noted that slip was purely strike-slip along a dipping fault associated with tectonic geomorphic evidence of long-term reverse faulting. Based on these observations, Barnhart et al. (2015) proposed a bimodal slip model in which individual earthquakes may alternate between dip-slip and strike-slip kinematics. A fundamental question is whether strike-slip faulting can occur along dipping faults in transtentional environments (i.e. Walker Lane) and how this faulting contributes toward the kinematic evolution of youthful or incipient strike-slip fault systems. Do previously existing normal faults provide a pathway for lateral deformation? The Petersen Mountain fault in the northern Walker Lane is ideally located to examine these ideas given its location within a zone of many variably oriented faults within a region of right lateral shear.

The 25-km-long Petersen Mountain fault system bounds the eastern side of Petersen Mountain north of Reno, NV within the northern Walker Lane and extends from Cold Springs Valley in the south to Red Rock Valley in the north (Figures 1 and 2). The system consists of two subparallel traces (herein referred to as the Western and Eastern Petersen Mountain faults) which are part of a series of east dipping, north-striking faults that bound basins known as the North Valleys. At the latitude of the North Valleys, approximately 15-25% of the Pacific-North American plate boundary strain is accommodated east of the Sierra Nevada through a combination of normal oblique (dextral) slip on the Sierra Nevada frontal fault system and dextral slip along faults in the northern Walker Lane (Hammond et al., 2011; Wesnousky, 2005; Faulds et al., 2005; Ramelli et al., 2005).

Faults in the North Valleys, including the Spanish Springs Valley, Lemon Valley, Granite Hills, Fred’s Mountain, Petersen Mountain, and Last Chance faults represent a distributed system of faults that accommodate oblique extension and vertical thinning and have been interpreted as a trailing imbricate fan system (Faulds et al., 2005). The North Valleys are bound on the north by the northwest-trending dextral Honey Lake and Warm Springs Valley faults and on the south by the Peavine Peak fault, a northwest-trending normal oblique (dextral) slip range front fault that represents the northern continuation of the Carson Range/Mount Rose fault system. Based on these geometric relations, Koehler

(2019) inferred that the North Valleys faults may play a role in transferring oblique slip from the Sierra Nevada range front to strike-slip faults of the northeastern Walker Lane.

Geodetic studies indicate that up to 7 mm/yr of dextral shear is distributed across the northern Walker Lane and primarily accommodated along the left-stepping Pyramid Lake, Honey Lake, and Warm Springs Valley faults (Hammond et al., 2011). Geodetic studies of the North Valleys estimate that north-striking faults collectively accommodate 0.9-1.2 mm/yr of extension and <0.3 mm/yr of dextral slip, with the Petersen Mountain fault accommodating ~0.4 mm/yr of extension and 0.1 mm/yr of dextral slip (Bormann, 2013). Geologic and paleoseismic studies indicate that faults within the North Valleys all exhibit evidence of Quaternary deformation and are characterized by low slip rates and distributed deformation (Koehler, 2019; Dee et al., 2018; Cordy 1987; Nitchman, 1991; Soeller and Nielson, 1980; Bell, 1984). The Petersen Mountain fault is associated with over 500 m of vertical relief along the eastern side of Petersen Mountain (a west tilted fault block), scarps that cut late Pleistocene alluvial surfaces, triangular facets, and aligned springs. Both traces of the Petersen Mountain fault are recognized as active faults in the U.S. Geological Survey Quaternary fault and fold database and are included as sources in the 2014 update of the National Seismic Hazards Model (Petersen et al., 2014). Within the North Valleys as a whole, geologic information on the timing of earthquakes, recurrence, and slip rates are sparse and the style and distribution of strain is not yet fully resolved.

The purpose of this study is to assess the style of faulting and paleoseismic history of the Petersen Mountain fault. To this end, we conducted geologic, geomorphic, and fault trace mapping, paleoseismic trenching, and geochronologic studies along the

Eastern Petersen Mountain fault. The results are discussed in the context of the fault's role in the kinematic evolution and strain partitioning within the Walker Lane and suggest that the fault has accommodated both normal and lateral displacement in the late Pleistocene.

1.1. Previous studies along the Petersen Mountain fault

The Petersen Mountain fault has been previously mapped by Dohrenwend et al. (1996), Nitchman (1991), Soeller and Nielsen (1980), Bell (1984), and Bonham (1969). These maps were primarily reconnaissance fault trace mapping at small scales and were compiled for the USGS Quaternary Fault and Fold Database (USGS, 2006). In general, these maps all describe the Petersen Mountain fault as two primary east dipping normal faults including a western trace that bounds the eastern side of Petersen Mountain and an eastern trace that extends along the eastern side of an unnamed north-trending bedrock block (herein referred to as Porcupine Ridge). The relative age of Quaternary deposits was only coarsely divided on these maps and only limited information on the age of deformation along the fault was described.

A reconnaissance study of active deformation along the Petersen Mountain fault was conducted by the Nevada Bureau of Mines and Geology in the early 1990's (Nitchman, 1991). That study identified a 2.8-m-high scarp in late Pleistocene lacustrine deposits along the southern part of the fault in Cold Springs Valley. A small hand dug trench excavated across this scarp identified two steeply east dipping fault planes and a juxtaposition of sand against warped lacustrine deltaic strata. Although the Nichman (1991) study suggests the occurrence of at least one late Pleistocene earthquake, absolute ages of the faulted deposits were not determined and comprehensive mapping of active fault traces along the length of the fault were not conducted. Nitchman (1991) also identified a ~3-m-high scarp along the central part of the fault zone but did not study it in detail. Koehler (2019) revisited this scarp and estimated a reconnaissance vertical slip rate of 0.01-0.06 mm/yr assuming normal fault displacement and a broad age range for the displaced surface of 50-175 ka.

2. Methods

Fault traces, Quaternary deposits, and tectonic geomorphic features along the Petersen Mountain fault were mapped in the field aided by lidar data and satellite imagery. The USGS STATEMAP program supported 1:24,000 scale geologic mapping of the Granite Peak 7.5’ quadrangle which covers most of the Petersen Mountain fault trace (Dee, 2019). Lidar data utilized for this project are part of a 2018 dataset acquired for the Reno Carson City Urban area, partially funded by the USGS 3DEP program (Digital Aerial Solutions, 2018). Within the Petersen Mountain fault study area these data have an Aggregate Nominal Pulse (ANPS) spacing of 0.7 m (QL2) and were used to produce a 1m DEM and derivative bare-earth hillshade basemaps for field mapping. The lidar data can be viewed online http://nbmg.maps.arcgis.com/apps/webappviewer/index.html?id=2eb0b527ab8b47c8b1e09323aff14a04.

The trench was excavated, cleaned, and mapped using standard methods. A reference string grid was installed using a Spectra Precision LL300N auto level. Photos of the trench walls were used to develop trench photomosaics using methods modified from Reitman et al. (2015). The photomosaics were printed with a 1-meter grid for field logging. A fault scarp profile was extracted from the lidar DEM's at the trench site using ArcMap. Soils developed into both the hanging wall and foot wall were described based on methods and terminology outlined in Birkeland (1999). Samples of soil horizons were analyzed for particle size distribution at the Desert Research Institute. A DJI Mavic Pro drone survey was conducted at the trench site to generate low altitude images of the site.

Sediment ages were determined through analyses of six Optically Stimulated Luminescence (OSL) samples collected from the trench wall. Stratigraphic units sampled include Units 1, 2, 3, 4, and 8. We targeted quartz sand distributed throughout the trench and on both sides of the fault zone. Samples were collected by tube and block sampling procedures in areas void of bioturbation to the best extent possible following Gray et al. (2015). Lab preparation and data analyses were completed at the Desert Research Institute Luminescence Laboratory (DRILL). Samples were treated to isolate 180-250 μm quartz and then treated with hydrofluoric acid to remove the outer α-irradiated rim of the grains. Samples were measured using a modified single-aliquot regenerative-dose (SAR) protocol with an IR check (Murray and Wintle, 2000). We then used the central age model (CAM) and minimum age model (MAM) to estimate the age of the deposits.

3. Results

3.1. Mapping observations, geometry and kinematics of faults

The Western Petersen Mountain fault (WPMF) strikes generally north-south along the eastern range front of Petersen Mountain, dips to the east (>70°, locally vertical), and is associated with several shorter bedrock splays and basin bounding stepovers ranging in strike from N45E to N20W (Figures 2 and 3). The southern part of the WPMF in Cold Springs Valley consists of a singular trace along the base of an over steepened range-front escarpment and juxtaposes bedrock against latest Pleistocene-Holocene alluvial fan deposits and basal colluvium. North of Cold Springs Valley, the WPMF continues along the range front and makes a 1.4 km right step to the western edge of a broad intermountain catchment (Dee, 2019) (Figure 4). In this area, the fault is characterized by aligned springs, triangular facets, and scarps that displace Quaternary alluvial fan surfaces, landslide deposits, and basal colluvial slopes (Figures 3 and 4). North of the catchment, the WPMF passes through a low bedrock pass and extends along a 500 m high faceted range front with local antithetic strands to Red Rock Valley. There the WPMF is characterized by aligned springs and scarps across middle Pleistocene alluvial fans and landslide deposits (Figures 3 and 4).

The Eastern Petersen Mountain fault (EPMF) extends from several kilometers south of and along the eastern side of Porcupine Ridge to Lee's Flat (Figure 3) and consists of several strands distributed across a >1-km-wide zone. Individual strands of the EPMF range in strike from N10E to N35W, with dips on east and north east dipping strands ranging from 54° to 87°. Along the southern part of the EPMF, several of the fault strands are characterized by aligned springs and scarps in late-Pleistocene alluvial fan and landslide deposits. A seasonal stream channel in this area has an apparent right deflection (Figure 5). Along the eastern side of Porcupine Ridge, strands of the fault form a 0.5 km wide graben associated with a 110-m-deep linear valley and displace middle Pleistocene alluvial fans (Dee, 2019). Slickenlines documented on bedrock fault planes along the EPMF plunge 9° to 19° southeast consistent with down-to-the-east dextral oblique fault motion (Figure 4B).

The geologic map relations provide constraints on the sense of displacement along the two fault strands. Long term late-Cenozoic normal displacement across the WPMF is demonstrated by the high relief of Petersen Mountain range front (>500 m) as well as the accumulation of Miocene sediments to the east that were likely deposited into a basin controlled by early displacement along the fault (Dee, 2019) (Figure 2). This is in contrast to the EPMF which only bounds a small basin along a short length adjacent to Lee's Flat (Figure 3). South of Lee's Flat the EPMF is flanked on both sides by an elevated bedrock erosion surface that does not have a consistent sense of displacement across the fault, and commonly the elevation of the surface is equivalent on both sides.

3.2. Petersen Mountain trench site

Based on our lidar evaluation and field mapping, we confirmed the presence of a ~3-m-high fault scarp along a strand of the EPMF (Figures 4, 5, and 6A). We excavated a trench (39.7828°N, 119.9411°W) across the scarp immediately south of a dirt road, approximately 3.5 km south of Red Rock road on BLM land.

The scarp has a general north-south trend and cuts a late Pleistocene alluvial fan deposit (Figures 4, 6B, and 6D). Koehler (2019) previously characterized the surface cut by the scarp as a Quaternary/Tertiary pediment surface incised by active alluvial fans based on the presence of isolated low bedrock outcrops distributed across the surface west of the scarp. Subsequent more detailed mapping (Dee, 2019) indicates that the surface is better characterized as a late Pleistocene alluvial fan based on its flat interfluve morphology and relative degree of incision (~10 m along the main active wash). The surface contains boulders of granodiorite (Kgdp) up to 1 meter in diameter.

The scarp at the trench site has been isolated from deposition since incision by east draining stream channels and Holocene alluvial fans. Apparent right-deflection of a channel is evident south of the trench in the lidar hillshade (Figures 5 and 6C). South of this apparent stream deflection the fault projects through a linear valley and across a low saddle. In the vicinity of the trench site, the EPMF consists of at least three strands (Figure 4). North of the trench the strand we trenched splits into two splays, one that projects into Porcupine Ridge as a bedrock fault and linear trough (Figure 6B), and another that extends along the eastern side of Porcupine ridge as a graben in a linear valley with down-dropped middle Pleistocene fans (Figures 3 and 4). The WPMF is approximately 0.75 km west of the trench where it is associated with prominent linear scarps in fan and colluvial deposits, aligned springs, and benches.

3.3. Trenching observations and stratigraphic framework

A log of the trench exposure as well as un-interpreted and interpreted photomosaics of the Petersen Mountain fault trench are shown in Figure 7 and Appendix B. Ten stratigraphic units were identified within the trench. Both the north and south walls of the trench exposed the same units laterally and vertically in the footwall and hanging wall (Appendix B Table 1). Two distinct soil profiles are evident in the exposure with the footwall soil being more developed than the soil developed into the hanging wall (Figure 8 and Appendix B Table 2).

The basal unit exposed in the footwall (Unit 6) consists of massive medium to coarse-grained sand, interpreted as completely disintegrated (grussified) bedrock which has discontinuous oxidation stringers. Microscopic analysis of hand samples of Unit 6 indicate that grains are largely angular quartz, plagioclase, orthoclase, biotite and hornblende minerals with a compositional distribution consistent with the local diorite bedrock that outcrops directly southwest of the trench. Unit 6 is unconformably overlain by Unit 7, a thin medium to coarse grained sand with imbricated cobbles of granitic and volcanic composition up to 20 cm in diameter. A fining upward sequence of sand with trace pebbles and cobbles (Unit 8) overlies Unit 7. A well-developed soil (Units 9 and 10) is developed >80 cm into Unit 8 and includes a prominent 23 cm thick reddish-brown sandy clay argillic horizon with high clay percent and coarse angular blocky structure (Figure 8). The reddening color of the footwall soil is attributed to iron minerals inherited from the underlying granodioritic bedrock that oxidize under the influence of groundwater.

The basal deposit in the hanging wall (Unit 1) is a poorly sorted fine to coarse-grained loamy sand with gravel and sub-rounded pebbles and cobbles. Unit 2 overlies Unit 1 and consists of medium- to coarse-grained sand with imbricated sub-rounded to rounded boulders that is 1.5 to 2 m thick and weakly bedded. The cobbles and boulders in Units 1 and 2 are disintegrated and have a quartz diorite composition and do not correlate with units exposed in the footwall. Unit 2 is buried by silty sand with trace cobbles (Unit 3). A weakly developed soil (Units 4 and 5) has developed into the hanging wall deposits and consists of loamy sand with a gray 20-cm-thick cambic B horizon with low clay percent and medium subangular blocky structure (Figure 8). Buried soils and colluvial wedges were not observed in the hanging wall deposits. The relatively uniform thickness and bedded nature of the deposits is consistent with alluvial deposition.

We interpret the footwall package as a bedrock strath or pediment surface overlain by sandy alluvial fan deposits. The high clay percent, red color of the argillic horizon, and depth of the soil developed in the footwall suggests a late Pleistocene age for the surface. This age is consistent with Dee (2019) who inferred a late Pleistocene age for intermediate aged (Qfi) alluvial fans distributed across the trench site. The hanging wall package is interpreted as sand and boulder alluvial fan deposits. The low clay percent and gray color of the cambic B horizon, as well as the relatively shallow depth of development of the hanging wall soil suggests a latest Pleistocene-Holocene age for the surface.

Disintegrated bedrock Unit 6 in the footwall is juxtaposed across a steeply east-dipping well-defined fault against boulder alluvium (Unit 2) of the hanging wall (Figures 7, 8D, and 8E). The relation between Unit 8/9 (footwall) and Unit 3/4 (hanging wall) across the fault is ambiguous, however the different texture (sandy clay and loamy sand, respectively) and degree of soil development in these deposits, as well as subtle shears suggest that they may also be juxtaposed across the fault. Alternatively, these deposits could represent a continuous deposit across the scarp. The fault has an orientation of 335°/55°NE. A wide shear zone extends 10 m west from the main fault with faults and fractures that strike roughly north-south, dip eastward between 52° and 80°, and propagate through the disintegrated bedrock (Appendix B).

3.4. Age of sediments

The OSL age results are shown in Table 1. Graphs of CAM age as a function of water content, and the weighted histogram and kernel density estimate plots produced by R-Luminescence package for each PMF sample are provided in Appendix A Supplementary Data. MAM was applied to sample PMF001 based on a high overdispersion initially run with the central age model. All other samples passed the less than 25% overdispersion criteria using CAM. The OSL age in Table 1 and radial plot for PMF001 are from the minimum age model. Laboratory analyses showed that all samples were near or at the luminescence saturation limit. Locations of samples are shown with OSL ages on the fault trench log in Figure 7.

The temporal accuracy of ages determined by OSL analysis is limited by the effects of saturation, partial bleaching, and bioturbation/mixing among other factors (Batemen et al., 2007). The results from the OSL age models for samples PMF002 (28 ka), PMF004 (32 ka), PMF005 (28 ka), and PMF006 (20 ka) were expected and suggest that grain transportation was in a fluvial environment allowing for the grains to be relatively well sorted and fully bleached. This is reflected in the narrow distribution of grain luminescence in the radial plots found in Appendix A. The radial plots for samples PMF001 and PMF003 displayed a greater distribution in grain luminescence, as well as grain luminescence populations seen in the histograms in Appendix A, indicating partial bleaching and mixing with modern soil. Sample PMF001 was collected in fine sand

(Unit 8) suggesting a sheet wash- alluvial fan environment which is consistent with field observations. Sample PMF003 had the most grain luminescence populations and largest distribution of luminescence typical with partially bleached grains. PMF003 was collected at the base of Unit 4, a sandy soil, within proximity to the surface allowing for bioturbation. The extremely young age for sample PMF003 (~3 ka) likely reflects partial bleaching related to mixing in the pedoturbation zone (Figure 8a and 8b).

The ~10-20 ka age determined for the sandy alluvial deposits near the surface (but beneath the pedoturbation zone) in both the footwall and hanging wall suggests a late Pleistocene age for the surfaces. This age is consistent with ages determined elsewhere for intermediate Qfi alluvial fan deposits in the region (Dee et. al., 2018).

4. Discussion

4.1. Characteristics and timing of faulting

Stratigraphic and structural relations exposed in the trench show juxtaposition of sand and boulder alluvial fan deposits (Units 1, 2, and 3) against disintegrated bedrock and alluvial fan deposits (Units 6, 7, and 9). Soils with different pedogenic properties are also juxtaposed across the fault, however, clear fault planes have been obscured by soil processes (Figures 7 and 8). The boulder alluvium (Unit 2) is identical to sediments exposed in the channel north of the trench suggesting that this deposit was brought to its current position through right-lateral faulting. The relations considered with the existence of an east-facing scarp suggest the occurrence of at least one earthquake characterized by oblique lateral displacement. We propose two alternative possibilities for the age of faulting. First (Scenario 1), that faulting postdates the age of the soil developed in the footwall evidenced by the juxtaposition of soils across the fault. A second possibility, (Scenario 2), based on similar compositional characteristics of sandy alluvial fan deposits (Unit 8/9 on the footwall and Unit 3/4 on the hanging wall) is that these units bury the fault indicating that faulting occurred prior to their deposition but after the deposition of the boulder alluvial fan deposit (Unit 2). If true, this would suggest that the differences in soil development and deposit texture across the scarp may be more a reflection of parent materials and less of an indication of relative age (i.e. the red soil on the footwall reflects the influence of the iron rich granodioritic material below the B horizon). Furthermore, this suggests alluvial fan sheet deposition across an existing gentle fault scarp. A schematic diagram showing these alternatives is shown in Figure 9A. In either case, faulting occurred in the late Pleistocene.

Multiple constraints on the age of faulting can be inferred from the geochronology and stratigraphic relations. Based on the subtle tectonic geomorphology documented in our mapping, we infer that scenario 1 is unlikely, but could indicate that faulting postdates 10-20 ka. Our preferred interpretation (Scenario 2) is that faulting occurred prior to ~10-20 ka and after the deposition of the boulder alluvial fan (Unit 2), which has a minimum age of ~32 ka. However, we acknowledge that the laterally displaced deposits may be older than the OSL analyses suggest.

Although the two scenarios described above are consistent with the exposed stratigraphy, there remains a mismatch between the height of the scarp and the vertical separation of the stratigraphy that is difficult to reconcile. An estimate of the amount of displacement that postdates the ~32 ka age constraint for the timing of faulting can be calculated based on the available geodetic and geologic slip rate estimates for the Petersen Mountain fault. Using vertical slip rate estimates of 0.4 mm/yr (geodetic; Bormann, 2013) and 0.01-0.06 mm/yr (geologic; Koehler, 2019) implies vertical separations of 12 m and 0.3-1.8 m, respectively. The vertical displacement estimated from the geodetic slip rate is clearly an overestimate based on the surface scarp height. The upper bound of the vertical displacement estimated from the geologic slip rate (1.8 m) is similar to the ~ 2 m of separation of the bedrock pediment surface assuming the surface is buried by Units 1/2 in the hanging wall and occurs close to the floor of the trench consistent with a component of normal separation in the most recent earthquake. We acknowledge that the total height of the scarp may be a reflection of additional paleoevents but that the amount of separation is reasonable to have occurred in one event. A right-lateral slip rate of 0.1 mm/yr estimated geodetically (Bormann, 2013) allows the possibility of up to 3 m of lateral slip in the last ~30 ka. We do not have constraints on the extent of the boulder alluvial deposit east of the scarp that was sourced from a channel 100 m north of the trench, however the fan could have extended an unknown amount north and south of the mouth of the channel as is observed along many range front scarps in western Nevada. Although we cannot estimate a lower bound on the amount of lateral slip in the most recent earthquake, the geodetic constraints and the trench relations are consistent with a component of lateral slip. We surmise that the most recent earthquake did not produce a steep free face scarp, but instead was associated with a broad escarpment related to the juxtaposition of units. This would be consistent with the lack of colluvial wedge deposits in the hanging wall stratigraphic package. We conclude that the most recent earthquake was associated with components of both normal and lateral deformation (oblique slip).

4.2. Displacement across the Petersen Mountain Fault Zone and its role in the evolution of the northern Walker Lane

The WPMF fault has a long history of normal displacement based on the steep relief (>500 m) along its range front and accumulation of Miocene basin sediments east of the fault. However, several wind gaps and other topographic highs occur along the fault, and it is not associated with a deep Quaternary basin. The EPMF extends across an elevated bedrock erosion surface that has similar elevation on both sides of the fault and is only associated with a small basin along a short reach of the fault at its northern end. The lack of Miocene sediments on either side of Porcupine Ridge suggest that it has been exhumed during the Quaternary. These observations in conjunction with the dip of the fault, dextral oblique kinematic data from fault surfaces and tectonic geomorphic features, trenching observations indicative of lateral motion, and absence of a deep continuous pre-Quaternary basin suggest that the EPMF may have developed in the early Pleistocene in response to Walker lane shear, as opposed to longer-lived Basin and Range style normal faulting.

In the northern Walker Lane, strain accumulation measured geodetically and strain release documented in geologic studies have clearly shown that dextral slip is the primary mode of deformation (Faulds et al., 2005; Bormann, 2013; Hammond et al., 2011; Ramelli et al., 2003; 2005; Turner et al., 2008; Gold et al., 2013). The North Valleys sit north of the dextral oblique Peavine Peak fault, southwest of the dextral

Honey Lake and Warm Springs Valley faults, and within a major right step in the dextral fault system. Geologic studies indicate a Holocene slip rate of 1.4-1.9 mm/yr for the Honey Lake fault (Gold et al., 2017). Ramelli et al. (2003; 2005) estimated a slip rate of ~1 mm/yr for the Peavine Peak fault and suggested equal components of normal and right-lateral slip. These studies suggest that dextral shear projects through the North Valleys, consistent with our observations of dextral deformation and a component of shear measured geodetically.

Analyses of strain rate data across the northern Walker Lane at the latitude of this study indicate that the shear direction in the modern strain field is oriented N38° ± 3°W, approximately parallel to both the average strike of the Walker Lane fault system and motion of the Sierra Nevada-Great Valley (SNGV) microplate to the central Basin and Range (Hammond and Thatcher, 2007). A more regional geodetic analysis of the contemporary strain rate field by Bennett et al. (2003) determined that the SNGV microplate translates N47°W relative to North America, an orientation similar to the strike of the Honey Lake fault. In Figure 9B, we compare the orientation of the Petersen Mountain fault to two synthetic simple shear models (Sylvester, 1988) oriented N35°W and N47°W to capture the range in contemporary northwest shear orientations. This comparison shows that, depending on the orientation of the strain field, the N-S to N15°W orientation of the Petersen Mountain fault traces fall within the predicted orientation of normal displacement or slip along R shears. Thus, in the modern strain field, the Petersen Mountain fault is favorably oriented to accommodate components of both normal and lateral slip in an incipient strike-slip system and may kinematically act to transfer slip from the Peavine Peak fault to the Honey Lake fault (Figure 9B).

The observations of normal faulting and a component of lateral deformation along the Petersen Mountain fault indicate that tectonic strain is being accommodated by shear overprinting a previously existing normal fault. This process may be analogous to overprinting tectonic styles documented in the central and southern Walker Lane. Studies along the White Mountain fault indicate a long history of normal faulting with a transition to lateral motion within the last ~750 ka (Kirby et al., 2006; Stockli et al., 2003). Similarly, studies along the Wassuk Range fault zone indicate slip partitioning between rangefront normal faults and strike-slip faults that extend obliquely across the northern end of the fault (Bormann et al., 2012; Dong et al., 2014). The discontinuous nature of tectonic geomorphic features and fault traces may indicate the development of a youthful dextral fault system, possibly a Riedel shear structure, within the North Valleys along the transition between the Basin and Range and Walker Lane. In this sense, the Petersen Mountain fault may be developing a bypass across the right step between the Sierra Nevada frontal fault system and faults in the northeastern Walker Lane and may eventually integrate the Peavine Peak and Honey Lake faults (Figure 9B).

5. Conclusions

The Petersen Mountain fault within the North Valleys area of the northern Walker Lane has previously been characterized as a range front normal fault (USGS, 2006). We conducted geologic and geomorphic mapping along the 25-km-long length of the fault and excavated a trench to examine the fault’s style of deformation. The results indicate that the fault is expressed as two main traces (WPMF and EPMF) each composed of a complex network of short stepping strands. Fault striations measured on calcified fault planes indicate down-to-the-east dextral oblique slip along the fault. Additionally, tectonic geomorphic features along the fault including triangular facets, linear valleys, aligned saddles, notches, springs, and scarps are consistent with components of both normal and lateral deformation. The lack of a continuous basin along the length of the EPMF provides evidence that the fault is not a classic Basin and Range style normal fault. Observations from the trench exposure including the juxtaposition of stratigraphic units across the fault, the relative degree of soil development in the faulted surface, and ages of faulted deposits estimated from OSL analyses indicate the occurrence of at least one earthquake in the late Pleistocene that was associated with lateral displacement on a dipping fault.

The combined observations indicate that the Petersen Mountain fault accommodates components of both normal and dextral deformation (oblique slip), possibly along a pre-existing normal fault system. The Quaternary deformation may be related to the development of Riedel shearing that is responding to regional northwest directed shear. This suggests that active deformation along Riedel shears is an important component in the development of youthful or incipient strike-slip fault systems. Thus, the Petersen Mountain fault may ultimately provide an important kinematic link between the Sierra Nevada Frontal Fault system and faults of the northern Walker Lane.

Acknowledgements

This work was funded under USGS NEHRP Cooperative Agreement G18AP00007. Additional field support to De Masi was funded by the Geological Society of America Graduate Student Research Grant, and the University of Nevada Reno

Graduate Student Association Graduate Student Research Grant. We appreciate field assistance during the trenching from C. Chupik, C. Castillo, E. Kleber, and various groups of graduate students from UNR. C. Neudorf of the DRI E.L. Cord Luminescence Laboratory assisted De Masi during sample preparation and data analysis. We thank R. Gold and an anonymous reviewer for insightful comments that improved the manuscript.

References

Barnhart, W.D., Briggs, R.W., Reitman, N.G., Gold, R.D., and Hayes, G.P., 2015, Evidence for slip partitioning and bimodal slip behavior on a single fault: Surface slip characteristics of the 2013 Mw7.7 Balochistan, Pakistan earthquake, Earth and Planetary Science Letters, 420, 1-11.

Bateman, M.D., Boulter, C.H., Carr, A.S., Frederick, C.D., Peter, D. & Wilder, M. 2007: Detecting post-depositional sediment disturbance in sandy deposits using optical luminescence. Quaternary Geochronology 2, 57–64.

Bell, J.W., 1984, Quaternary fault map of Nevada-Reno sheet, Nevada Bureau of Mines and Geology Map 79, 1 sheet, scale 1:250,000.

Bennett, R.A., Wernicke, B.P., Niemi, N.A., Friedrich, A.M. and Davis, J. L., 2003, *Contemporary strain rates in the northern Basin and Range province from GPS data.* Tectonics, 22 (2). Art. No. 1008. ISSN 0278-7407

Birkeland, P.W., 1999, Soils and Geomorphology, 432 pp., Oxford University Press.

Bormann, J., 2013. New insights into strain accumulation and release in the Central and Northern Walker Lane, Pacific-North American Plate Boundary, California and Nevada, USA. Ph.D. Dissertation. University of Nevada, Reno.

Bormann, J.M., Surpless, B.E., Caffee, M.W., and Wesnousky, S.G., 2012, Holocene earthquakes and late Pleistocene slip-rate estimates on the Wassuk Range fault zone, Nevada, Bulletin of the Seismological Society of America, v. 102, No. 4, pp. 1884-1891. doi: 10.1785/0120110287.

Castillo, D.A., and Ellsworth, W.L., Seismotectonics of the San Andreas faut system between Point Arena and Cape Mendocino in Northern California: Implications for the development and evolution of a young transform, Journal of Geophysical Research, v. 98, no. B4, pp. 6543-6560.

Cordy, G.E., 1987, Geology and earthquake hazards Reno NE quadrangle: Nevada Bureau of Mines and Geology OpenFile Report 875, 78 p.

Dee, S., 2019, Preliminary geologic map of the Granite Peak quadrangle, Washoe County, Nevada: Nevada Bureau of Mines and Geology Open-File Report 19-2, 1:24,000 scale, 5 p.

Dee, S., Ramelli, A.R., and Koehler, R.D., 2018, Pilot paleoseismic investigation of faults in the North Valleys, Reno, NV, Final Technical Report, U.S. Geological Survey National Earthquake Hazards Reduction Program (Award # G16AP00060).

Digital Aerial Solutions, 2018, Lidar project report: NV Reno Carson City Urban: Prepared for U.S. Geological Survey, contract #16PC00044, task order #G17PD01257.

Dixon, T.H, and Xie, S., 2018, A kinematic model for the evolution of the Eastern California Shear Zone and Garlock Fault, Mojave Desert, California, Earth and Planetary Science Letters, V. 494, 2018, P.60-68.

Dohrenwend, J.C., Schell, B.A., Menges, C.M., Moring, B.C., and McKittrick, M.A., 1996, Reconnaissance photogeologic map of young (Quaternary and late Tertiary) faults in Nevada, *In*: Singer, D.A. (ed.), Analysis of Nevada's metal-bearing mineral resources: Nevada Bureau of Mines and Geology Open-File Report 96-2, 1 pl., scale 1:1,000,000.

Dong, S., Ucarkus, G., Wesnousky, S.G., Maloney, J., Kent, G., Driscoll, N., and Baskin, R., 2014, Strike-slip faulting along the Wassuk Range of the northern Walker Lane, Nevada, Geosphere, v. 10, No. 1, pp. 40-48.

Durcan, J.A., King, G.E., and Duller, G.A.T., 2015. DRAC: Dose rate and age calculator for trapped charge dating. Quaternary Geochronology, v.28, p.54-61.

Faulds, J.E., and Henry, C.D., 2008, Tectonic influences on the spatial and temporal evolution of the Walker Lane: An incipient transform fault along the evolving Pacific – North American plate boundary, *in* Spencer, J.E., and Titley, S.R., eds., Ores and orogenesis: Circum-Pacific tectonics, geologic evolution, and ore deposits: Arizona Geological Society Digest 22, p. 437-470.

Faulds, J. E., Henry, C. D., and Hinz, N. H., 2005, Kinematics of the northern Walker Lane: An incipient transform fault along the Pacific–North American plate boundary, Geology 33, 505–508.

Galbraith, R.F., Roberts, R.G., Laslett, G.M., Yoshida, H., Olley, J.M., 1999. Optical dating of single grains of quartz from Jinmium rock shelter, northern Australia. Part I: experimental design and statistical models. Archaeometry, 41, pp. 339-364.

Gray, H.J., Mahan, S.A., Rittenour, T., and Nelson, M.S., 2015, Guide to luminescence dating techniques and their application for paleoseismic research, In: Lund, W.R. (ed.), 2015, Proceedings volume, Basin and Range Province Seismic Hazards Summit III, Utah Geological Survey, Miscellaneous Publication 15-5.

Gold, R.D., dePolo, C.M., Briggs, R.W., Crone, A.J., and Gosse, J., 2013, Late Quaternary slip-rate variations along the Warm Springs Valley fault system, northern Walker Lane, California- Nevada border, Bulletin of the Seismological Society of America, v. 103, no 1, p. 542-558.

Gold, R.D., Briggs, R.W., Crone, A.J., and Duross, C.B., 2017, Refining fault slip rates using multiple displaced terrace risers-An example from the Honey Lake fault, NE California, USA, Earth and Planetary Science Letters, v. 477, pp. 134-146.

Hammond, W.C., Blewitt, G., and Kreemer, C., 2011, Block modeling of crustal deformation of the northern Walker Lane and Basin and Range from GPS velocities, J. Geophys. Res. B Solid Earth Planets 116, 1-28.

Hammond, W.C., and Thatcher, W., 2007, Crustal deformation across the Sierra Nevada, northern Walker Lane, Basin and Range transition, western United States measured with GPS, 2000–2004, J. Geophys. Res., 112, B05411, doi:10.1029/2006JB004625.

Hornafius, J.S., Luyendyk, B.P., Terres, R.R., Kamerling, M.J., 1986. Timing and extent of Neogene tectonic rotation in the western Transverse Ranges, California. Geol. Soc. Am. Bull. 97, 1476–1487.

Kelsey, H.M., and Carver, G.A., 1988, Late Neogene and Quaternary tectonics associated with northward growth of the San Andreas Transform Fault, northern California, Journal of Geophysical Research, v. 93, no. B5, pp 4797-4819.

Kirby, E., Burbank, D.W., Reheis, M., Phillips, F., 2006, Temporal variations in slip rate of the White Mountain Fault Zone, Eastern California, Earth and Planetary Science Letters, V. 248, Issues 1–2, pp. 168-185.

Koehler, R.D., 2019, Active faulting in the North Valleys region of Reno, Nevada: A distributed zone within the northern Walker Lane, Geomorphology, v. 326, p. 38-53.

Liritzis, I., Singhvi, A.K., Feathers, J.K., Wagner, G.A., Kadereit, A., Zacharias, N. and Li, S.H. (2013) Luminescence dating in Archaeology, Anthropology and Geoarchaeology: An overview. Springer Briefs in Earth System Sciences, Berlin.

Murray, A.S., and Wintle, A.G., 2000, Luminescence dating of quartz using an improved single-aliquot regenerative-dose protocol: Radiation Measurements, v. 32, no. 1, p. 57-73.

Nitchman, S.P., 1991, Petersen Mountain fault: Nevada Bureau of Mines and Geology Preliminary Fault Evaluation Report, 3 p., scale 1:62,500.

Peltzer, G., Tapponier, P., 1988. Formation and evolution of strike-slip faults, rifts, and basins during the India-Asia collision: an experimental approach. J. Geophys. Res. 93 (B12) 15,085-15,117.

Petersen, M. D., Moschetti, M. P., Powers, P. M., Mueller, C. S., Haller, K. M., Frankel, A. D., Zeng, Y., Rezaeian, S., Harmsen, S. C., Boyd, O. S., Field, N., Chen, R., Rukstales, K. S., Luco, N., Wheeler, R. L., Williams, R. A., and Olsen, A. H., 2014b. Documentation for the 2014 Update of the United States National Seismic Hazard Maps, U.S. Geological Survey Open-File Report 2014-1091, 243 pp.

Prescott, J.R., & Hutton, J.T. (1994). Cosmic ray contributions to dose rates for luminescence and ESR dating: large depths and long-term time variations. Radiation Measurements, 23, 497-500.

Ramelli, A. R., dePolo, C. M., and Bell, J.W., 2003, Paleoseismic studies of the Peavine Peak fault, NEHRP Technical Report, 01HQGR0167, 15 pp.

Ramelli, A. R., Bell, J.W., and dePolo, C. M., 2005, Peavine Peak fault: Another Piece of the Walker Lane Puzzle, in Lund, W.R., editor, Western States Seismic Policy Council Proceedings Volume of the Basin and Range Province Seismic-Hazards Summit II: Utah Geological Survey Miscellaneous Publication 05-2.

Reitman, N.G., Bennett, S.E.K., Gold, R.D., Briggs, R.W., and DuRoss, C.B., 2015, High-resolution trench photomosaics from image-based modeling: workflow and error analysis, Bulletin of the Seismological Society of America, V. 105, no. 5, pp. 2354-2366.

Richard, S.M., 1993. Palinspastic reconstruction of southeastern California and southwestern Arizona. Tectonics 12, 830–852.

Schermer, E.R., Luyendyk, B.P., Cisowski, S., 1996. Late cenozoic structure and tectonics of the northern Mojave Desert. Tectonics 15, 905–932.

Soeller, S.A., and Nielson, R.L., 1980, Geologic map, Reno NW quadrangle, Nevada Bureau of Mines and Geology Map 4Dg, scale 1:24,000.

Stockli, D.F., Dumitru,T.A., McWilliams, M.O., and Farley, K.A., 2003, Cenozoic tectonic evolution of the White Mountains, California and Nevada, Geol. Soc. Amer. Bull. 115. 788–816.

Sturmer, D.M., and Faulds, J.E., 2018, Kinematic evolution of the Olinghouse fault and the role of a major sinistral fault in the Walker Lane dextral shear zone, Nevada, USA: Journal of Structural Geology, v. 115, p. 47-63.

Sylvester, A.G., 1988. Strike-slip faults. Geol. Soc. Am. Bull. 100, 1666–1703.

Trexler Jr., J.H., Cashman, P.H., Henry, C.D., Muntean, T., Schwartz, K., TenBrink, A., Faulds, J.E., Perkins, M., Kelly, T., 2000. Neogene basins in western Nevada document the tectonic history of the Sierra Nevada-Basin and Range transition zone form the last 12 Ma. In: In: Lageson, D.R., Peters, S.G., Lahren, M.M. (Eds.), Great Basin and Sierra Nevada, vol. 2. Geological Society of America Field Guide, pp. 97–116.

Turner, R., Koehler, R., Briggs, R. W., and S. G. Wesnousky, 2008, Paleoseismic and slip-rate observations along the Honey Lake fault zone, northeastern California, Bulletin of the Seismological Society of America, 98, 4, 1730-1736.

U.S. Geological Survey, 2006, Quaternary fault and fold database for the United States, https://earthquake.usgs.gov/hazards/qfaults/, accessed February 2, 2019.

Wesnousky, S.G., 2005a. Active faulting in the walker Lane. Tectonics 24, TC3009.

Wesnousky, S. G., 2005b, The San Andreas and Walker Lane fault systems, western North America: transpression, transtension, cumulative slip and the structural evolution of a major transform plate boundary (2005), Journal of Structural Geology, 27, 1505-1512.

Wilcox, R.E., Harding, T.P., Seely, D.R., 1973. Basic wrench tectonics. Bull. Am. Assoc. Pet. Geol. 57, 74–96.

Liritzis, I., Singhvi, A.K., Feathers, J.K., Wagner, G.A., Kadereit, A., Zacharias, N. and Li, S.H. (2013) Luminescence dating in Archaeology, Anthropology and Geoarchaeology: An overview. Springer Briefs in Earth System Sciences, Berlin

FIGURES

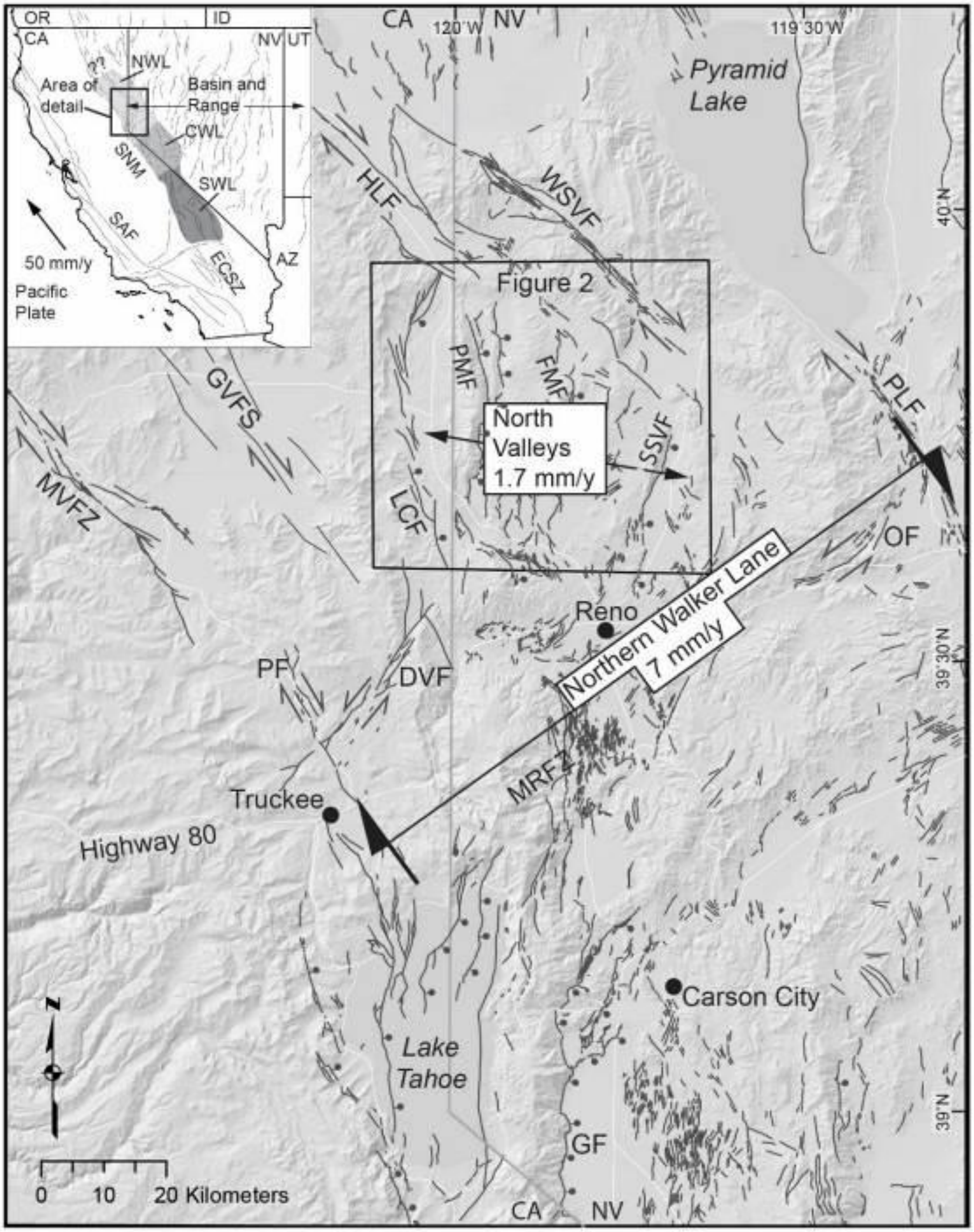
OR
ID
CA
NV
UT
??
NWL
Area of detail
Basin and Range
CWL
SNM
SWL
SAF
ECSZ
AZ
50 mm/y
Pacific Plate
CA
120°W
NV
119°30'W
Pyramid Lake
HLF
WSVF
40°N
Figure 2
PMF
FMF
North Valleys 1.7 mm/y
SSVF
LCF
GVFS
MVFZ
PLF
OF
Reno
Northern Walker Lane 7 mm/y
39°30'N
PF
DVF
MRFZ
Truckee
Highway 80
Carson City
Lake Tahoe
39°N
GF
N
0
10
20 Kilometers
CA
NV

Figure 1. Regional hillshade map of the northern Walker Lane in the vicinity of Reno, NV showing major Quaternary faults (U.S. Geological Survey, 2006) and location of the North Valleys. Inset map shows the location of the study area with respect to the northern Walker Lane and the western Basin and Range Province. Geodetically determined rates of strain accumulation are shown in white boxes (Bormann, 2013) and represent cumulative rates across the zones indicated. Large black arrows indicate the direction of shear and extension. HLF, Honey Lake fault; WSVF, Warm Springs Valley fault; PLF, Pyramid Lake fault; OF, Olinghouse fault; SSVF, Spanish Springs Valley fault; FMF, Fred’s Mountain fault; PMF, Petersen Mountain fault; GVFS, Grizzly Valley Faulty System; MVFZ, Mohawk Valley Fault Zone; PF, Polaris fault; DVF, Dog Valley fault; MRFZ, Mount Rose Fault Zone; GF, Genoa fault.

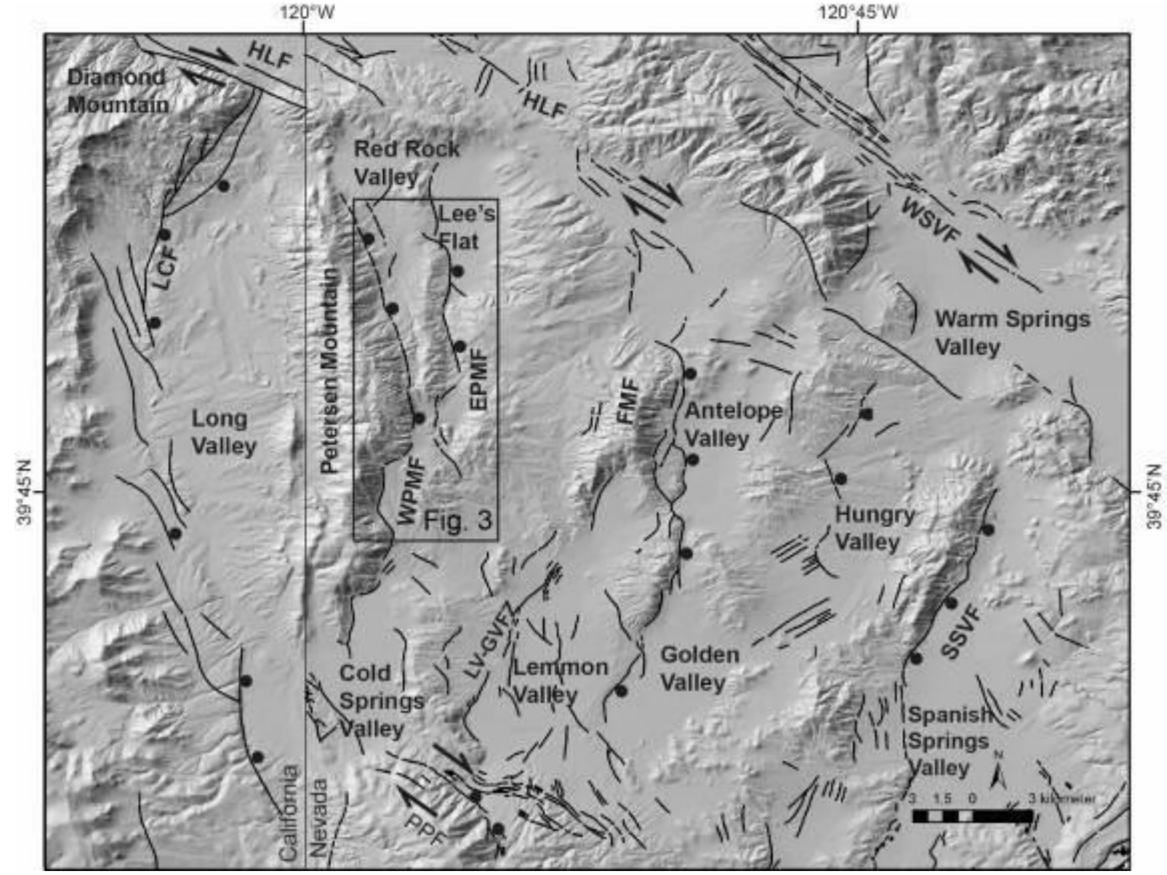

Figure 2. Hillshade map of the North Valleys including the Petersen Mountain fault. Black rectangle shows location of Figure 3. Quaternary faults (US Geological Survey, 2006). LCF, Last Chance fault; WPMF Western Petersen Mountain fault; EPMF, Eastern Petersen Mountain Fault; PPF, Peavine Peak fault; LV-GVFZ, Lemmon Valley-Golden Valley fault zone; FMF, Fred's Mountain fault; SSVF, Spanish Springs Valley fault; HLF, Honey Lake fault; WSVF, Warm Springs Valley fault.

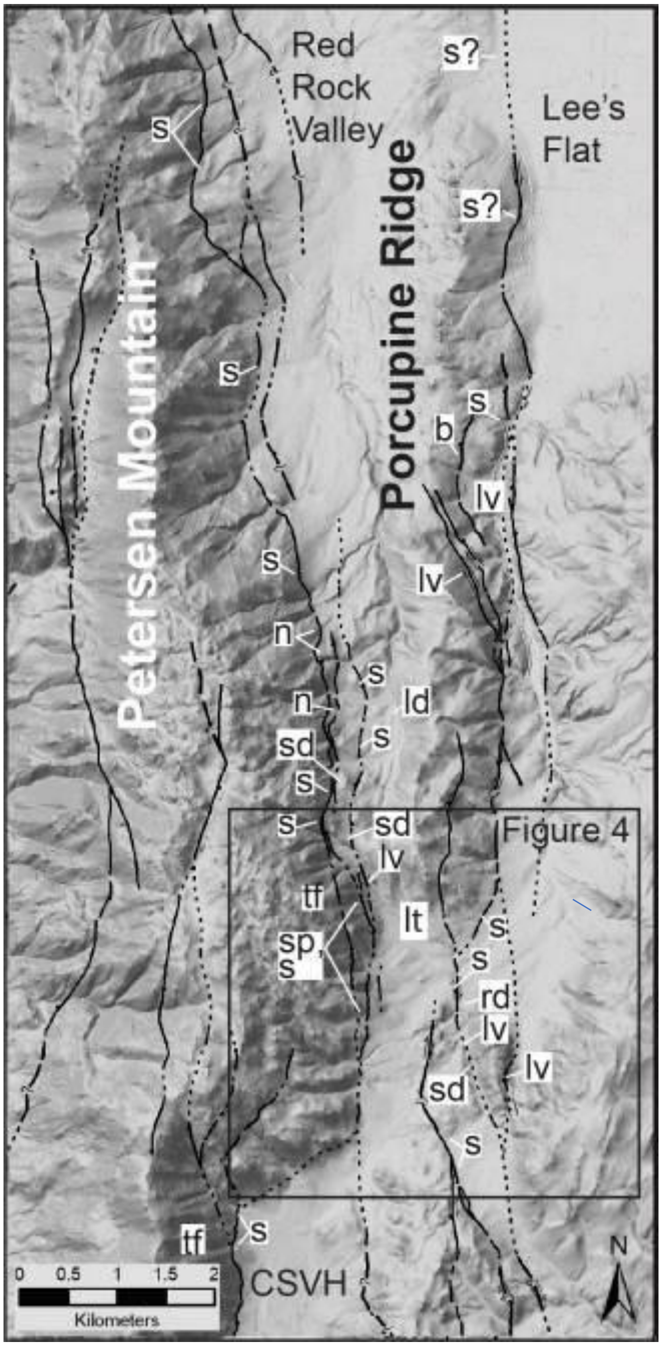

Figure 3. Lidar shaded relief map of area showing major fault traces (Dee, 2019) and tectonic geomorphic features evaluated in this project. Area of detailed geologic mapping shown in Figure 4 indicated by black rectangle. Tectonic geomorphic abbreviations: s, scarp; lv, linear valley; rd, right deflection; sd, saddle; tf, triangular facet; sp, springs; b, bench; ld, linear drainage; n, notch; lt, linear trough. CSVH, headwaters of the Cold Springs Valley drainage basin

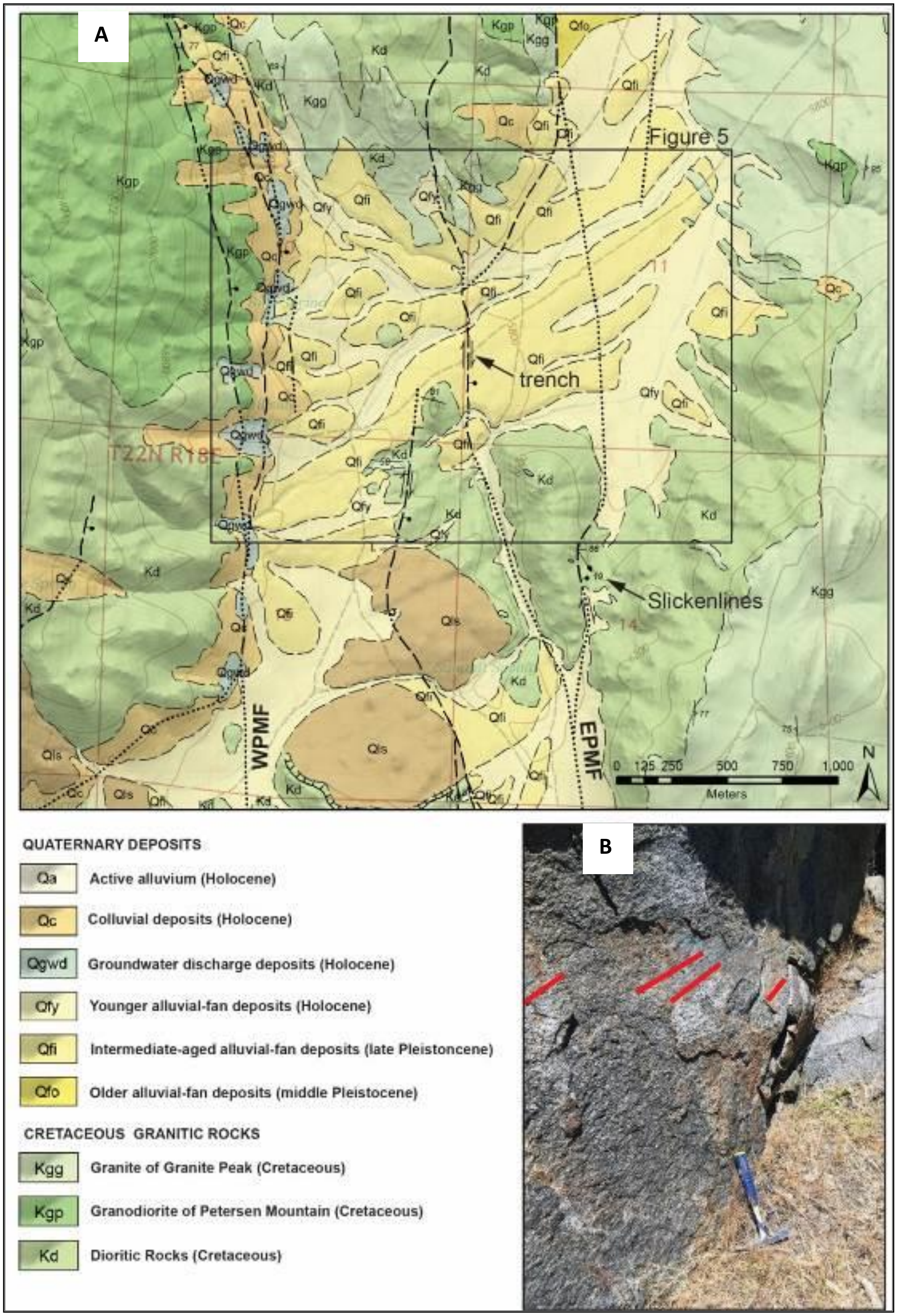
A
Figure 5
trench
Slickenlines
WPMF
EPMF
T22N R18E
Kgp
Kgg
Kd
Qc
Qfi
Qfy
Qfo
Qgwd
Qls
11
14
0 125 250 500 750 1,000
Meters
N
QUATERNARY DEPOSITS
Qa Active alluvium (Holocene)
Qc Colluvial deposits (Holocene)
Qgwd Groundwater discharge deposits (Holocene)
Qfy Younger alluvial-fan deposits (Holocene)
Qfi Intermediate-aged alluvial-fan deposits (late Pleistoncene)
Qfo Older alluvial-fan deposits (middle Pleistocene)
CRETACEOUS GRANITIC ROCKS
Kgg Granite of Granite Peak (Cretaceous)
Kgp Granodiorite of Petersen Mountain (Cretaceous)
Kd Dioritic Rocks (Cretaceous)
B

Figure 4. A) Detailed geologic mapping in the vicinity of the paleoseismic trench taken from Dee (2019). Area of figure 5 shown by black rectangle. WPMF, western Petersen Mountain fault; EPMF, eastern Petersen Mountain fault. B) Fault surface on the EPMF. Fault surface is oriented 332°/66° SE with slickenside lineations (shown with red line) on a calcified fault surface. Slickenline location marked on Fig 4A. Lineations plunge to the southeast with a 21° rake indicative of down-to-the-east dextral oblique fault motion. The fault exposure shown is located <1 km to the SE of the trench site on a parallel fault strand.

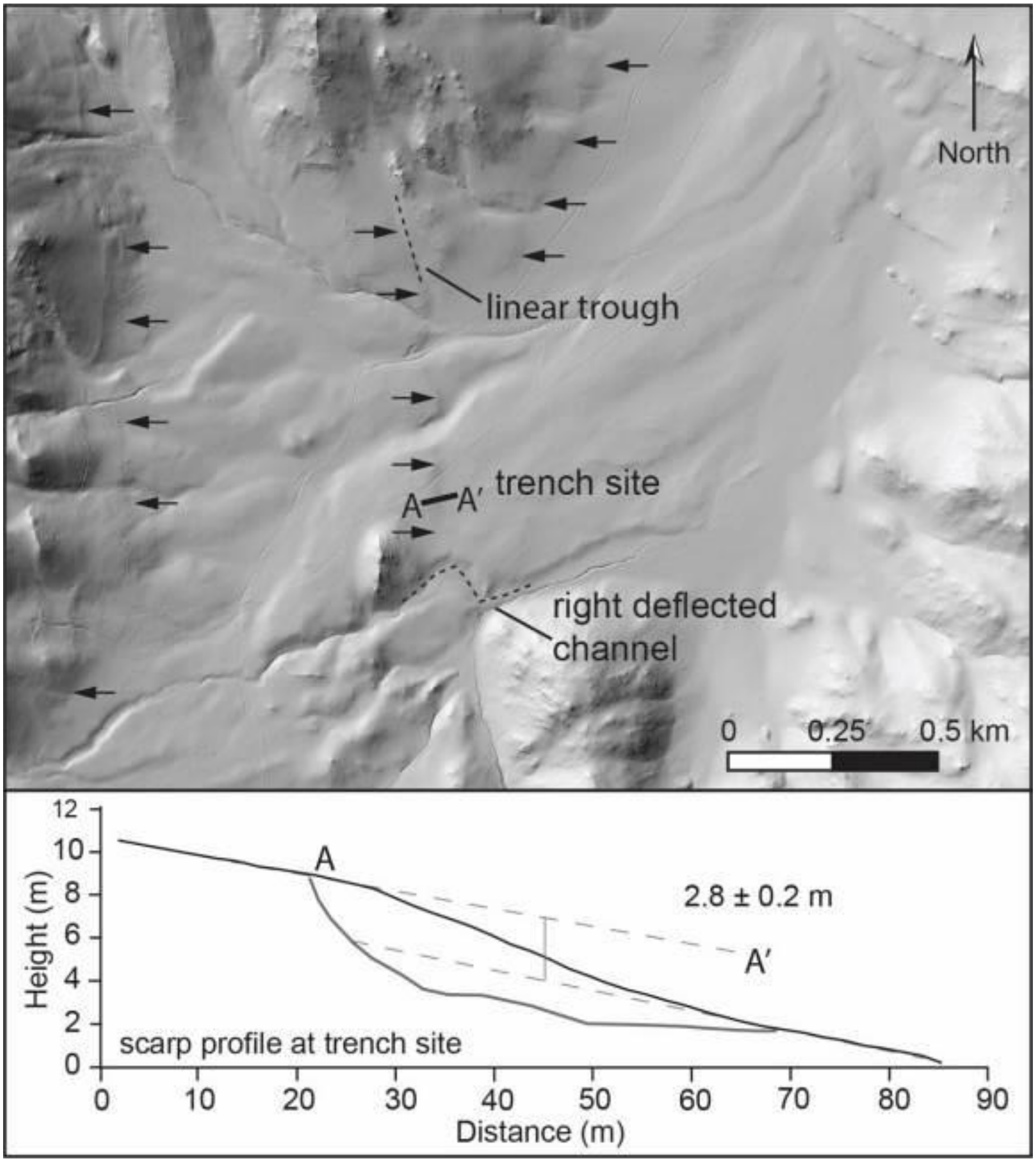

Figure 5. Lidar hillshade map of the area around the paleoseismic trench site. Black arrows indicate prominent faults. Apparent channel defection is about 100 m. Bottom image is a fault scarp profile at the trench site showing ~3 m of vertical separation. Extent of trench shown below profile.

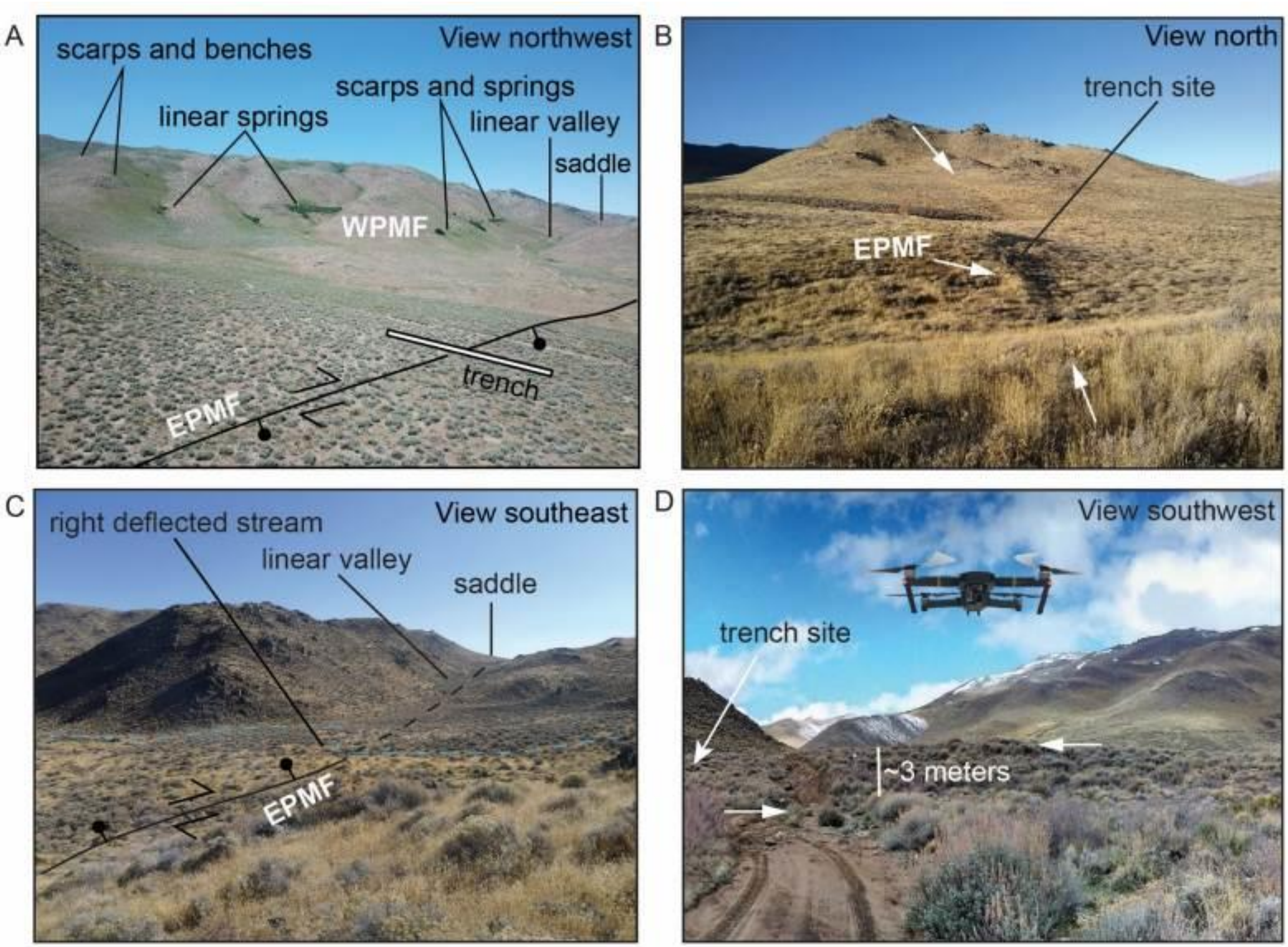
A
scarps and benches
View northwest
linear springs
scarps and springs
linear valley
saddle
WPMF
trench
EPMF
B
View north
trench site
EPMF
C
right deflected stream
View southeast
linear valley
saddle
EPMF
D
View southwest
trench site
~3 meters

Figure 6. A) Drone photograph of the trench site showing tectonic geomorphology along the western trace of the Petersen Mountain fault zone (WPMF) and eastern trace (EPMF). B) Photograph of the trench site along the eastern trace of the Petersen Mountain fault with the scarp shadowed by late afternoon sun. C) Drone photograph of possible right-lateral stream deflection (dashed light blue line) located about 250 m south of the trench. D) Close up photograph of the scarp at the trench site. Fault extends between white arrows in B and D and indicated by black line in A and C.

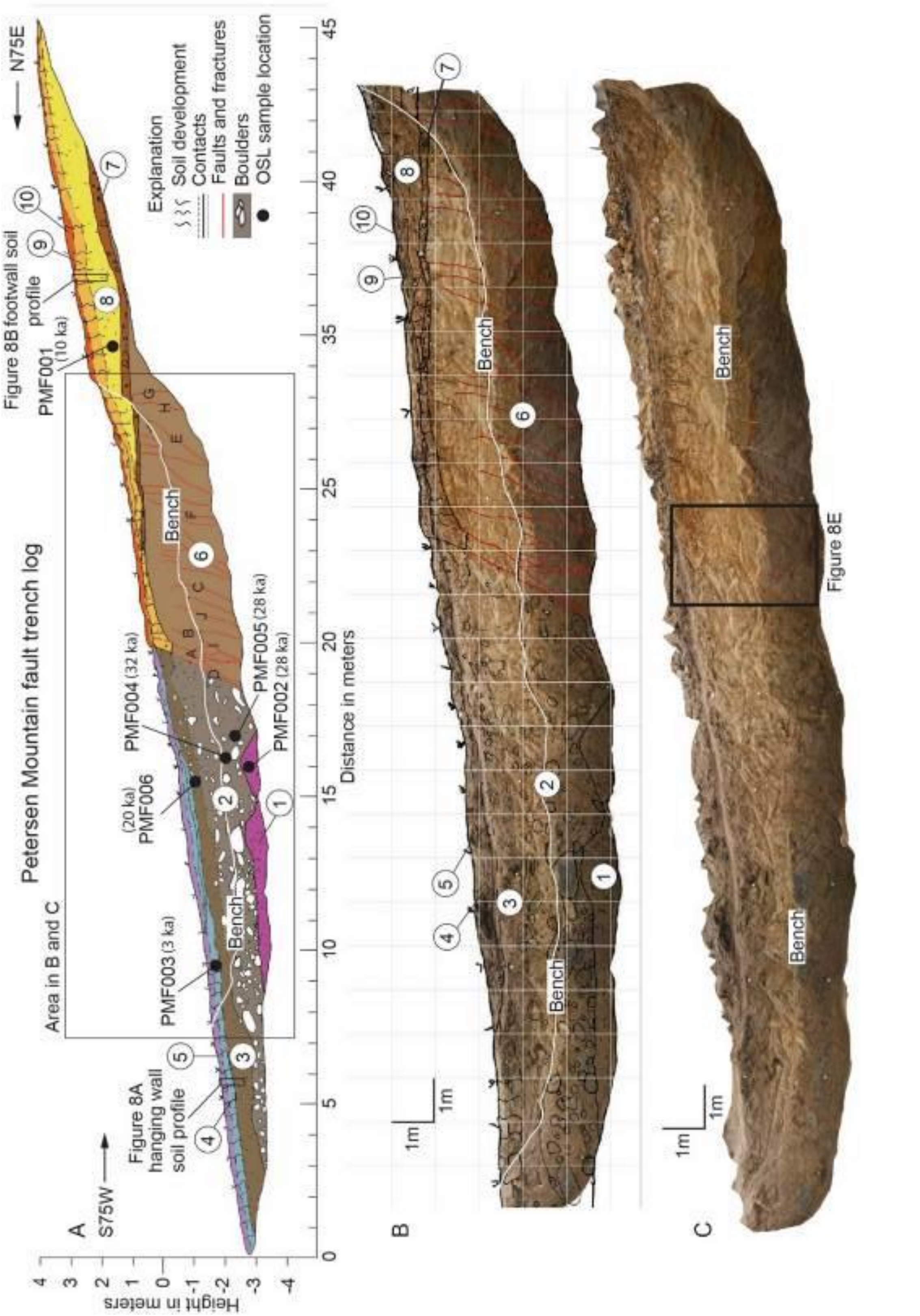
A
Petersen Mountain fault trench log
S75W
N75E
Area in B and C
Figure 8A hanging wall soil profile
Figure 8B footwall soil profile
PMF001 (10 ka)
PMF002 (28 ka)
PMF003 (3 ka)
PMF004 (32 ka)
PMF005 (28 ka)
PMF006 (20 ka)
Bench
A B C D E F G H I J
1
2
3
4
5
6
7
8
9
10
Explanation
Soil development
Contacts
Faults and fractures
Boulders
OSL sample location
Height in meters
4
3
2
1
0
-1
-2
-3
-4
Distance in meters
0
5
10
15
20
25
35
40
45
B
1m
1m
C
Figure 8E

Figure 7. A) Log of Petersen Mountain trench exposure (south wall) showing stratigraphic and structural relations. Open circles show unit numbers, solid black circles are OSL samples, and letters are fracture attitude locations (Appendix B). Black boxes outline Figures 8A and 8B. B) Interpreted photomosaic. C) Uninterpreted photomosaic. Black box outlines Figure 8E.

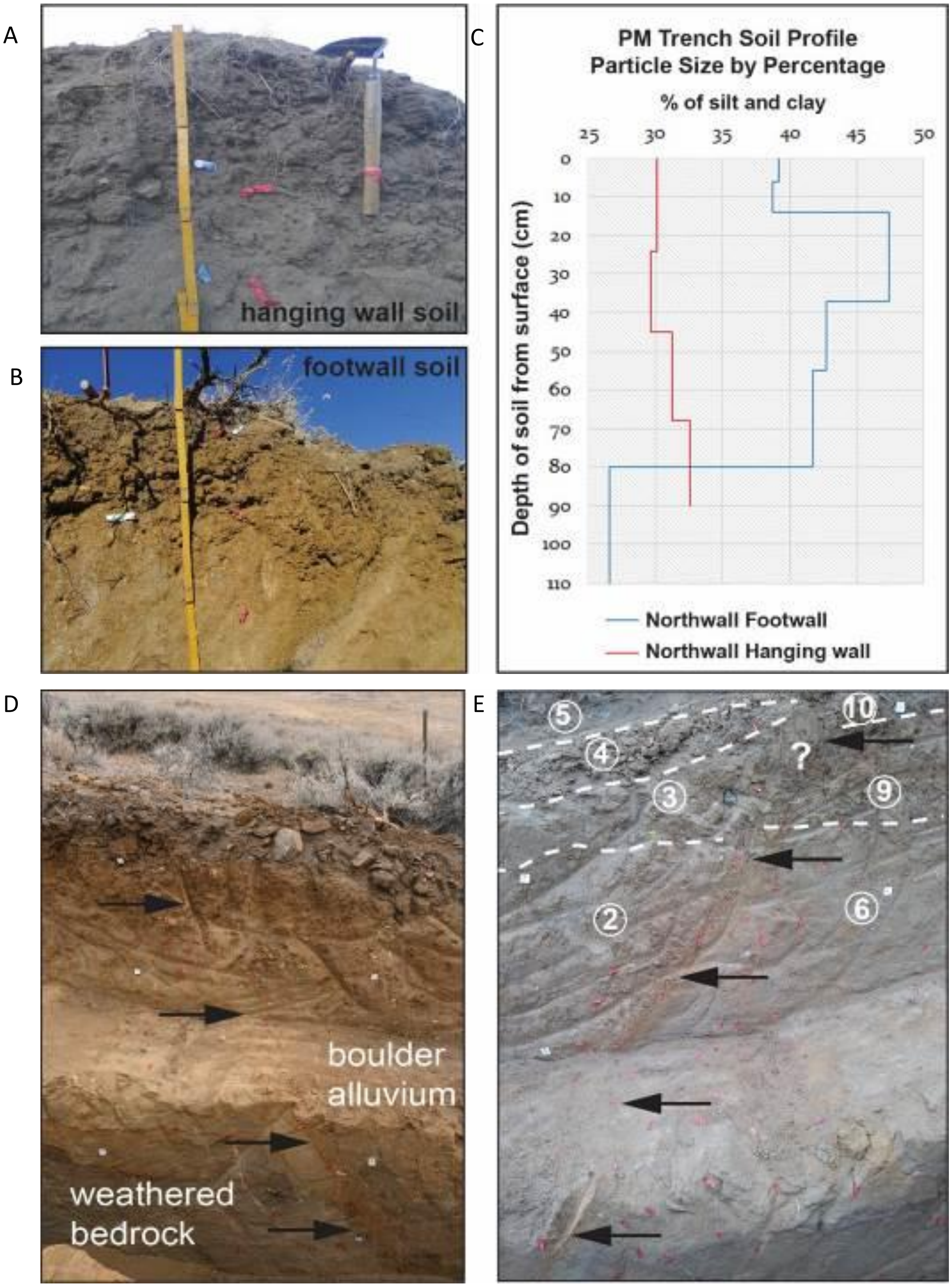
A
hanging wall soil
B
footwall soil
C
PM Trench Soil Profile
Particle Size by Percentage
% of silt and clay
25
30
35
40
45
50
Depth of soil from surface (cm)
0
10
20
30
40
50
60
70
80
90
100
110
Northwall Footwall
Northwall Hanging wall
D
boulder alluvium
weathered bedrock
E
5
10
4
?
3
9
2
6

Figure 8. Photographs of soils developed into the hanging wall (A) and footwall (B). Plot in (C) shows percent silt and clay vs depth for both soils. The higher percentage of silt and clay and red color in the Bt-horizon in the footwall soil suggests a late Pleistocene age. In contrast, the low silt and clay percent and gray color in the Bw-horizon of the hanging wall soil suggests a latest Pleistocene-Holocene age. See Appendix B for complete soil descriptions. D and E show close up photographs of the main fault zone in the trench exposure. D) North wall showing boulder alluvium juxtaposed against weathered bedrock. E) The south wall fault plane is visible in the lower left of the photo where it was excavated into the trench wall. Units are labeled in white. Location of the main fault is shown by black arrows in D and E. Orientations of fractures are presented in Appendix B, Table 3.

A

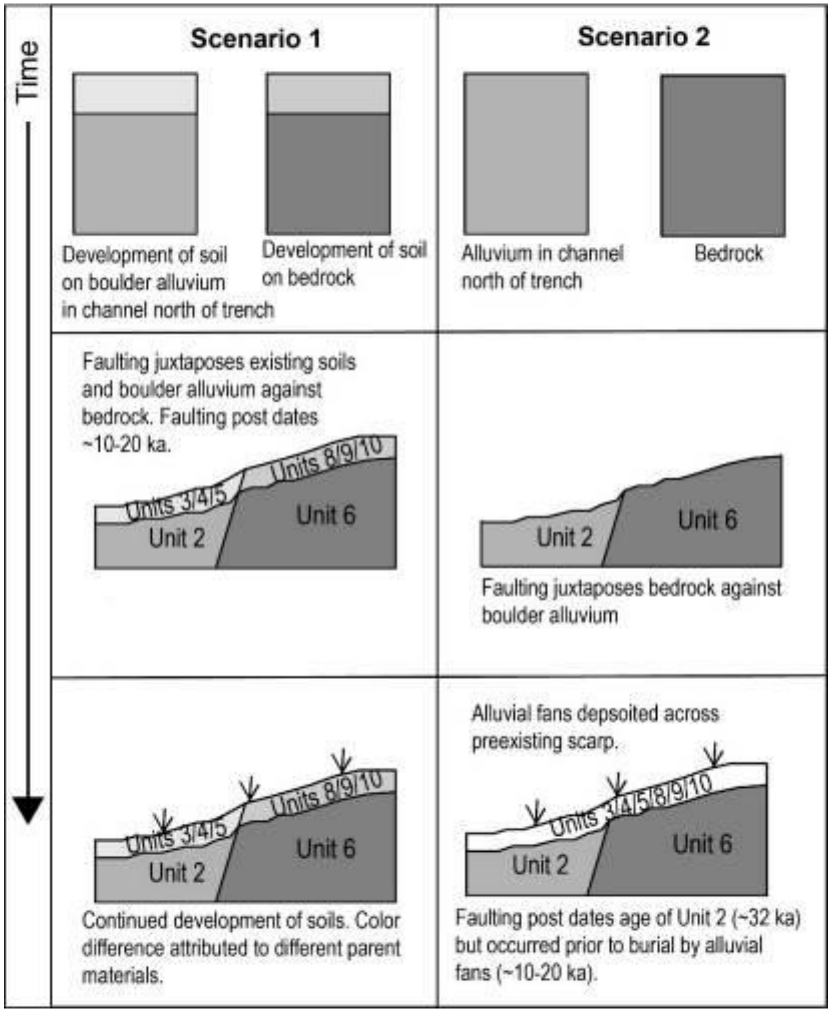
Time
Scenario 1
Scenario 2
Development of soil on boulder alluvium in channel north of trench
Development of soil on bedrock
Alluvium in channel north of trench
Bedrock
Faulting juxtaposes existing soils and boulder alluvium against bedrock. Faulting post dates ~10-20 ka.
Units 3/4/5
Units 8/9/10
Unit 2
Unit 6
Faulting juxtaposes bedrock against boulder alluvium
Alluvial fans depsoited across preexisting scarp.
Units 3/4/5/8/9/10
Continued development of soils. Color difference attributed to different parent materials.
Faulting post dates age of Unit 2 (~32 ka) but occurred prior to burial by alluvial fans (~10-20 ka).

B

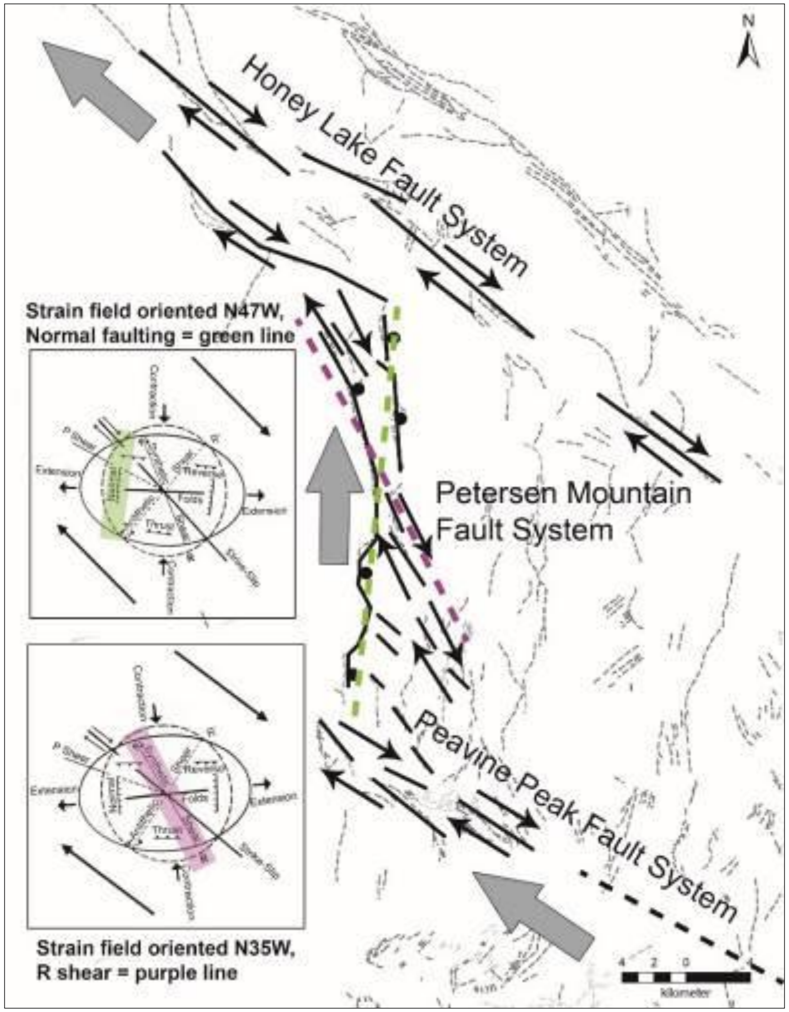
N
Honey Lake Fault System
Petersen Mountain Fault System
Peavine Peak Fault System
Strain field oriented N47W, Normal faulting = green line
Strain field oriented N35W, R shear = purple line
Contraction
Extension
P Shear
R
Reverse
Folds
Thrust
Normal
Strike-Slip
4 2 0
kilometer

Figure 9. A) Schematic history of deposition, soil development, and faulting for Scenario 1 and Scenario 2. Time progresses from top to bottom in each column. B) Schematic cartoon showing a right step in the Peavine Peak, Petersen Mountain and Honey Lake fault systems. Large gray arrows outline right step. Dashed line in Peavine Peak Fault System indicates unconfirmed section of the fault. Insets show simple shear models (Sylvester, 1988) oriented N47^{o}W and N35^{o}W capturing the range of orientations of the modern strain field (Hammond and Thatcher, 2007; Bennet et al., 2003). These shear models indicate alignment of the Petersen Mountain fault with both normal and R shear deformation.

Table 1.

Sample data used to calculate dose rates and luminescence ages.

Sample number	Trench unit	Depth (m)	U (ppm)[a]	Th (ppm)[a]	K (%)[a]	Total dose rate (Gy/ka)[b]	N[c]	CAM Over-dispersion (%)	MAM D_e (Gy)[d]	CAM D_e (Gy)[d]	Age (ka)[d,e]
PMF001	8	1.21	4.58	14	1.15	3.41	23/48	29	32.56 ± 2.98	55.30 ± 3.64	9.84 ± 0.99*
PMF002	1	2.97	3.54	14.3	1.6	3.57	36/48	22	77.38 ± 5.64	96.83 ± 4.36	27.99 ± 1.76
PMF003	4	0.4	3.54	18.05	1.72	4.05	26/48	47	6.42 ± 0.53	12.23 ± 1.17	3.11 ± 0.33
PMF004	2	1.65	3.55	13.4	1.43	3.38	39/48	23	79.75 ± 5.87	103.19 ± 4.60	31.48 ± 1.95
PMF005	2	2.27	3.95	14.25	1.71	3.79	34/48	8	92.63 ± 6.02	101.38 ± 2.96	27.66 ± 1.46
PMF006	3	0.7	4.65	23.6	2.05	4.98	38/48	14	93.31 ± NA	96.92 ± 3.07	20.12 ± 1.09

[a] U and Th were fused with lithium borate and measured with ICP-MS. K2O was measured on bulk samples with ICP-AES and converted to % K. An assumed measurement error of ± 10% was used to calculate the total dose rate.

[b] Dose rates (Gy/ka) were calculated using the conversion factors of Liritzis et al. 2013 and are shown rounded to two decimal places; ages were calculated using values prior to rounding; central values are given for dose-rates and errors are incorporated into that given for the total dose-rate.
Water content of 5% ± 1.5% was used for all dose rate calculations. 180-250 μm grain size fraction used; and 2535 m used for elevation.

Cosmic dose rates (Gy/ka) are calculated according to Prescott and Hutton (1994).

[c] Number of aliquots meeting acceptance criteria/out of total aliquots measured.

[d] The error shown on the $D_{e,}$ is the error modeled with the central age model (CAM); *error modeled with the minimum age model (MAM) (Galbraith et al., 1999).

[e] Luminescence ages were calculated using DRACv1.2 (Durcan et al., 2015) and are expressed as thousands of years before 2015 and rounded to the nearest year.
Error is 2 sigma.

Appendix A. Supplementary OSL data

Appendix A Table 1.

SAR protocols applied in this study.

Step	OSL SAR protocol
1	Natural/Regenerative Dose
2	Preheat (240ºC, 10 s)
3	Blue (470 nm) LED Diodes (125ºC, 100 s)
4	Test Dose (100 Gy s)
5	Cut Heat (160ºC, 0 s)
6	Blue (470 nm) LED Diodes (125ºC, 100 s)
7	Hot Wash Blue (470 nm) LED Diodes (260ºC, 40 s)
8	Return to step 1.

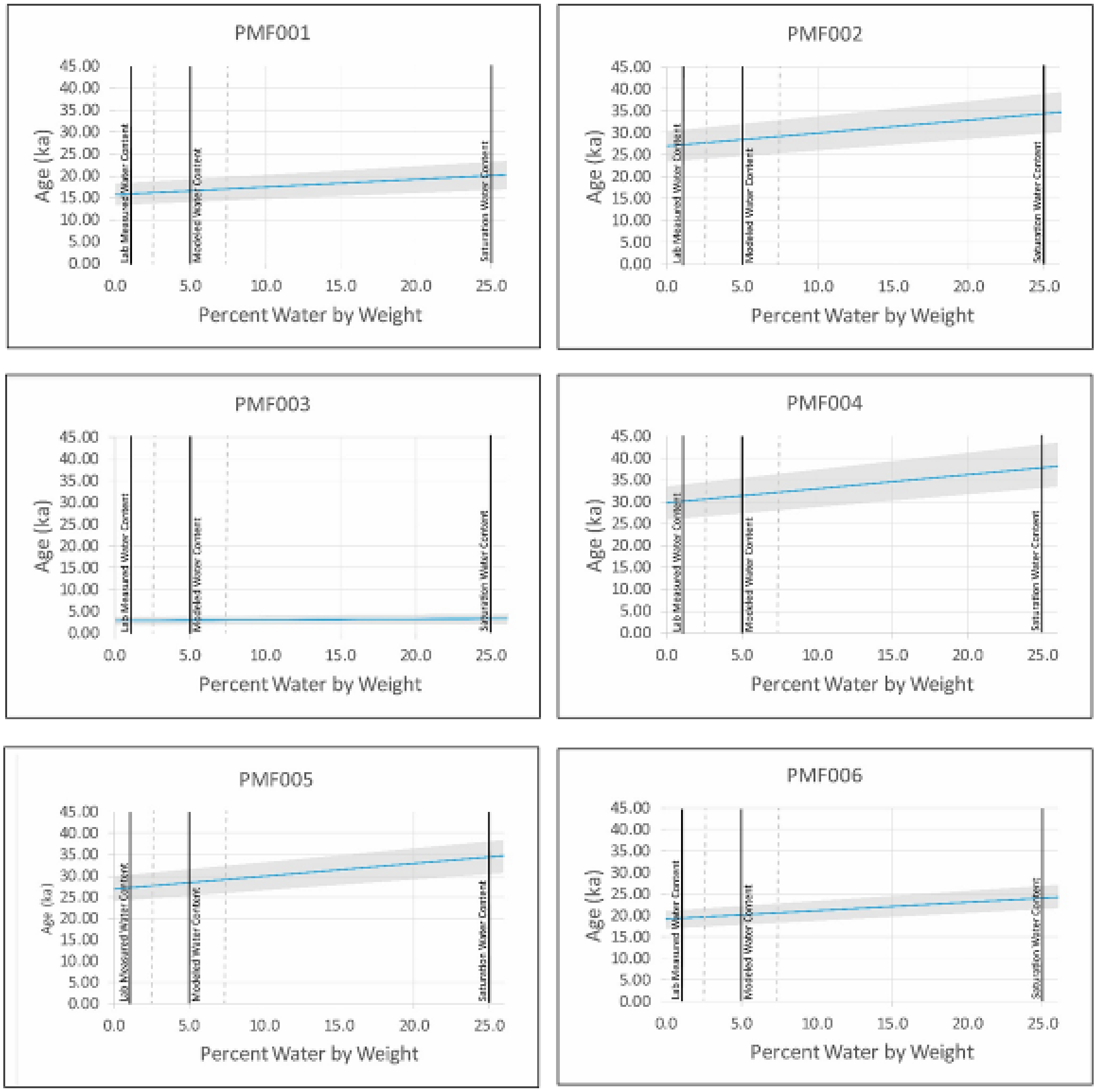

Figure A1. Graph of CAM age as a function of water content. Blue line represents CAM age; gray box shows extent of 95% confidence interval for the CAM age based on 2 sigma; vertical black lines mark the lab measured water content, 5% modeled water content, and 25% saturated water content; vertical gray dashed lines mark the 0.5% modeled water content error.

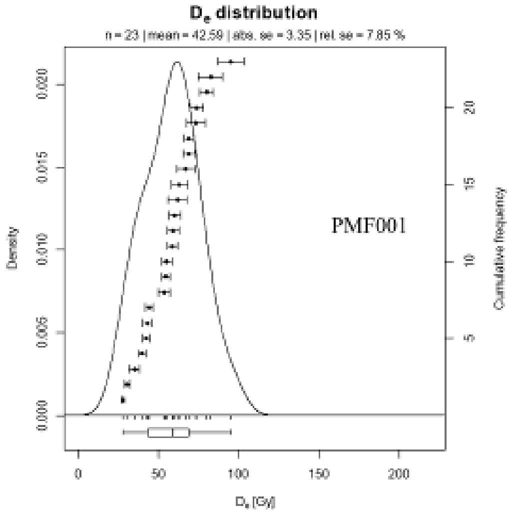
D_e distribution
n = 23 | mean = 42.59 | abs. se = 3.35 | rel. se = 7.85 %
PMF001
Density
Cumulative frequency
D_e [Gy]

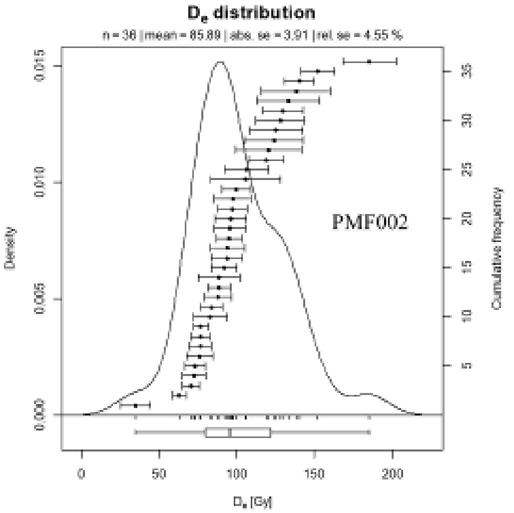
D_e distribution
n = 36 | mean = 85.89 | abs. se = 3.91 | rel. se = 4.55 %
PMF002
Density
Cumulative frequency
D_e [Gy]

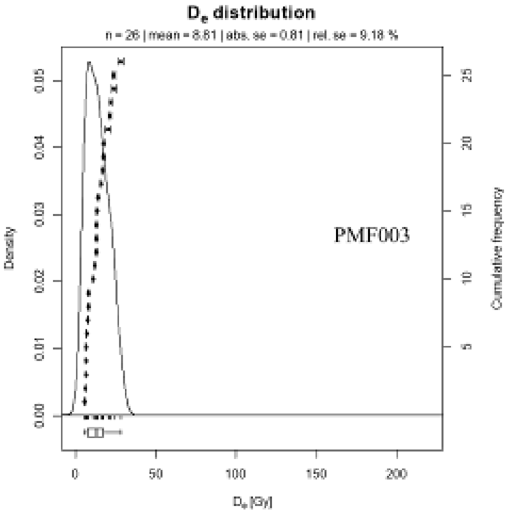
D_e distribution
n = 26 | mean = 8.81 | abs. se = 0.81 | rel. se = 9.18 %
PMF003
Density
Cumulative frequency
D_e [Gy]

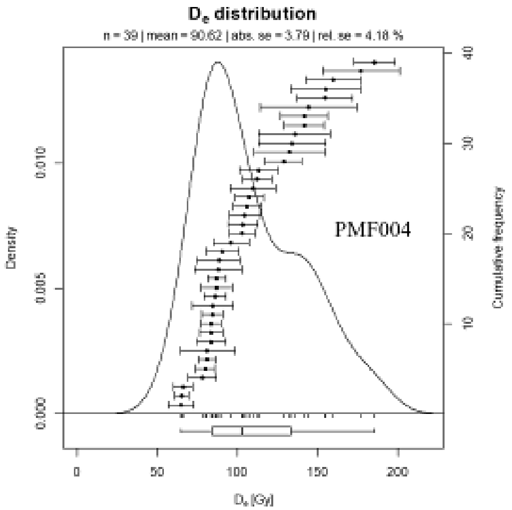
D_e distribution
n = 39 | mean = 90.62 | abs. se = 3.79 | rel. se = 4.18 %
PMF004
Density
Cumulative frequency
D_e [Gy]

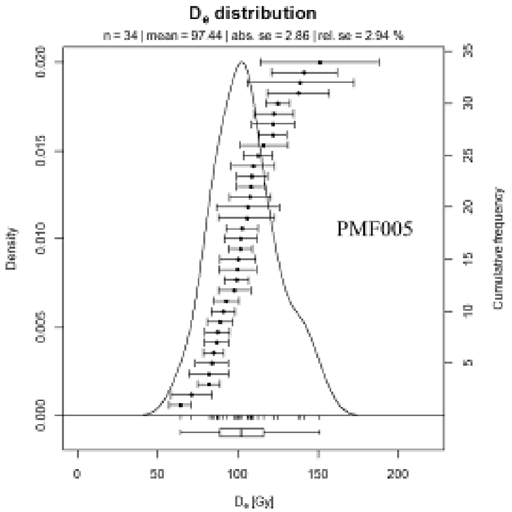
D_e distribution
n = 34 | mean = 97.44 | abs. se = 2.86 | rel. se = 2.94 %
PMF005
Density
Cumulative frequency
D_e [Gy]

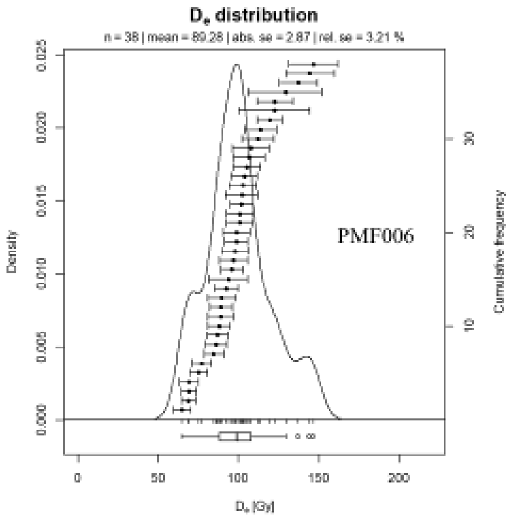
D_e distribution
n = 38 | mean = 89.28 | abs. se = 2.87 | rel. se = 3.21 %
PMF006
Density
Cumulative frequency
D_e [Gy]

Figure A2. Weighted histogram and kernel density estimate plot produced by R-Luminescence package for each PMF sample (Dietze, M., Kreutzer, S. (2017). plot_KDE(): Function version 3.5.5. In: Kreutzer, S., Dietze, M., Burow, C., Fuchs, M.C., Schmidt, C., Fischer, M., Friedrich, J. (2017).

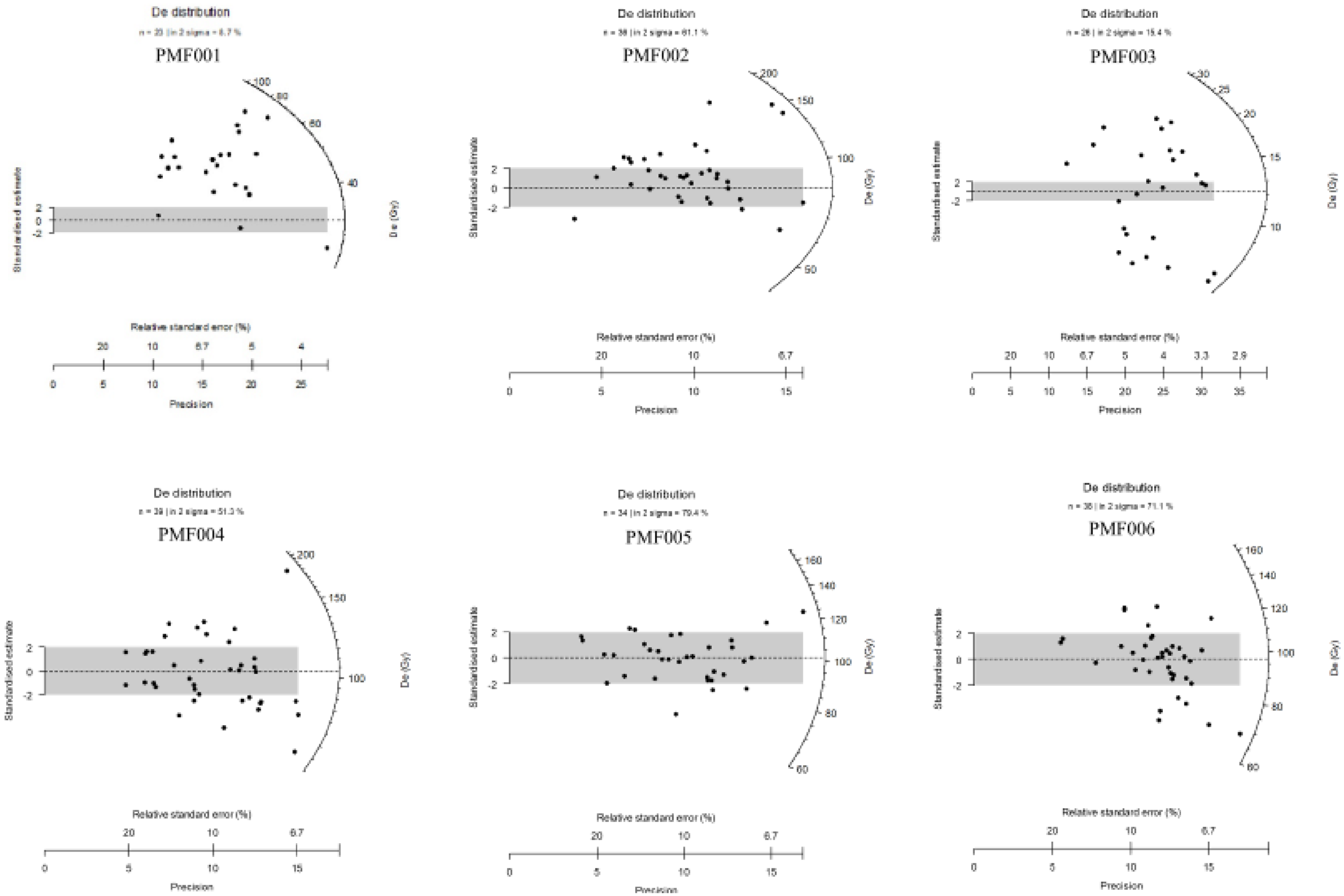

Figure A3. Radial plot generated by R-Luminescence package for each PMF sample (Dietze, M., and Kreutzer, S., 2017). plot_RadialPlot(): Function version 0.5.4. In: Kreutzer, S., Dietze, M., Burow, C., Fuchs, M.C., Schmidt, C., Fischer, M., Friedrich, J. (2017).

Appendix B. Supplementary trench data

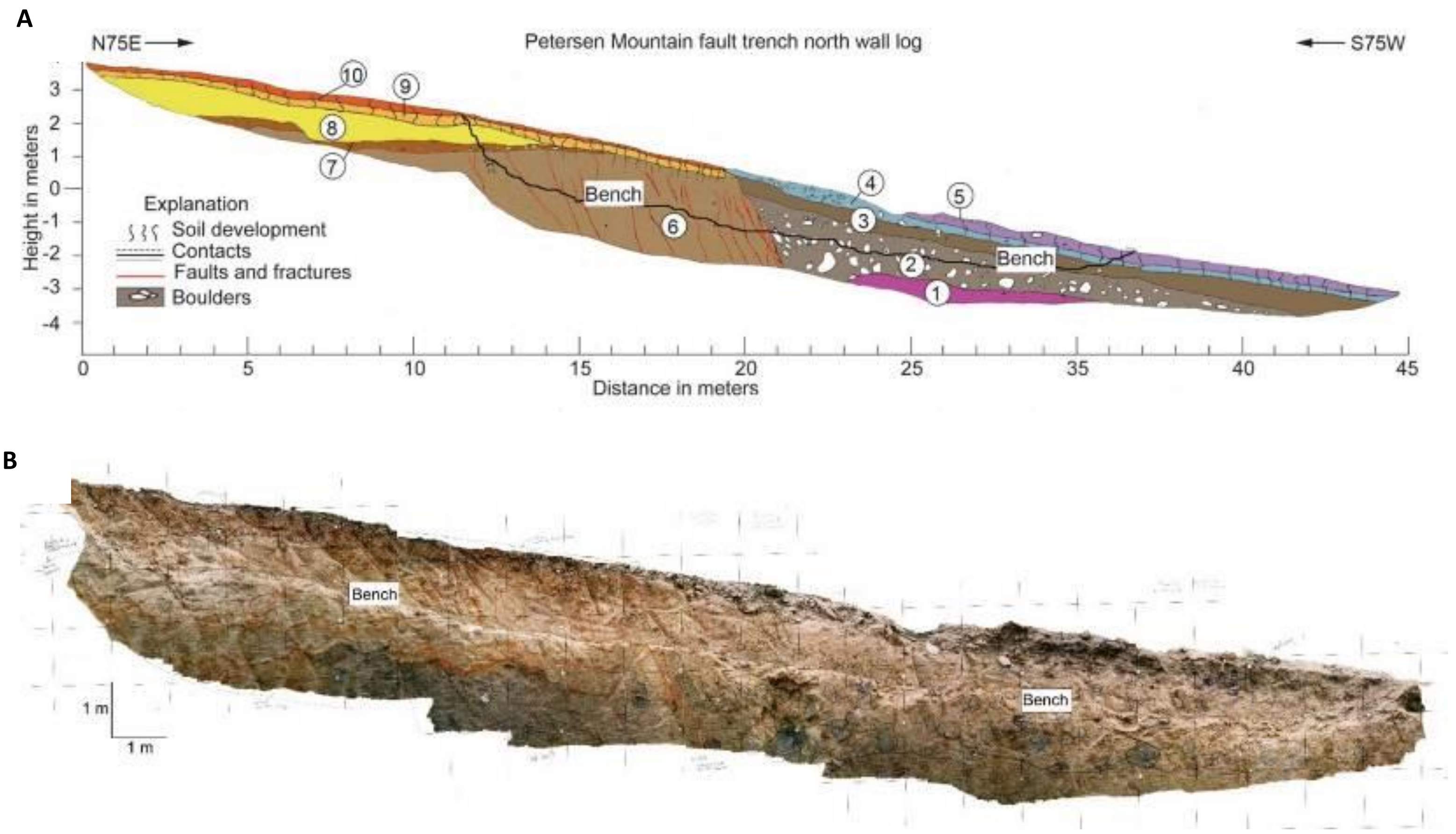

Figure B1. (A) Log of Petersen Mountain north wall trench exposure showing stratigraphic and structural relations. Open circles show unit numbers. (B) Photomosaic.

Figure B2. A) Enlarged trench photo orthomosaic of south wall with log mapping overlay at section of fault with unit labels. B) Enlarged trench photo orthomosaic of south wall with only labeled units.

Appendix B Table 1. Unit descriptions for stratigraphic deposits exposed in the trench.

Unit	Description
1	Fine to course grained loamy sand with gravel to pebbles, dark tan to yellow-brown, massive, clasts are weathered granite consistent with a diorite composition (~20% quartz, 40% feldspar, and ~40% biotite and hornblende mafic minerals) (sandy alluvium).
2	Fine to course grained sand with subrounded to rounded cobbles and boulders, tan-brown, weakly bedded, clasts are imbricated, boulders are subrounded to rounded and up to 1 m diameter, quartz diorite composition (bouldery alluvial fan).
3	Silty sand with trace cobbles, tan, sand is fine to medium grained, cobbles up to 20 cm, similar to Unit 2 but slightly finer grained (sandy alluvial fan).
4	Loamy sand, brownish-gray, sand is fine to medium grained (sandy alluvium with B-horizon soil development).
5	Loamy sand to silty sand, brownish-gray, sand is fine to medium grained (sandy alluvium mixed and aeolian silt with A-horizon soil development, similar to Unit 10).
6	Coarse sand to gravel, color ranges between gray, tan, black, and orange, grains are angular, contains discontinuous irregular, thin (2-5 cm) oxidized bands related to groundwater staining, highly fractured, massive Contains quartz, plagioclase, orthoclase, biotite and hornblende. Mineral percentages include Quartz (~25%) and feldspar (~45%), with feldspars predominantly plagioclase (~85%) consistent with the Granodiorite of Petersen Mountain (disintegrated bedrock).
7	Sand with gravel and cobbles, reddish-brown, cobbles are mixed granitic and volcanic lithologies and subrounded to subangular, matrix is medium to course grained sand (debris flow or alluvial fan deposit).
8	Medium to course grained sand with trace pebbles and cobbles, reddish brown, massive (sandy alluvial fan).
9	Fine to medium grained sand with trace pebbles and cobbles, reddish brown, massive (sandy alluvium with Bt-horizon soil development becoming sandy clay loam towards base).
10	Loamy sand to silty sand with trace pebbles and cobbles, brownish gray, massive, correlative with A-horizon developed in the hanging wall (sandy alluvium mixed and aeolian silt with A-horizon soil development, similar to Unit 5).

Appendix B Table 2. Soil descriptions from the south wall of the trench.

Depth (cm)	Horizon	Description*
Hanging wall		
0-24	A	Light brown, loamy sand, 10% gravel, single grain to weak very fine granular structure, non-sticky, non-plastic, loose to very friable consistence (m and d), no clay films, abrupt wavy basal contact.
24-45	Bw	Gray brown, loamy sand, 10% gravel, moderate medium subangular blocky structure, non-sticky, non-plastic, friable (m), slightly hard (d) consistence, no clay films, clear wavy basal contact.
45-68	BCm	Light brown, loamy sand to sand, 10% gravel, moderate medium to fine subangular blocky structure, non-sticky, non-plastic, firm (m), slightly hard (d) consistence, no clay films, cemented (silica?), gradual wavy basal contact.
68-90+	C	Yellow brown, sand, 10% gravel, single grain to weak friable subangular blocky structure, non-sticky, non-plastic, firm (m), hard (d) consistence, no clay films, cemented (silica?).
Footwall		
0-6	A	Light brown, loamy sand, <10% gravel, single grain to weak fine to medium subangular blocky structure, non-sticky, non-plastic, very friable (m), loose to weakly coherent (d) consistence, no clay films, abrupt wavy basal contact.
6-14	Bw	Brown, Sandy loam, <10% gravel, moderate medium subangular blocky structure, slightly sticky, slightly plastic, friable to firm (m), slightly hard (d) consistence, no clay films, abrupt wavy basal contact.
14-37	2Bt1	Reddish brown, Sandy clay, 10% gravel, strong, medium to course angular blocky structure, sticky, plastic, extremely firm (m), extremely hard (d) consistence, many distinct clay films on ped faces, pores, and bridges, gradual wavy basal contact.
37-55	2Bt2m	Light reddish brown, sandy clay loam, 10-25% gravel, strong medium subangular blocky structure, slightly sticky, slightly plastic extremely firm (m), extremely hard (d) consistence, many distinct clay films on ped faces, pores, and bridges, cemented (slilica?), diffuse wavy basal contact.
55-80	2Bt3m	Tan brown, sandy clay loam, 10-25% gravel, strong medium subangular blocky structure, non-sticky, slightly plastic, very firm (m), very hard (d) consistence, few, faint clay films on ped faces, cemented (silica?), gradual wavy basal contact.
80-110	Cox	Tan, sand to loamy sand, 10% gravel, weak fine to medium subangular blocky structure, non-sticky, non-plastic, very friable (m), weakly coherent (d), no clay films.

*For consistence, m, moist; d, dry

Appendix B Table 3. Orientations of faults and fractures exposed in the footwall of the trench.

Type	Measurement location*	Attitude
Primary fault plane	D	335 º /55 ºNE
Fracture	A	355º/62º
Fracture	B	352º/78º
Fracture	C	12º/74º
Fracture	E	348º/52º
Fracture	F	10º/70º
Fracture	G	2º/85º
Fracture	H	8º/75º
Fracture	I	356º/60º
Fracture	J	355º/80º

*location of fracture measurements are shown on trench log in Figure 8.

Chapter 2

Deciphering shorelines from scarps: Drone modelling and paleoseismic investigation of the Bonham Ranch Fault Zone, North of Reno, Nevada

Conni De Masi[1], Rich Koehler[1]

[1]University of Nevada Reno, Nevada Bureau of Mines and Geology

Abstract

The 56-km-long Bonham Ranch fault zone is an east-dipping normal fault zone that extends along the western side of Smoke Creek Desert, Nevada and accommodates extensional deformation along the boundary between the Walker Lane and Basin and Range tectonic provinces. The fault zone consists of several subparallel range bounding, piedmont, and intrabasin faults that cut across pluvial lake and alluvial fan deposits. The origin of some scarps in previous studies has been difficult to reconcile due to the presence of lacustrine shorelines leading to uncertainties in the total amount of displacement accommodated across the faults. Thus, to determine whether the scarps were formed by tectonic displacement or lacustrine processes, we conducted a morphological study and compared the landforms to ancient lake highstand events.

Combined observations for the Bonham Ranch fault from satellite imagery, site specific mapping utilizing Structure from Motion DTMs generated from low-altitude drone photography, as well as reconnaissance field mapping and description of stream channel outcrops, indicate that one scarp follows contour lines matching ancient shorelines associated with the mid-Holocene Neopluvial period highstand at an elevation

of ~1190-1200 m along the western margin of the basin (Adams and Rhodes, 2019). The sinuosity of the scarp, and relatively horizontal morphology of the upper and lower surfaces indicate a lacustrine shoreline origin. Two scarps located along the edge of the Smoke Creek playa strike N-S, and are characterized by linear sections, and steep scarps. Several stream exposures across these scarps show vertically offset lacustrine stratigraphy including a white tephra, indicating a tectonic origin. Faulting is also inferred to be the origin of another scarp that cuts across the Younger Dryas shorelines at elevations ~1212 m to ~1230 m (Bensen et al, 1992; Briggs et al, 2005; Adams and Rhodes, 2019). Scarp profiles along this trace indicate that the scarp is ~3 m to 6 m high. The data provided in this study indicate that surface rupturing earthquakes along the Bonham Ranch fault zone post-date the Younger Dryas shoreline and likely the Neopluvial period shorelines of mid-Holocene age.

1. Introduction

Lacustrine paleoshorelines and fault scarps have similar morphological features when briefly glanced at across a landscape. Deciphering the differences between the two formations are key in properly identifying fault scarps to characterize the fault and determine earthquake history. The goal for this study is to separate the shoreline features from fault scarps to better understand the paleoseismicity of the Bonham Ranch fault in the Smoke Creek Desert, a sub-basin of Lake Lahontan, located in the northern Walker Lane region north of Reno, Nevada.

Lake Lahontan was a large Pleistocene lake located in the Basin and Range region of the western Great Basin of northwestern Nevada, and northeastern California (Russell, 1885). It was an endorheic system with multiple sub-basins comprised of modern individual lakes such as Pyramid Lake, Honey Lake, and the lakes sustained in the Smoke Creek Desert, Black Rock Desert, and Winnemucca Dry Lake (Adams and Wesnousky, 1998; Reheis, 1999). Water level changes were controlled by seasonal input through creeks and evaporation. Thus, the regional climate heavily influenced the fluctuation of water in the basins, which altered the surrounding topography, creating shoreline features, which are preserved today on the range fronts (Benson, 1978 and 1981; Benson and Mifflin, 1986; Benson and Thompson, 1987; Benson et al., 1992). The range front and lake basins have since experienced topographic changes under the influence of active tectonics in the northern Walker Lane (Adams and Wesnousky, 1998; Adams et al., 1999). This has influenced the original elevation of lake highstand shorelines, as well as created an overprinting of fault scarps on shorelines.

The northern Walker Lane accommodates approximately 15-25% of the Pacific/North American plate boundary strain east of the Sierra Nevada through a combination of normal oblique (dextral) slip on the Sierra Nevada frontal fault system, dextral slip along northwest trending faults in the northern Walker Lane, and oblique normal-slip on north trending faults along the western margin of the Basin and Range province (Figure 1) (Faulds et al., 2005, Wesnousky, 2005; Hammond et al., 2011). The Bonham Ranch fault, located north of Reno, Nevada, is one of the westernmost normal faults of the Basin and Range and may experience dextral shearing from the Walker Lane. However, the presence of shoreline features complicates the assessment of tectonic scarps along the Bonham Ranch fault.

A previous study along the Bonham Ranch fault is a M.S. thesis (Weick, 1990) which included fault trace mapping, scarp profiling, and documentation of a stream cut exposure inferred to show tectonic graben fill sediments. The fault traces and paleoseismic data from this study are included in the USGS Quaternary faults and folds database (Adams et al., 1998). However, questions remain on the origin of some of the lineaments at the western margin of the Smoke Creek Desert which could indeed be lacustrine shorelines. Observations from stream incisions (Adams, 2010) through Quaternary deposits indicate relatively horizontal stratigraphy that lack fractures or deformation near scarps at certain locations suggesting that the scarps are erosional features and have a climatic origin rather than a tectonic origin.

In this paper, we present UAV imagery, observations of mapped morphological and stratigraphic data, and discuss the origin of topographic scarps found along the Bonham Ranch fault and Smoke Creek Desert basin (Figure 2). Structure for Motion digital terrane models with contours and slope maps were made from the UAV images to identify linear features and their respective heights, as well as stream channels for potential outcrops showing the local stratigraphy. We compared this data to previously published works on the Lahontan shorelines to decipher fault scarps from shorelines and determine the earthquake history along the Bonham Ranch fault.

2. Background

2.1. Bonham Ranch fault

The Bonham Ranch fault is an approximately 56-km-long east-dipping normal fault located along the western margin of the Smoke Creek Desert in northwestern Nevada (Figure 1) (Dodge, 1978; Weick, 1990; Adams et al, 1998). The fault is in a tectonically active region that accommodates extension between the Walker Lane and Basin and Range tectonic provinces. Right oblique displacement has been documented along north-trending normal faults within the North Valleys region of Reno, as well as along faults to the north of the Walker Lane including the Dry Valley-Smoke Creek, and Bonham Ranch fault zones (Weick, 1990; Bell and Ramelli, 2009; De Masi, 2021). It is uncertain how strain is partitioned between Walker Lane faults and Basin and Range normal faults to the northeast, however, it is possible that slip is transferred through the Bonham Ranch fault zone to the relatively young Likely fault (Potter, 1988; Bryant, 1990; Weick, 1990), an incipient northwest-trending strike-slip fault within previously extended Basin and Range crust (Figure 1). This is consistent with the theory that the Walker Lane is propagating to the north based on northward decreasing geologic displacement and geodetic strain accumulation, as well as less organized discontinuous faults to the north (Faulds et al., 2005, Wesnousky, 2005, Bormann, 2013).

Late Pleistocene slip rates in the northern Walker Lane region include 1.0 ±0.3 mm/yr for the Pyramid Lake fault (Angster et al., 2014), 1.8-2.4 mm/yr for the Warm Springs Valley fault (Gold et al., 2013), 1-2 mm/yr for the Honey Lake fault (Gold et al., 2017; Turner et al., 2008; Wills and Borchardt, 1993), and rates on the order of 0.2-0.4 mm/yr for faults in the North Valleys (Koehler, 2018; Dee et al., 2018). These studies have also placed constraints on the number, timing, and recurrence of late Pleistocene earthquakes for the region. Turner et al (2008) documented the occurrence of four earthquakes that post-date deposition of the ~7 ka Mazama Ash in a river bank exposure and determined inter-event timing of 730-990 yrs for the Honey Lake fault. Briggs et al. (2004) determined that at least four earthquakes have occurred since the desiccation of

Lake Lahontan (~15 ka) along the Pyramid Lake fault. Trenching along the Warm Springs Valley fault, indicate the occurrence of three to four late Pleistocene earthquakes with an inferred recurrence of 2,500-3,000 yrs (Chupik et al., 2021). The similar earthquake chronologies along these closely spaced faults raises the possibility of multi-fault ruptures, as has been recently considered for faults to the west in the Unified California Earthquake Rupture Forecast Model (UCERF3) (Field et al., 2013). Thus, paleoseismic parameters for faults in the region have been reasonably well documented, however the Bonham Ranch fault zone is poorly characterized and earthquake timing, recurrence, and slip rate data are few to non-existent, resulting in large uncertainties in the fault's seismic potential. One study presents a radiocarbon date for what was interpreted at the time to be graben fill. Weick (1990) states that the graben was created by a ground rupturing earthquake post ~290 yr BP. However, that particular outcrop is now covered in vegetation and slopewash and therefore the stratigraphic relations and inferred tectonic graben origin could not be confirmed. Despite this lack of data, the 2014 update of the NSHM included the Bonham Ranch fault zone using a modeled slip rate of 0.26 mm/yr (Petersen et al., 2014).

The Bonham Ranch fault zone consists of several subparallel range bounding, piedmont, and intra-basin faults that extend 56 km from the southwestern side of Smoke Creek desert near the Terraced Hills to the west flank of the Buffalo Hills (Figure 2). Fault traces were originally mapped by Bonham (1969) and later refined by Weick (1990) and Dohrenwend et al. (1991). Although Dohrenwend et al. (1991) only mapped several traces within Smoke Creek Desert, Weick (1990) showed numerous traces cutting late Pleistocene and Holocene deposits in the valley. Evidence for late Quaternary deformation in the Smoke Creek Desert includes juxtaposition of Quaternary deposits against Tertiary bedrock along range front traces, inferred single- and multiple-event scarps on latest Pleistocene lacustrine deposits and Holocene subaerial and lacustrine deposits (Weick, 1990; Adams and Sawyer, 1998).

2.2 Smoke Creek Desert

The Smoke Creek Desert is a 1,200-square-mile northeast-trending basin located ~ 100 km north of Reno, Nevada along the California-Nevada border in the eastern part of the northern Walker Lane. The basin is bounded by granitic rocks on the east and a high plateau of volcanic rocks on the west and north sides of the basin (Glancy and Rush, 1968; Maurer, 1993). Smoke Creek Desert is comprised of three sub-basins (Figure 2) based on hydrology and lithology (Ponce et al., 2006). The southern basin is located between Terraced Hills in the south, Smoke Creek to the northwest and the Fox Range to the east. The central basin is bounded with Smoke Creek on the west to just north of Buffalo Creek, and the northern Fox Range to the east. The northern basin of Smoke Creek Desert starts from the center basin and ends at about Squaw Creek and the Granite Range to the north with the Black Rock Desert and the town of Gerlach, NV to the northeast. Geophysical data indicate that basin-fill sediments are about 2 km thick (Ponce et al., 2006). The central part of the Smoke Creek Desert basin is characterized by the Mid-valley fault, a continuous linear feature striking north-south and ~18 km in length, which possibly connects with faults mapped in the Terraced Hills and southward to Pyramid Lake (Ponce et al., 2006). Alternatively, the Mid-valley fault could be part of the Bonham Ranch fault zone but is not explored in this study. A few fault scarps cut across shorelines surrounding the basin (Figure 3). The shorelines, if dated, can be used to help place age constraints on these strands of the Bonham Ranch fault.

2.3. Quaternary lake history of the Smoke Creek Desert

The Smoke Creek Desert is a sub-basin of the larger Pleistocene Lake Lahontan basin. The Lake Lahontan basin is located in western Nevada and adjacent northeastern California and is comprised of multiple sub-basins that were integrated when lake levels were high and formed separate lakes or dry terminal subbasins when lake levels were low (Reheis, 1999; Adams, 2008; Reheis et al., 2014). The modern basin is located in the Sierra Nevada rain shadow and has an arid to semi-arid climate fed by snowmelt river systems (Reheis et al, 2014). The western sub-basins of Lake Lahontan include Pyramid Lake, Honey Lake, Smoke Creek Desert, Black Rock Desert, and Winnemucca Dry Lake, and all were connected through sills of varying elevations (Figure 4) (Born, 1972; Davis, 1982; Prokopovich, 1983; Thompson et al., 1986; Hostetler, and Benson, 1990; Morrison, 1991; Benson et al., 1995; Adams and Wesnousky, 1998; Reheis, 1999; Briggs et al., 2005).

There are several lake cycles captured in the Lahontan basin. Elevations and the distributions of tephra beds were used to infer the timing of the former shoreline levels and vary per sub-basin (Davis, 1978 and 1983; Benson et al., 1997; Sarna-Wojcicki, et al., 2005; Adams, 2010). The last major highstand for Lake Lahontan was ~1335 m (Davis, 1982). The Sehoo Lake cycle began in the Lahontan basin around 35,000 ^{14}C B.P. and lasted to around 13,000 ^{14}C B.P. (15,300 cal. B.P.) (Morrison, 1991; Benson et al., 1995; Adams and Wesnousky, 1998; Adams, 2008). The elevation of the Sehoo highstand shoreline varies from ~1340 m to ~1318 m depending on the sub-basin (Adams et al., 1999; Bills et al., 2007) and now vary vertically up to 22 m due to isostatic rebound. In the Carson Sink sub-basin the Younger Dryas shoreline is found at ~1205 m and is dated to 11,300-10,400 14 C B.P. (calibrated to ~13,200-12,260 B.P.) (Benson et al., 1992) and at an elevation of ~1230-1235 m (Adams et al, 2008). In the Pyramid lake sub-basin, Briggs et al. (2005) collected a mussel shell from a beach ridge at 1212 m which was dated to 10,800 14C yr BP, overlapping with the Younger Dryas interval. According to revised data from Adams and Rhodes (2019), the Younger Dryas lake reached an elevation of about 1230 m in the western subbasins based on archaeological data and tephra deposits, this includes Pyramid Lake and the Smoke Creek Desert (Morrison and Frye, 1965; Dodge, 1980; Weick, 1990). Briggs et al. (2005) mention a lake transgression near elevation 1199 m between 3,595 and 2,635 ka in the Pyramid Lake sub-basin. This coincides with the Neopluvial period of ~4,800 to 3,400 cal yr BP (Allison, 1982; Adams and Rhodes, 2019).

Lake level cycles of importance to this study are the Sehoo Highstand, Younger Dryas, Fallon Alloformation and the Neopluvial period. The Sehoo deposits primarily consist of near shore and beach sand and gravel, shallow lake fine sand and silt, and deeper lake clay. Gravels consist of subangular to well-rounded cobbles to pebbles, and the matrix sand is poorly to moderately hardened. (Weick, 1990; Adams and Wesnousky, 1998; Adams et al., 2008). Deposits associated with the Younger Dryas are similar in composition to those associated with the Sehoo highstand. Outcrops in Smoke Creek expose the Fallon A1loformation disconformably overlying the Sehoo (Weick, 1990). The Fallon deposits typically consist of intermixed sand and silt with scattered gravel layers (Dodge, 1980). The exposed thickness of the Fallon Alloformation is about 1 to 2 m in a deeply incised gully near the distal outflow of Smoke Creek (Morrison and Frye, 1965; Dodge, 1980; Weick, 1990). The Fallon Alloformation term was used for the mid-Holocene Fallon Lake coined by Weick (1990). However, Morrison and Frye (1965) and Allison (1982) recognize a mid-Holocene lake system that consisted of alluvial, colluvial and shallow-lake deposits at similar shorelines across the Great Basin from their work in Summer Lake, Oregon and Lake Bonneville, Utah.

2.4. Shoreline and fault scarp morphology

In order to distinguish a shoreline from a fault scarp we must first differentiate the morphological processes between the two. A fault scarp is defined as a tectonic landform associated with a fault plane that has dislocated the ground surface (Stewart and Hancock, 1990). The initial scarp or fault plane right after an earthquake generally dips away from the upthrown block at an angle ranging between 50^o and vertical. Over time, the scarps break down so that scarps of about 12,000 years of age have maximum slope angles of 20^o to 25^o and slopes with angles less than 10 degrees represent ages much older than 12,000 years (Wallace, 1977). Normal fault scarps in the western USA are primarily piedmont scarps, faults that cut through poorly consolidated Quaternary sediment deposited at the base of range fronts (Adams and Wesnousky, 1998; Faulds et al., 2005; Wesnousky, 2005). The most common morphology for these types of faults consists of a steep free face ($\sim 50^o$-60^o), and a debris slope of $\sim 30^o$ (Wallace, 1977). The upper (crest) and lower (toe or base) original surfaces are the same segments separated by faulting.

A wave-formed terrace is a shoreline feature that has similar morphology to a fault scarp. Shoreline terraces have an overall flatness laterally on upper and lower surfaces (Parker et al., 1989) which is created by shore erosion and rising and lowering of water levels. Shore erosion is the wearing away of land or beach at the water's edge (Pilkey and Hume, 2001). This is accentuated during storms when waves are large due to increased winds and crash on shore with a lot of energy (Gilbert, 1890; Gulliver, 1899; Aubrey, 1979; Pilkey and Hume, 2001; Houser et al., 2008). The shallow slopes of an alluvial fan produce aerially extensive but subtle shorelines and where topography is steep, the shoreline is more likely to develop steep shoreline features (Parker and Currey, 2001). The shoreline breaks down over time through wave action, surface erosional processes or by submergence of water with rising lake levels.

Waves can also deposit sediment on the shore, leading to the accumulation of shoreline deposits. When waves deposit sand, shells, and gravel on the shoreline, a beach forms (Bluck, 1967; Orford et al, 1992; Adams and Wesnousky, 1998). Beach material can be deposited by rivers systems and move down the shoreline through wave action and longshore drift. Wave action at the shoreline also helps to sieve out minerals naturally by material density. This can create layers of well sorted minerals, dividing quartz and feldspar from micas and iron rich minerals (Hampson et al., 2008; Godsey et al., 2011; Miller et al., 2012). Lacustrine carbonate associated with shoreline tufa deposits are also common in late Pleistocene lake systems in the Great Basin (Broecker and Orr, 1958; Broecker and Kaufman, 1965; Kaufman and Broecker, 1965; Benson et al., 1995; Adams and Wesnousky, 1998; Felton et al., 2006; Godsey et al., 2011; Zimmerman et al., 2011). The wave-formed terraces are an easily recognizable shoreline feature of the Lake Lahonton sub-basin preserved in the Smoke Creek Desert.

Once a scarp or wave-formed terrace has formed, it immediately begins to change through the process of erosion. Loose clasts and fine sediment mobilize downslope from the face under the influence of gravity, rain wash, and wind and are deposited at the base of the scarp. Erosion through frost-freeze cycles also contributes to degradation of the scarp (Young, 1972; Wallace, 1977; Nash, 1980). The process of erosion is similar for both paleoshorelines and fault scarps.

3. Methods

Fault scarps, shorelines, and channel outcrops along the Bonham Ranch fault were mapped in the field aided by satellite imagery and UAV photography. A UAV survey was conducted at three sites along the Bonham Ranch fault scarp with a DJI Mavic Pro (FC220) to generate low altitude images of the sites. We used an EOS Arrow Gold RTK receiver connected to the drone by Bluetooth® for increased GPS accuracy. Due to the remote location of the Smoke Creek Desert a real-time kinematic network was not established and therefore the unit received Satellite-based Augmentation System (SBAS) corrections, differential GPS with ~16 cm horizontal accuracy, and ~26 cm vertical accuracy. There were 25 satellites in view with 17 of them used. This applies to both UAV Site A and UAV Site B (sites overlap coordinates at 40.471701° N, 119.839810°W). UAV Site A was a 630 x 648 m grid flown at a height of 50 m and speed of 9 m/sec. The flight consisted of 21 fight lines with a 60% overlap and took ~19 minutes and 28 seconds to complete.

UAV Site B was flown in two drone missions. The first flight was a 618 m x 640 m grid flown at a height of 50 m and speed of 9 m/sec. The mission was 21 flight lines and completed in 19 minutes and 38 seconds. The second flight was a 611 m x 644 m grid flown at the same specifics as the first flight mission. This mission was completed in 28 minutes and 16 seconds.

UAV Site C (40.497916°N, 119.821738°W) was flown in one mission six months after the previous surveys. Satellite-based Augmentation System (SBAS) corrections with Differential GPS had ~21 cm horizontal accuracy and ~33 cm vertical accuracy for the RTK receiver. The drone was flown at a height of 50 m and a speed of 4.7 m/sec with 60% overlap. The speed was reduced in this survey to prevent image blur. The mission was flown in a 618 m x 640 m grid with 21 flight lines in 33 minutes and 43 seconds.

The UAV flight missions were generated with programmable automatic navigation software through Pix4D Capture. The images captured from the drone were processed using Pix4D Mapper to produce a digital terrain model and photo orthomoasic for each site. Additionally, slope and contour maps were made from those models.

Scarp profiles were extracted from the UAV DTMs and from satellite imagery at select locations using ArcMap. Morphology of scarps were analytically assessed for type, a fault scarp or lake shoreline wave-formed terrace, by looking for evidence of overall flatness laterally on upper and lower surfaces, shoreline deposits, stratigraphy, and correlating elevations with Lake Lahontan highstands associated with the Seehoo and Younger Dryas.

4. Results

4.1. Drone models

We produced three Digital Terrain Models and orthomosaic images in Pix4D Mapper from SFM images captured during the drone survey (Figure 5). The DTM and orthomosaic for UAV Site A have a ground sampling resolution of 1.52 cm/pixel. UAV Site B DTM and orthomosaic models have a resolution of 1.61 cm/pixel, and UAV Site C has DTM and orthomosaic models with ground sampling resolution of 1.66 cm/pixel. From those models we created contour and slope maps to help show height changes in linear features in the topography such as shorelines and creek channels. The results are shown in Figures 6, 7, and 8.

4.2. Scarp morphology

Eleven locations were examined along the Bonham Ranch fault at three UAV flight mission sites. Nine scarp profiles were generated at UAV Sites A and B (Figures 9 and 10). Two scarp profiles were generated along the scarp in UAV Site C (Figures 11 and 12). Shorelines followed the topography with relatively flat morphology laterally of the upper and lower surfaces. Fault scarps paralleled the shoreline at elevation ~1200 m and cut through the shorelines at elevations of 1212 m (Figure 13).

The slope and height of the scarp profiles varies for each UAV flight mission site based on comparison of profiles near the margin of the Smoke Creek playa. Scarps reflect as much as ~4 m of vertical displacement and have a maximum scarp angle of ~65^{o} and a minimum of ~30^{o} for UAV sites A and B (Figure 10). UAV Site C has a scarp slope of between 65^{o} and 60^{o} with as much as 6 m of vertical displacement (Figure 12).

Figure 13 is a map of Sheepshead Spring with the DTM polygons shown for reference. Late Pleistocene-early Holocene lake shorelines are faulted between an elevation of 1212 m and 1250 m. Shorelines are shown as blue lines and blue polygons. The red lines are faults and the black lines are 50 m contours. The faults between elevation 1200 m and 1240 m cut the Younger Dryas (12,100 cal. B.P.) (Adams et al., 2008) highstand which is found in the region near ~1230 m in the Smoke Creek Desert-Lake Lahontan region.

4.3. Stratigraphy in Smoke Creek channel

We located two tephra layers at 1190 m in a stream cut perpendicular to the fault scarp (Figure 14). Identifiable exposures were ~10 meters west of the Bonham Ranch fault scarp and channel outflow into Smoke Creek Desert. The outcrop is ~ 168 cm thick (Figure 14). The lowermost deposits (Unit 1) primarily consist of fine to medium sand and silt with sparse gravel layers, and deeper lake fine sand and clay, similar to the Sehoo highstand deposits (Weick, 1990; Adams and Wesnousky, 1998; Adams et al., 2008). Above those sediments are the two tephra layers that are found within a 40 cm thick bed. The lowermost tephra layer is ~6 cm thick (Unit 2) within the base of a ~20 cm thick silty sand layer with gravel lenses (Unit 3) topped with an evaporite deposit with a thickness of ~1 cm (Unit 4). This ash contains many white crystalline tubular glass shards that are 1 mm or less in size and are well sorted. Overlying the evaporite deposit is a ~19 cm thick blocky fine sand and clay layer (Unit 5) which underlies a ~2 cm thick tephra layer (Unit 6). The uppermost ash layer contains glass shards that are ~1 mm to 3 mm in size with a reddish color and is mixed with clay, quartz and feldspar. Above the tephra beds is a 50 cm deposit consisting of subangular coarse sand intermixed with silt and pebbles (Unit 7).

5. Discussion

The two tephra layers exposed in the stream cut of Smoke Creek occur at an elevation of 1190 m, lower than the highstands associated with the Sehoo and Younger Dryas shorelines (Weick, 1990) and possibly at the highstand elevation of Neopluvial period deposits. According to Adams, 2010, the Trego Hot Springs ash is found in Squaw Creek at 1254 m and in Smoke Creek at 1218 m. Our tephra site was 4.6 km downstream (east) of the Adams site near the mouth of Smoke Creek just before entering the modern river plane and lake playa (Figure 15). Based on the thickness of the tephra beds, ash composition, and underlying clay deposit similar to that found upstream in the Smoke Creek channel (Adams, 2010), this exposure of tephra could be the Trego Hot Springs and Wono ash beds that were deposited during the Seehoo highstand around 23,400 ^{14}C B.P. (Davis, 1983; Benson et al., 1997).

The tephra layers could also correlate to the Mazama Ash, which has been correlated by elevation in southern Pyramid Lake and found in proximity to the Younger Dryas paleoshorelines. The Mazama and Tsoyawata tephra beds are both found in fine-grained sediments ponded by the 1202 m beach ridge near the Coleman archaeological locality in the northern Winnemucca Dry Lake (Adams et al., 2008). The ages of the Mazama and Tsoyawata tephras are ~6845 ^{14}C B.P. (7730 cal. B.P.) and 7015 ^{14}C B.P. (7840 cal. B.P.) (Bacon, 1983; Zdanowicz wt al., 1999). The Mazama tephra is found within the Nixon terrace at an elevation of ~1198 m (Bell et al., 2005). Lake level was rising around 10,160–9560 cal. B.P through an elevation of 1168 m in northwest Pyramid Lake and may have attained that elevation near Emerson Pass and spilled into the Smoke Creek Desert (Adams et al., 2008). This increase in water level is constrained by the age of the Nixon fluvial terrace that grades to an elevation near 1200 m (Bell et al., 2005), and the presence of the Mazama and Tsoyawata tephras ponded behind the 1202 m beach ridge at the north end of Winnemucca Dry Lake (Adams et al., 2008).

Based on sediment type and stratigraphic relations to previously dated Trego Hot Springs ash further up Smoke Creek and the Wono tephra in Squaw Creek (Adams, 2010), it is likely that the ash exposed in this section of the channel correlates to the Trego Hot Springs and Wono tephras and not the Mazama or Tsoyawata, deposit being at an elevation of 1190 m. Because the ash deposits are below a surface cut by the fault, faulting occurred after 23,400 years ago. However, deposits above the ash in the exposure may be contemporaneous with a shoreline associated with the Neopluvial period (~4,800–3,400 cal yr BP) at ~1190 m (Adams and Rhodes, 2019). Although the shoreline is not offset by the fault, the fault does cut the surface, and the surficial deposits downstream from the shoreline are likely Neopluvial in age. Furthermore, the extension of the scarp to the north cuts across shorelines associated with the Younger Dryas highstand. Thus, we infer the occurrence of at least one earthquake that postdates ~12 ka to ~3.4 ka along this strand of the Bonham Ranch fault.

The fault scarp that parallels the playa margin south of Smoke Creek to south of Buffalo Creek has varying heights (Figure 2, and scarp profiles in Figures 10 and 12). In the south near Sheepshead Spring, the scarp height ranges from 1 m to 3 m, and in UAV Site C, south of Buffalo Creek, the scarp height jumps up to between 4.5 m to 7 m, while the majority of the scarp is ~1-2 m along its entire length. According to Weick (1990) single event scarps along the Bonham Ranch fault are 1 m to 2.9 m in height. Based on the height of the scarp along this section (4 to 6 meters), it is possible that more than one earthquake has occurred in the last ~3.4 ka, however we do not have stratigraphic data to support this possibility. It is unclear if the part of the fault that has larger scarps is a reflection of more frequent or more recent earthquakes, variable displacement along the trace of the fault, or if there has been more incision along the margin of the playa in this location due to river input from Buffalo and Smoke Creeks.

6. Conclusions

We were able to distinguish shorelines from fault scarps by looking at the overall flatness laterally of the upper and lower surfaces of the scarps, the way they followed the topography or cut through it, and by cross cutting relationships between the shorelines and fault. We were then able to correlate previous studies of the Trego Hot Springs and Wono ash layers and the Neopluvial and Younger Dryas lake-level highstands in the region to match tephra bed stratigraphy and highstand elevations along the Smoke Creek channel located on the western margin of the Smoke Creek Desert for age control along the Bonham Ranch fault. We compared the results of scarp heights in this study to that of the previous Weick study to suggest the possibility that more than one earthquake has occurred along this trace of the fault. The stratigraphic and geomorphic observations support the occurrence of at least one earthquake that postdates ~3.4 ka. Thus, the Bonham Ranch fault is an active extensional structure along the western margin of the Basin and Range.

Acknowledgements

Funding for this project was provided from USGS NEHRP Cooperative Agreement

#G20AP00014.

References

Adams, K.D.,and Sawyer, T.L., compilers, 1998, Faut number 1601, Bonham Ranch fault zone, in Quaternary fault and fold database of the United States: U.S. Geological Survey website, https://earthquakes.usghs.gov/hazards/qfaults, accessed 12/14/2020.

Adams, K.D., and Wesnousky, S.G.,1998, Shoreline processes and the age of the Lake Lahontan highstand in the Jessup embayment, Nevada. Geological Society of America Bulletin, 110, 1318–1332.

Adams, K.D., Goebel, T., Graf, K., Smith, G.M., Camp, A.J., Briggs, R.W., and Rhode, D.,2008, Late Pleistocene and early Holocene lake-level fluctuations in the Lahontan Basin, Nevada: Implications for the distribution of archaeological sites. Geoarchaeology, 23(5), 608- 643.

Adams, K.D., and Rhodes, E.J., 2019, Late Pleistocene to present lake-level fluctuations at Pyramid and Winnemucca lakes, Nevada, USA: Quaternary Research, v. 92, p. 146-164.

Allison, I.S., 1982. Geology of Pluvial Lake Chewaucan, Lake County, Oregon. Oregon State University Press, Corvallis.

Angster, S., Huang, W., Wesnousky, S.G., Kent, G., Nakata, T., and Goto, H., 2014, Earthquake size and slip rate of the Pyramid Lake fault zone near Reno, Nevada, NEHRP Final Technical Report, G13AP00033, 22 p.

Aubrey, D.G., 1979, Seasonal patterns of onshore/offshore sediment movement. Journal of Geophysical Research 84, 6347–6354.

Bell, J.W., and Ramelli, A.R., 2009, Active fault controls at high-temperature geothermal sites: Prospecting for new faults, GRC Transactions, vol. 33, p. 425-429.

Bell, J.W., Caskey, S.J., and House, P.K., 2009, Geologic map of the Lahontan Mountains quadrangle, Churchill County, Nevada (second edition), Nevada Bureau of Mines and Geology, Map 168.

Benson, L.V., 1978, Fluctuations in the level of pluvial Lake Lahontan during the last 40,000 years. Quaternary Research, 9, 300–318.

Benson, L.V., 1981, Paleoclimatic significance of lake-level fluctuations in the Lahontan Basin. Quaternary Research, 16, 390–403.

Benson, L.V., Currey, D.R., Lao, Y., & Hostetler, S.W. (1992). Lake-size variations in the Lahontan and Bonneville basins between 13,000 and 9000 14C yr B.P. Palaeogeography, Palaeoclimatology, Palaeoecology, 95, 19–32.

Benson, L.V., & Mifflin, M.D.,1986, Reconnaissance bathymetry of basins occupied by Pleistocene Lake Lahontan, Nevada and California. U.S. Geological Survey Water Resources Investigations Report 85-4262, 14.

Benson, L.V., & Thompson, R.S.,1987, The physical record of lakes in the Great Basin. In W.F. Ruddiman & H.E. Wright, Jr. (Eds.), North America and adjacent oceans during the last deglaciation (pp. 241–260). Boulder, CO: Geological Society of America.

Benson, L.V., Kashgarian, M., and Rubin, M., 1995, Carbonate deposition, Pyramid Lake subbasin, Nevada. 2. Lake levels and polar-jet stream positions reconstructed from radiocarbon ages and elevations of carbonates (tufas) deposited in the Lahontan Basin: Palaeogeography, Palaeoclimatology, Palaeoecology, v. 117, p. 1–30.

Benson, L.V., Smoot, J.P., Kashgarian, M., Sarna-Wojcicki, A.M., Burdett, J.W., 1997, Radiocarbon ages and environments of deposition of the Wono and Trego Hot Springs tephra layers in the Pyramid Lake subbasin, Nevada. Quaternary Research 47, 251–260.

Bluck, B. J., 1967, Sedimentation of beach gravels: Examples from South Wales: Journal of Sedimentary Petrology, v. 37, p. 128–156.

Bonham, H.F., 1969, Geology and mineral deposits of Washoe and Storey counties, Nevada, with a section on industrial rock and mineral deposits by K.G. Papke: Nevada Bureau of Mines and Geology Bulletin 70, 139 p.

Bormann, J., 2013, New insights into strain accumulation and reléase in the central and northern Walker Lane, Pacific-North American plate boundary, California and Nevada, USA, Ph.D. dissertation, August 2013, University of Nevada, Reno.

Born, S.M., 1972, Late Quaternary history, deltaic sedimentation, and mudlump formation at Pyramid Lake, Nevada. Reno, NV: Center for Water Resources, Desert Research Institute.

Briggs, R.W. and Wesnousky, S.G., 2004, Late Pleistocene fault slip rate, earthquake recurrence, and recency of slip along the Pyramid Lake fault zone, northern Walker Lane, United States: Journal of Geophysical Research-Solid Earth, v. 109, no. B8, 16 p.

Briggs, R.W., Wesnousky, S.G., & Adams, K.D., 2005, Late Pleistocene and late Holocene lake highstands in the Pyramid Lake subbasin of Lake Lahontan, Nevada, USA. Quaternary Research, 64, 257–263.

Broecker, W. S., and Orr, P. C., 1958, Radiocarbon chronology of Lake Lahontan and Lake Bonneville: Geological Society of America Bulletin, v. 69, p. 1009–1032.

Broecker, W. S., and Kaufman, A., 1965, Radiocarbon chronology of Lake Lahontan and Lake Bonneville II, Great Basin: Geological Society of America Bulletin, v. 76, p. 537–566.

Bryant, W.A., 1990, Likely fault zone, Lassen and Modoc Counties: California Division of Mines and Geology Fault Evaluation Report 218.

Chupik, C., Koehler, R., and Keen-Zebert, A., 2021, Complex Holocene Fault Ruptures on the Warm Springs Valley Fault in the Northern Walker Lane, Nevada–Northern California. *Bulletin of the Seismological Society of America* 2021; doi:https://doi.org/10.1785/0120200271.

Davis, J.O., 1978. Quaternary tephrochronology of the Lake Lahontan area, Nevada and California. University of Nevada, Nevada Archeological Survey Research Paper 7.

Davis, J.O.,1982, Bits and pieces: The last 35,000 years in the Lahontan basin. In D.B. Madsen & J.F. O'Connell (Eds.), Man and environment in the Great Basin (pp. 53–75). Society of American Archeology Papers No. 2.

Davis, J.O.,1983, Level of Lake Lahontan during deposition of the Trego Hot Springs tephra about 23,400 years ago. Quaternary Research, 19, 312–324.

Dee, S., Ramelli, A.R., and Koehler, R.D., 2018, Pilot paleoseismic investigation of faults in the North Valleys, Reno, NV, Final Technical Report, U.S. Geological Survey National Earthquake Hazards Reduction Program (Award # G16AP00060).

De Masi, C., Koheler., R., Dee., S., and Keen-Zebert, A., 2021, Early development of strike-slip faulting: Paleoseismic study along the Petersen Mountain fault, northern Walker Lane, Nevada, Journal of Quaternary Science. Vol. 36, No. 3, p. 403-414.

Dohrenwend, J.C., McKittrick, M.A., and Moring, B.C., 1991, Reconnaissance photogeologic map of yound faults in the Lovelock 1°X 2°quadrangle, Nevada and California, U.S. Department of the Interior, U.S. Geological Survey Miscellaneous Field Studies Map, MF-2178.

Faulds, J.E., Henry, C.D., and Hinz, N.H., 2005, Kinematics of the northern Walker Lane: An incipient transform fault along the Pacific-North American plate boundary, Geology, 33, 505-508.

Felton, A., Jewell, P.W., Chan, M., and Currey, D., 2006, Controls of tufa development in Pleistocene Lake Bonneville, Utah: The Journal of Geology, v. 114, p. 377–389.

Field, E.H., and 17 others, 2013, Uniform California earthquake rupture forecast, version 3 (UCERF3) – The time-independent model: U.S. Geological Survey Open-File Report 2013-1165, 97 p.

Gilbert, G. K., 1890, Lake Bonneville. United States: U.S. Government Printing Office.

Glancy, P.A., and Rush, F.E., 1967, Water-resources appraisal of Smoke Creek-San Emidio Desert Area Nevada and California, United States Geological Survey and U.S. Department of the Interior, Report 44, 82 p.

Godsey, H.S., Oviatt, C.G., Miller, D.M., and Chan, M.A., 2011, Stratigraphy and chronology of offshore to nearshore deposits associated with the Provo shoreline, Pleistocene Lake Bonneville, Utah: Palaeogeography, Palaeoclimatology, Palaeoecology, v. 310, p. 442–450, doi:10.1016/j.palaeo.2011.08.005.

Gold, R.D., dePolo, C.M., Briggs, R.W., Crone, A.J., and Gosse, J., 2013, Late Quaternary slip-rate variations along the Warm Springs Valley fault system, northern Walker Lane, California- Nevada border, Bulletin of the Seismological Society of America, v. 103, no 1, p. 542-558.

Gulliver, F.P., 1899, Proceedings of the American Academy of Arts and Sciences, Vol. 34, No. 8, pp. 151-258.

Hampson, G., Rodriguez, A., Storms, J., Johnson, H., & Meyer, C., 2008, Geomorphology and High-Resolution Stratigraphy of Progradational Wave-Dominated Shoreline Deposits: Impact on Reservoir-Scale Facies Architecture. Recent advances in models of siliciclastic shallow-marine stratigraphy: SEPM Special Publication. 90. 117-142. 10.2110/pec.08.90.0117.

Hostetler, S., and Benson, L., 1990, Paleoclimatic implications of the high stand of Lake Lahontan derived from models of evaporation and lake level. *Climate Dynamics* **4,** 207–217. https://doi.org/10.1007/BF00209522.

Kaufman, A., and Broecker, W. S., 1965, Comparison of Th^{230} and ^{14}C ages for carbonate materials from Lakes Lahontan and Bonneville: Journal of Geophysical Research, v. 70, p. 4039–4054.

Maurer, D.K., 1993, Hydrogeologic setting and hydrologic data of the Smoke Creek Desert Basin, Washoe County, Nevada, and Lassen County, California, water years 1988-1990, United States Geological Survey, Water-Resources Investigations Report 93-4043, 50 p.

Miller, D.M., Oviatt, C.G., and McGeehin, J.P., 2013, Stratigraphy and chronology of Provo shoreline deposits and lake-level implications, late Pleistocene Lake Bonneville, eastern Great Basin, USA. *Boreas, 42,* 342–361.

Morrison, R.B. and Frye, J.C., 1965, Correlation of the middle and Late Quaternary successions of the Lake Lahonton, Lake Bonneville, Rocky Mountain (Wasatch Range), southern Great Plains and Eastern Midwest area: Nevada Bureau of Mines Report 9, 45 p.

Morrison, R.B., 1991, Quaternary stratigraphic, hydrologic, and climatic history of the Great Basin, with emphasis on Lake Lahontan, Bonneville, and Tecopa. In R.B. Morrison (Ed.), Quaternary nonglacial geology: Conterminous U.S. pp. 283–320. Boulder, CO: Geological Society of America.

Nash, D.B., 1980, Morphologic Dating of Degraded Normal Fault Scarps, The Journal of Geology, Vol. 88, No. 3, pp. 353-360.

Orford, J. D., Carter, R. W. G., and Jennings, S. C., 1991, Coarse clastic barrier environments: Evolution and implications for Quaternary sea level interpretation: Quaternary International, v. 9, p. 87–104.

Parker, T.J., Saunders. R.S., and Schneeberger, D.M., 1989, Transitional morphology in west Deuteronilus Mensae, Mars: Implications for modification of the lowland/upland boundary, Icarus, 82, 111 – 145.

Parker, T.J., and Currey, D.R., 2001, Extraterrestrial coastal geomorphology, Geomorphology, v.37, pp.303-328.

Peterson, M.D., and 18 others, 2014, Documentation for the 2014 update of the United States national seismic hazard maps, U.S. Geological Survey Open-File Report 2014-1091, 243 p.

Pilkey, O.H. and Hume, T.M., 2001, The shoreline erosion problem: lessons from the past. Water and Atmosphere, *9*(2), pp.22-23.

Ponce, D., Glen, J., and Tilden, J., 2006, Geophysical investigations of the Smoke Creek Desert and their geologic implications, Northwest Nevada and Northeast California, United States Geological Survey, Open-File Report 2006-1176, 29 p.

Potter, S.L., 1988, Geology of the northern portion of the Likely fault lineament, Modoc County, northeastern California: Arcata, California, Humboldt State University, unpublished M.S. thesis, 55 p.

Prokopovich, N.P., 1983, Alteration of alluvium by natural gas in the Pyramid Lake area, Nevada. Bulletin of the Association of Engineering Geologists, 20, 185–196.

Reheis, M., 1999, Highest Pluvial-Lake Shorelines and Pleistocene Climate of the Western Great Basin. Quaternary Research, 52(2), 196-205.

Russell, I.C., 1885, Geological history of Lake Lahontan, a Quaternary lake in northwestern Nevada. U.S. Geological Survey Monographs 11.

Sarna-Wojcicki, A.M., Reheis, M.C., Pringle, M.S., Fleck, R.J., Burbank, D.W., Meyer, C.E., Slate, J.L., Wan, E., Budahn, J.R., Troxel, B., Walker, J.P., 2005, Tephra layers of blind Spring Valley and related upper Pliocene and Pleistocene tephra layers, California, Nevada, and Utah: isotopic ages, correlation, and magnetostratigraphy. USGS Professional Paper 701.

Thompson, R.S., Benson, L.V., & Hattori, E.M., 1986, Arevised chronology for the last Pleistocene lake cycle in the central Lahontan basin. Quaternary Research, 25, 1–9.

Weick, R.J., 1990, Structural, tectonic and Quaternary study of the eastern Madeline Plains, California and southwestern Smoke Creek Desert, Nevada: Reno, University of Nevada, unpublished M.S. thesis, 160 p., 5 plates.

Wesnousky, S.G., 2005, Active faulting in the Walker Lane, Tectonics, 24, TC3009.

Young, A., 1972, Slopes: Edinburgh, Oliver and Boyd, 288 p.

Zimmerman, S.R.H., Hemming, S.R., Hemming, N.G., Tomascak , P.B., and Pearl, C., 2011, High-resolution chemostratigraphic record of late Pleistocene lake level variability, Mono Lake, California: Geological Society of America Bulletin, v. 123, p. 2320–2334, doi:10.1130 /B30377.

FIGURES

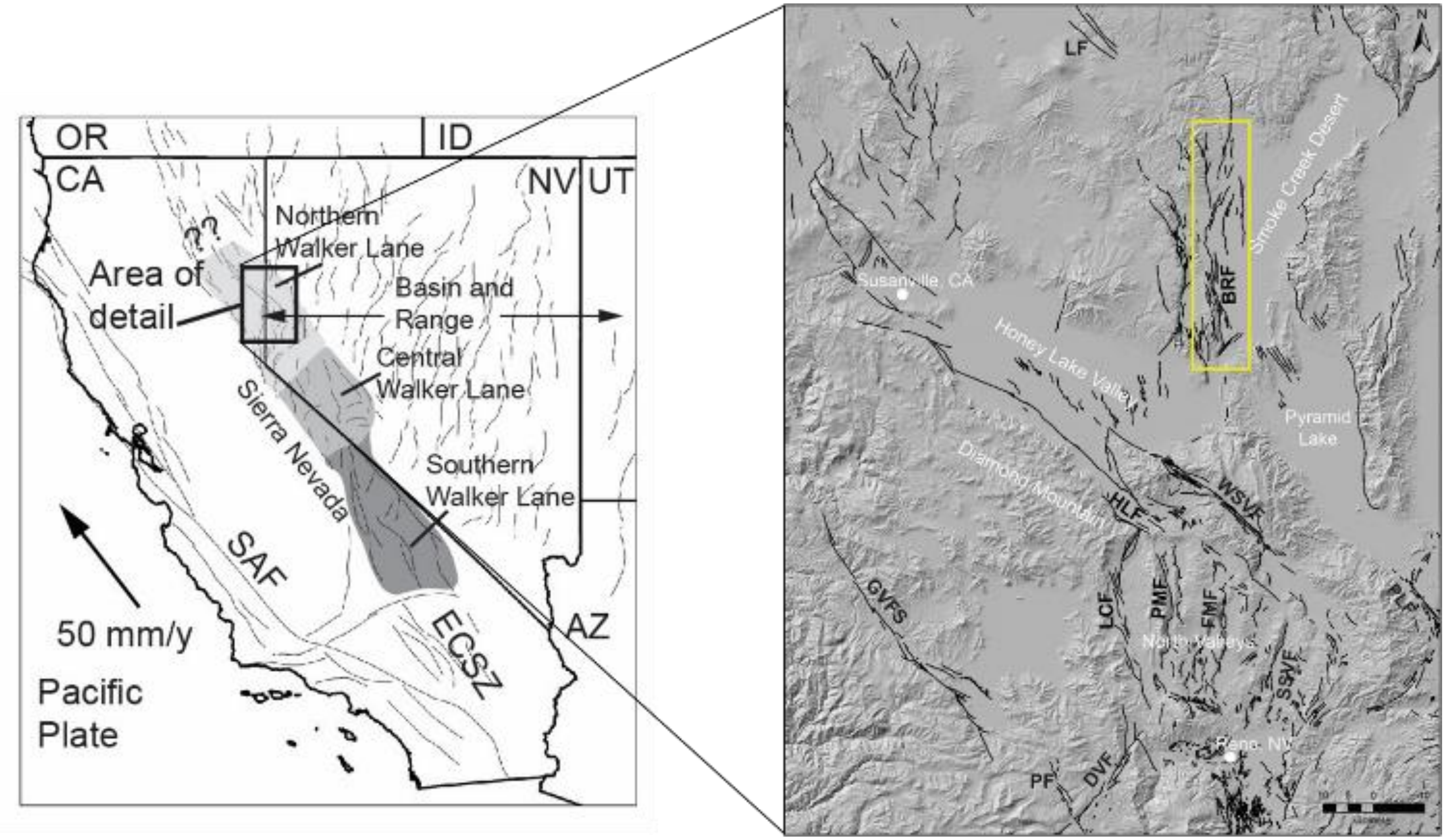

Figure 1. The shaded relief map of the northern Walker Lane, located to the right, shows project locations outlined in yellow boxes, and regional faults. [BRF, Bonham Ranch fault; DVF, Dog Valley fault; FMF, Freds Mtn fault; MVFZ, Mohawk Valley fault zone; HLF, Honey Lake fault; LCF, Last Chance fault; LF, Likely fault; PMF, Petersen Mtn fault; PF, Polaris fault; PLF, Pyramid Lake fault; SSVF, Spanish Springs Valley fault; WSVF, Warm Springs Valley fault.]

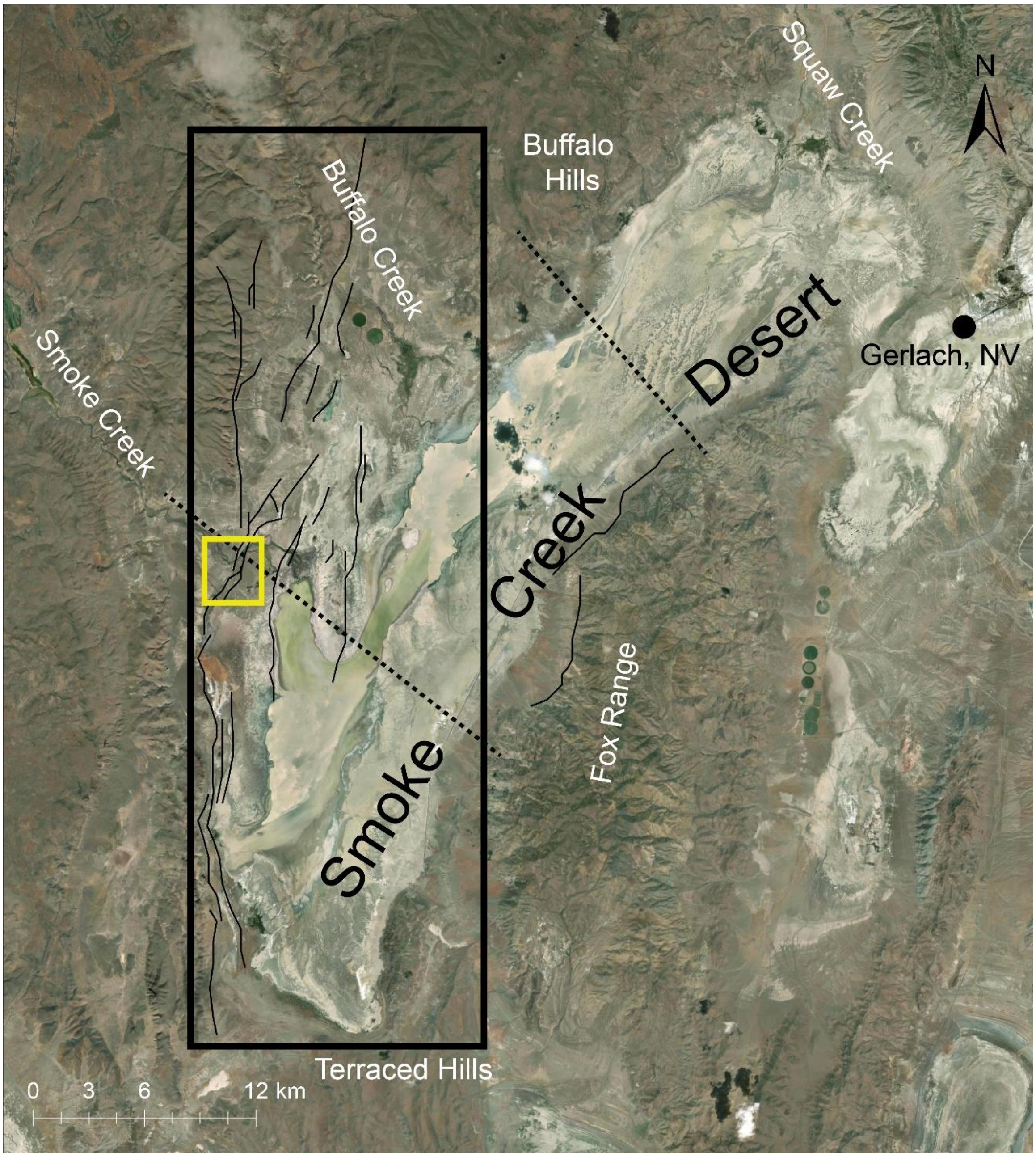

Figure 2. Satellite image of Smoke Creek Desert: Black box outlines Bonham Ranch Fault Zone and the Yellow box outlines location of Figure 3. Black dashed lines separate the southern, central, and northern basins. Faults are in solid black lines.

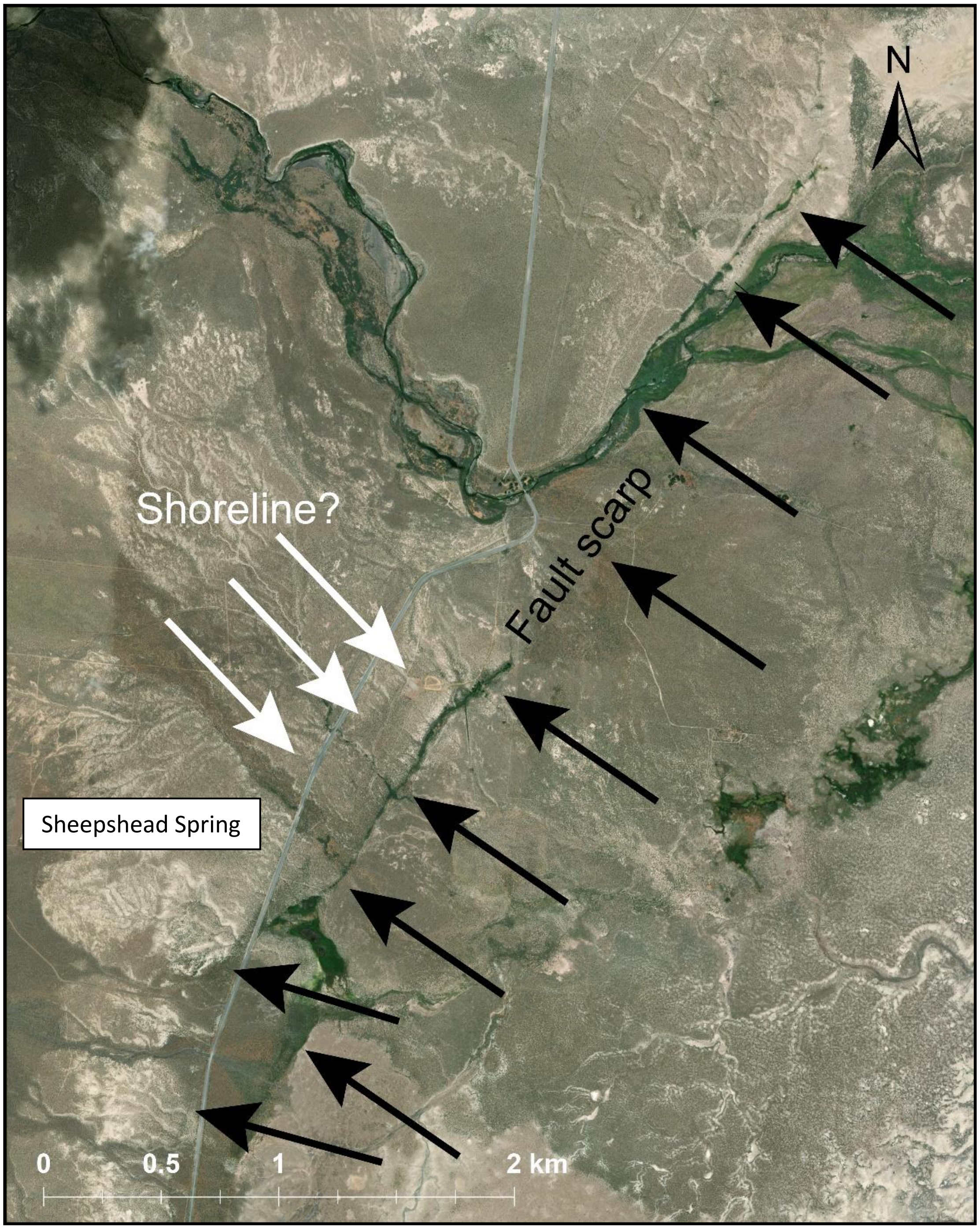

Figure 3. Satellite image of the Sheepshead Springs area. Black arrows indicate fault scarp. White arrow indicates shoreline.

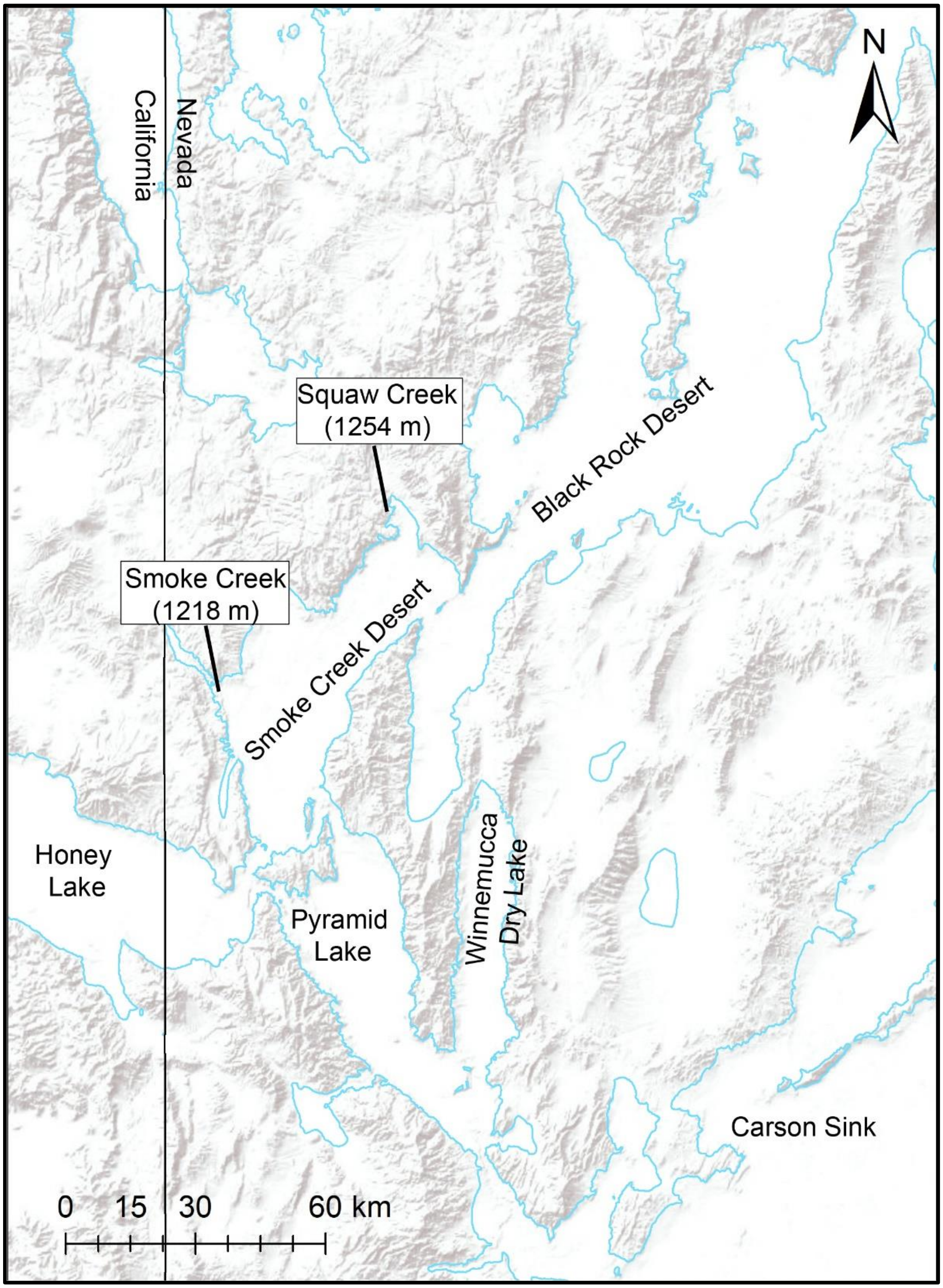

Figure 4. Blue lines outline the late Pleistocene highstand of Lake Lahontan sub-basins in the western Great Basin. White boxes mark locations of Trego Hot Springs and Wono ash layers (modified from Adams, 2010) in the Smoke Creek Desert.

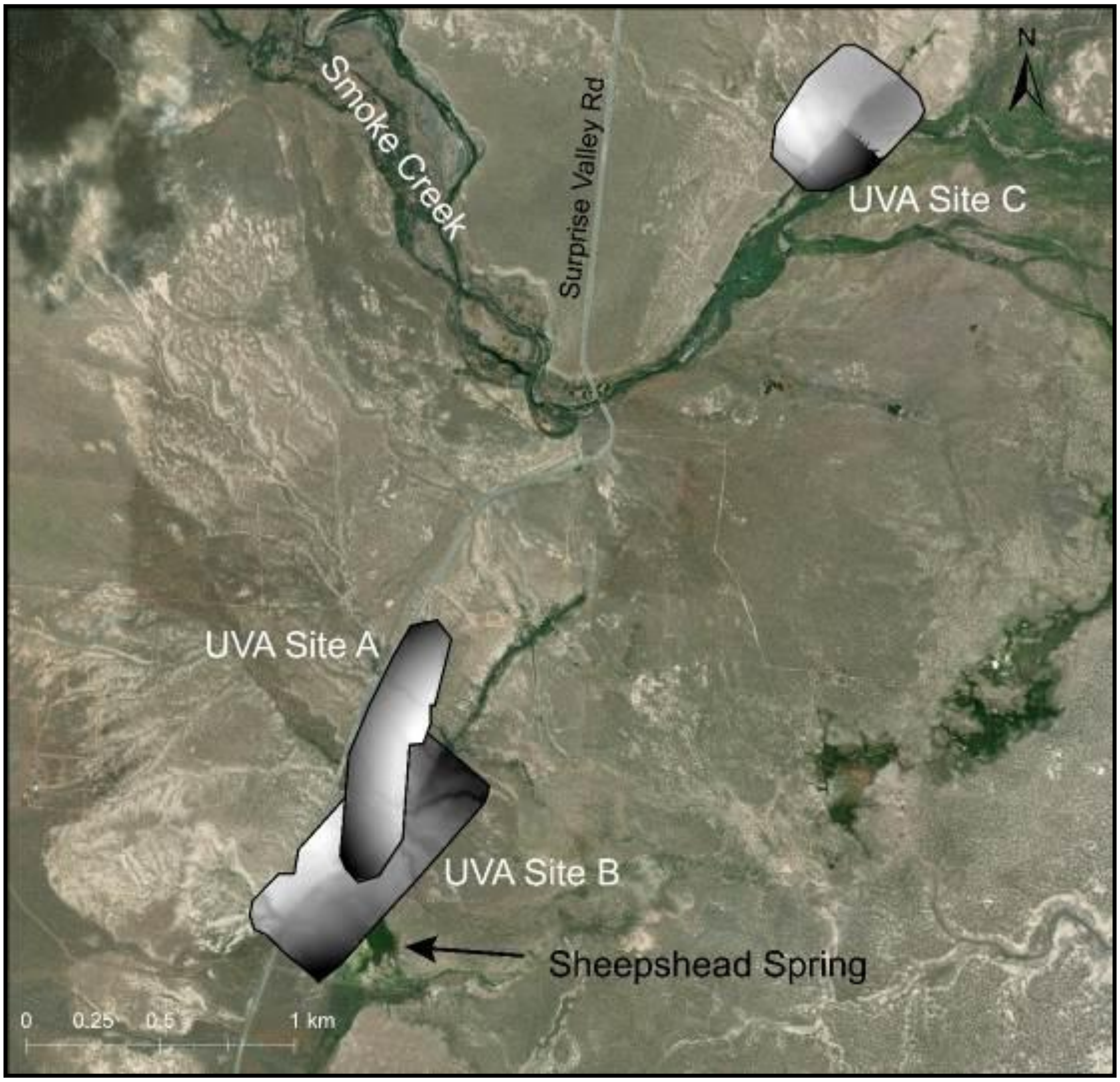

Figure 5. Satellite image with UVA mission flight sites shown as digital terrain models.

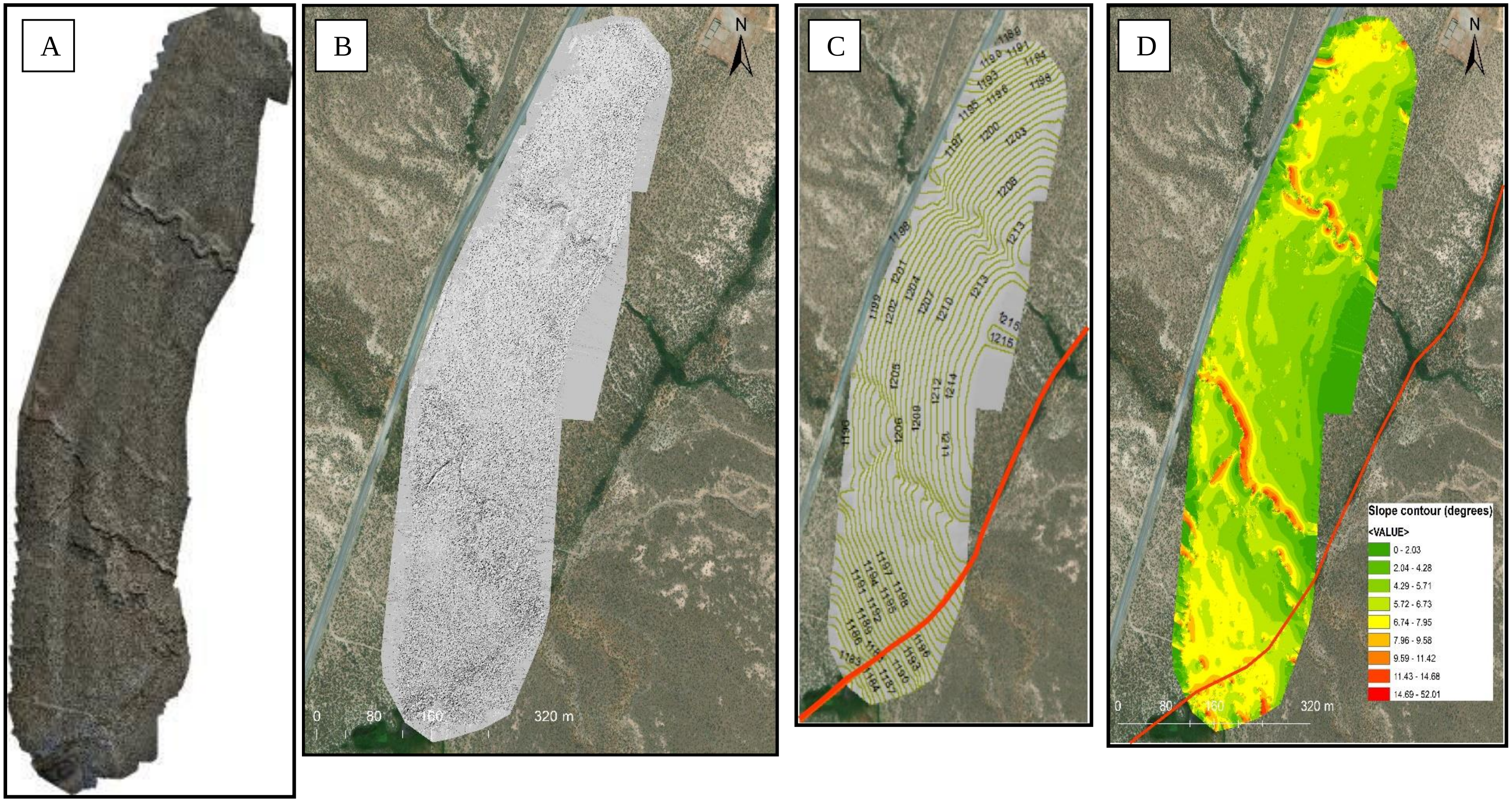

Figure 6. UAV flight mission site A. A) Orthomosaic B) Hillshade over digital terrain model C) Contour map with 1 meter contours D) Slope map: Green represents gentle slopes, then turns to yellow, orange and red as the slope gets steeper. Red line in C and D is interpreted location of the Bonham Ranch fault.

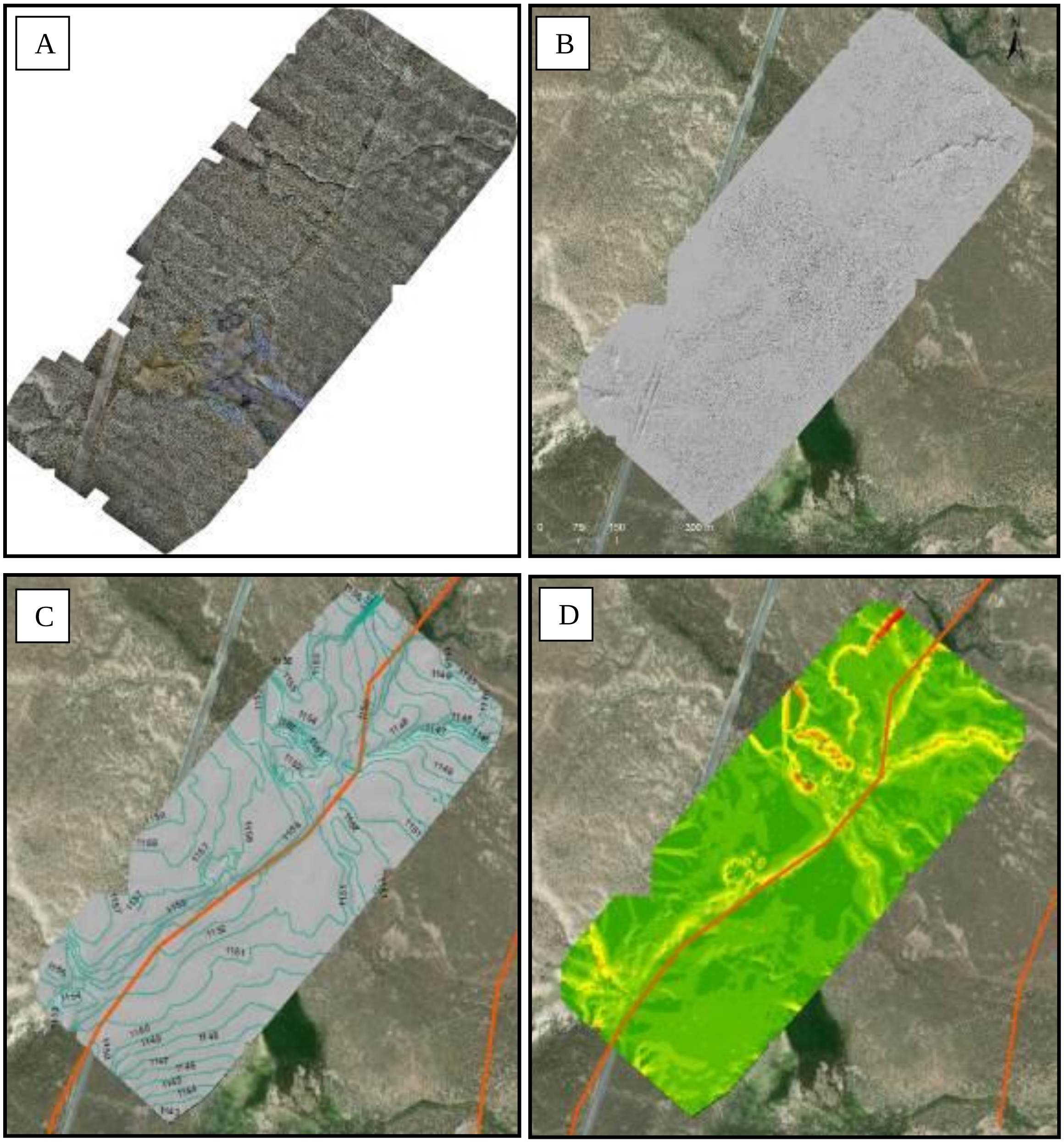

Figure 7. UAV flight mission site B. A) Orthomosaic B) Hillshade over digital terrain model C) Contour map with 1 meter contours D) Slope map: Green represents gentle slopes, then turns to yellow, orange and red as the slope gets steeper.

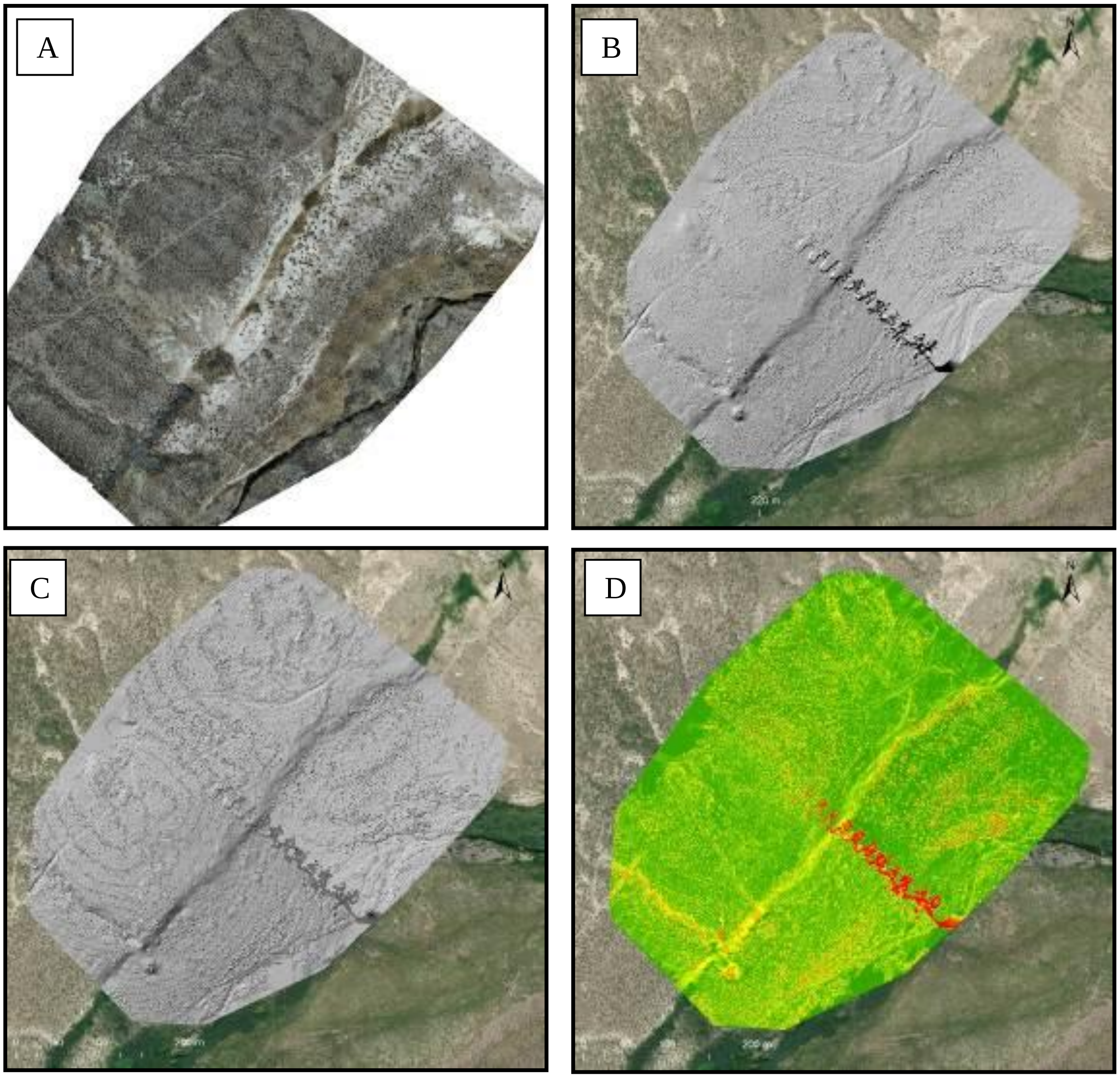

Figure 8. UAV flight mission site C. A) Orthomosaic B) Hillshade over digital terrain model C) Contour map with 1 meter contours D) Slope map: Green represents gentle slopes, then turns to yellow, orange and red as the slope gets steeper. The zipper looking feature trending NW-SE is due to flight height adjustment after battery change.

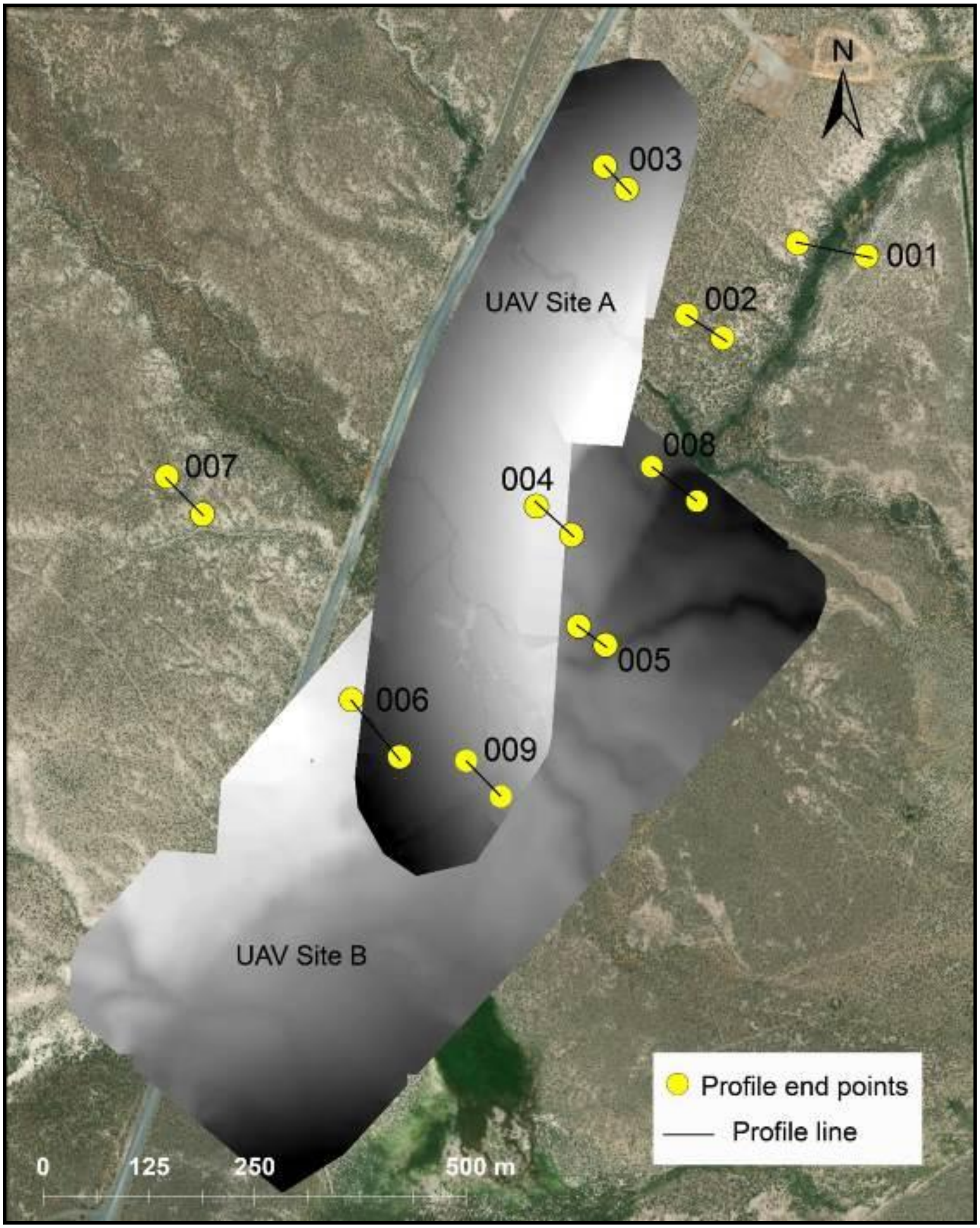

Figure 9. UAV DTM for flight mission Sites A and B with scarp profile lines.

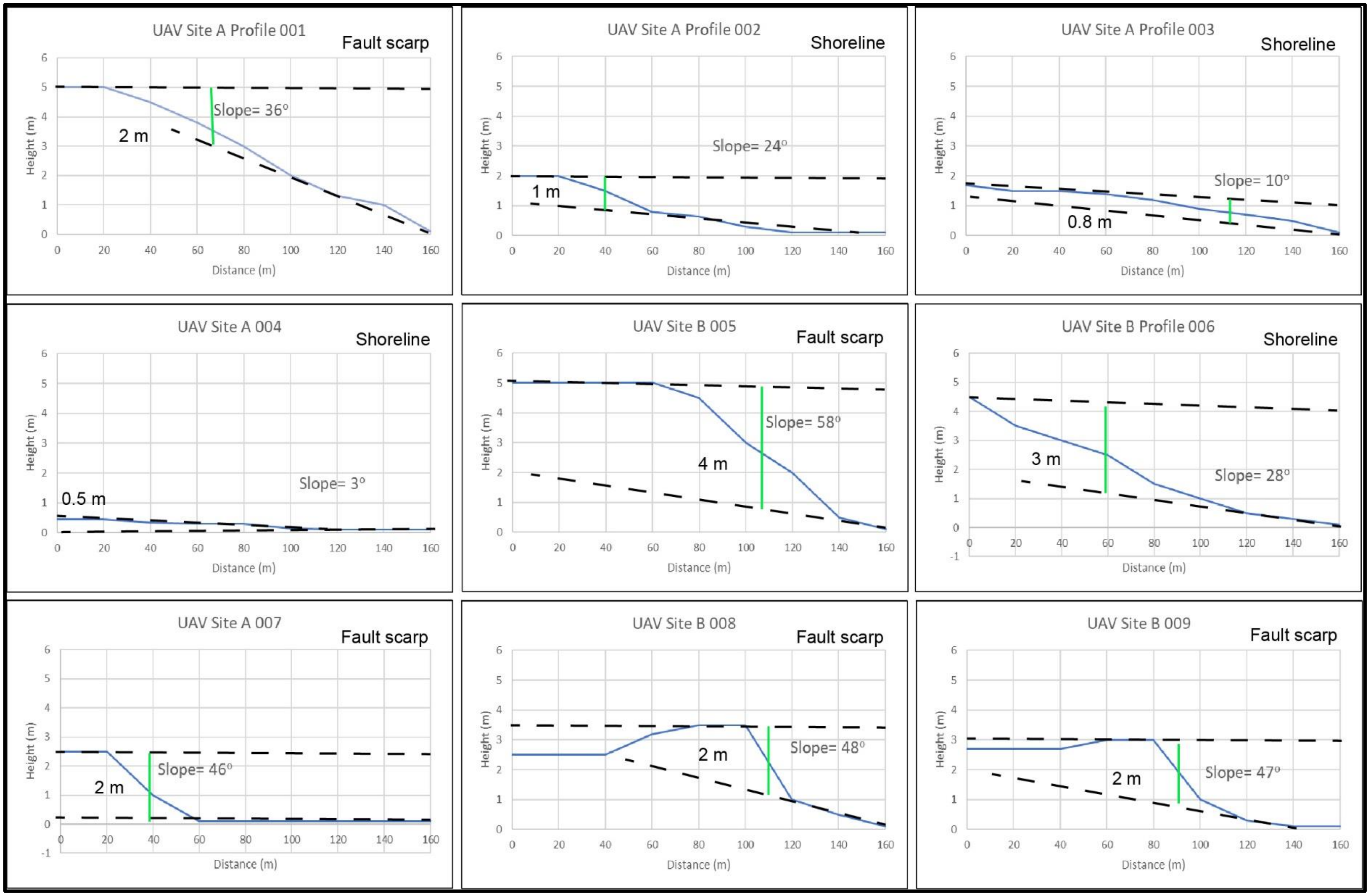

Figure 10. Scarp profiles from UAV Sites A and B. Black dashed lines show projections of slopes used to estimate scarp heights. Green line shows location of scarp height measurement taken.

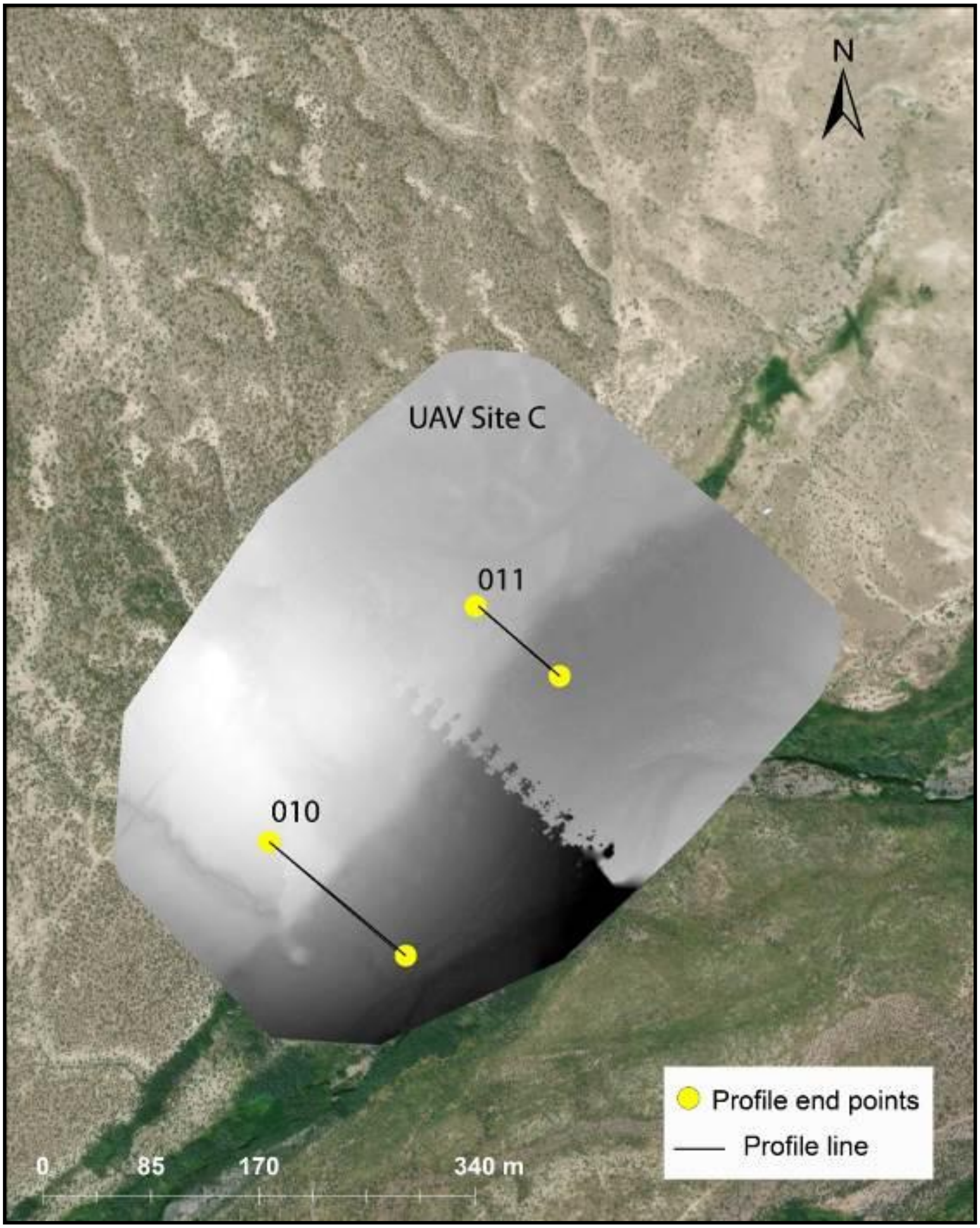

Figure 11. UAV DTM for flight mission Sites C with scarp profile lines.

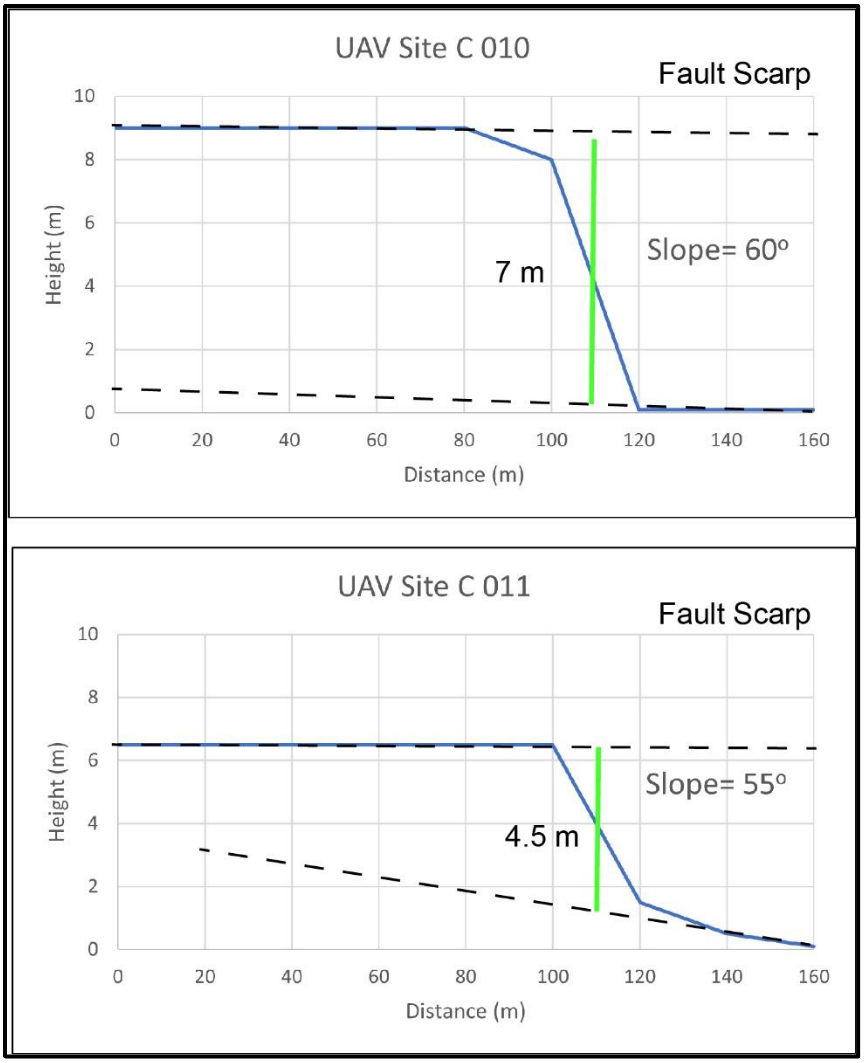

Figure 12. Scarp profiles from UAV Site C. Black dashed lines show projections of slopes used to estimate scarp heights. Green line shows location of scarp height measurement taken.

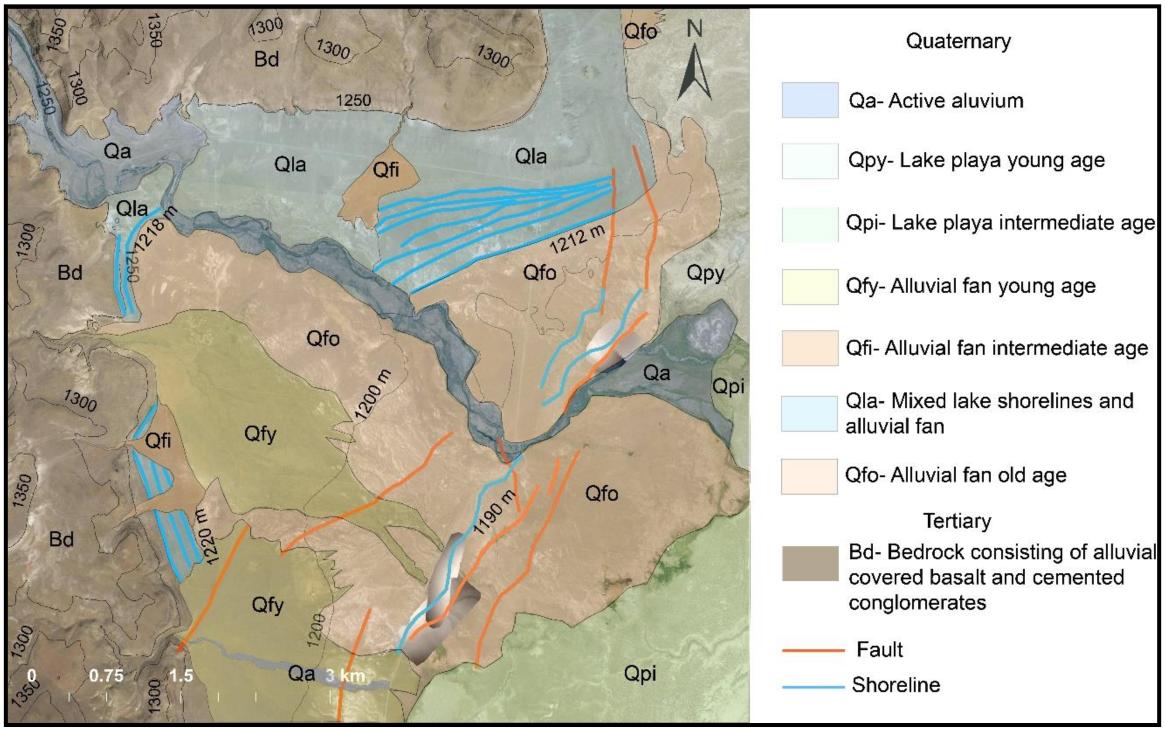

Figure 13. Quaternary map including shorelines (with key elevations labeled) and faults in the Sheepshead Spring region of Smoke Creek Desert. Black lines are 50 m contours.

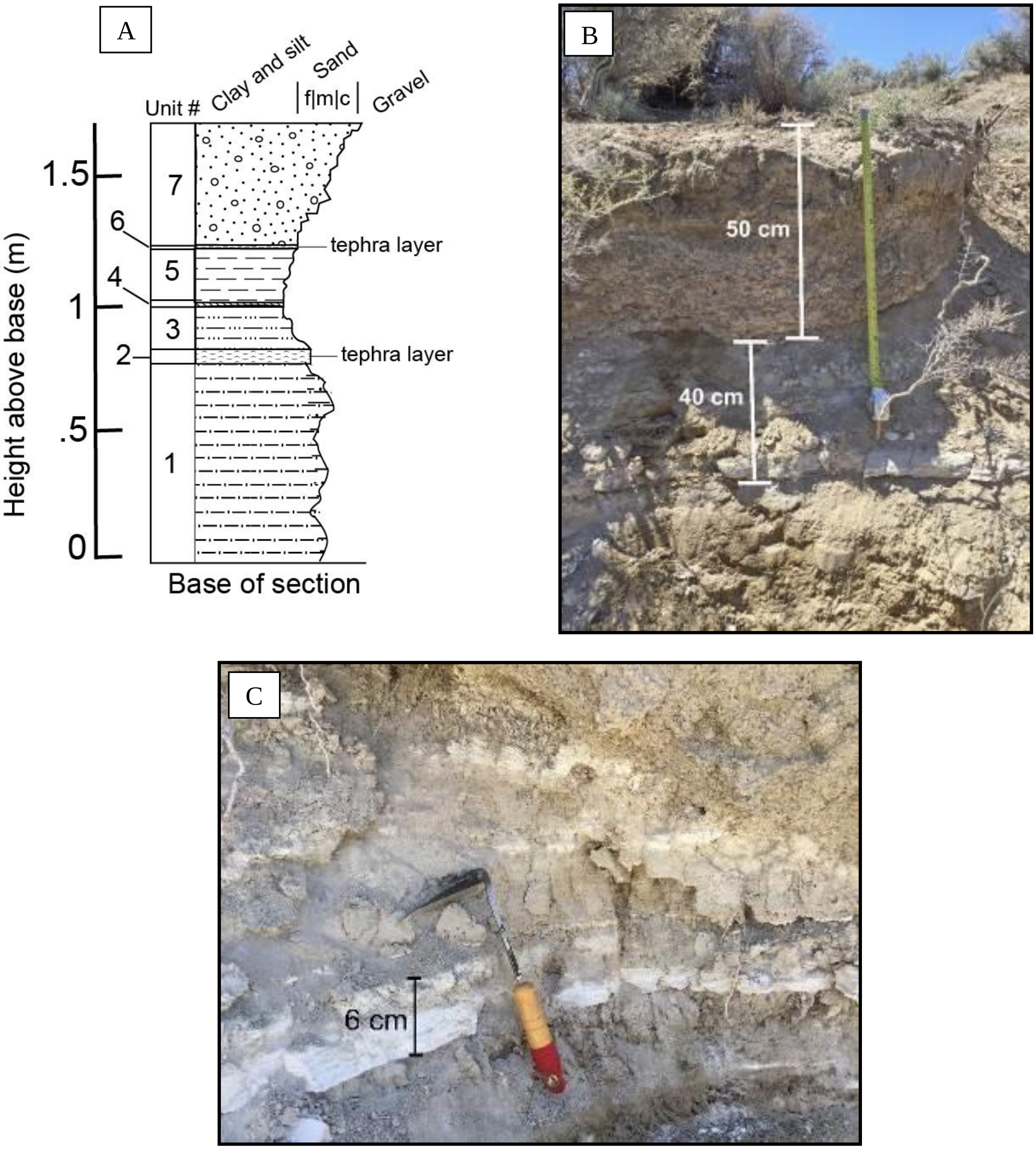

Figure 14. Tephra layers found in Smoke Creek near the 1190 m scarp. A) Stratigraphic column of the outcrop found in Smoke Creek. B) Photo of creek stratigraphy showing the 40 cm bed that includes the Trego Hot Springs ash. C) Detailed photo of Trego Hot Springs ash layer. Coordinates of photo 40.497284°N, 119.822445°W.

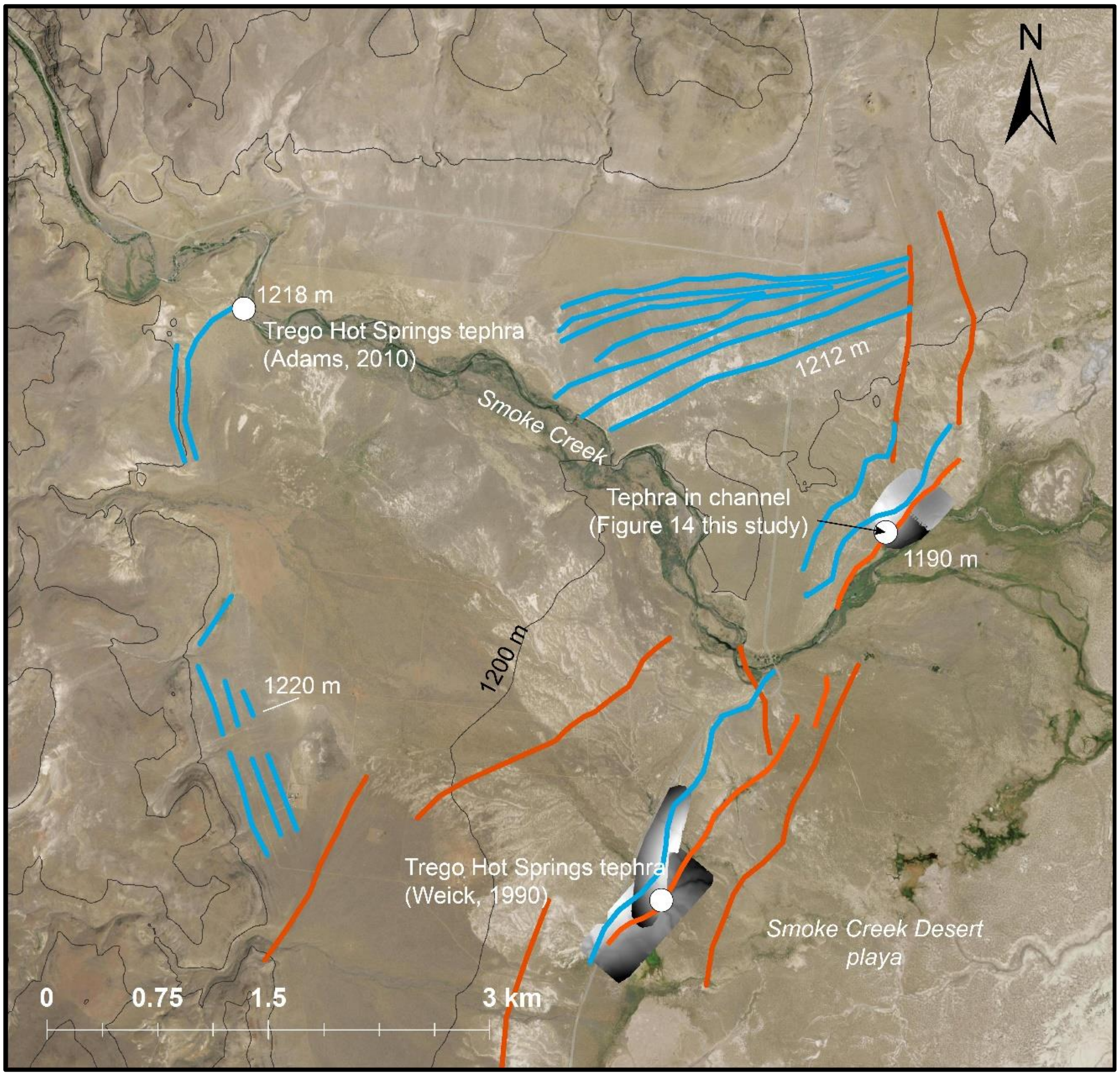

Figure 15. Map of tephra localities along smoke Creek. White circles mark tephra sites. Red lines mark fault scarps. Blue lines mark shorelines.

Chapter 3

The application of Uncrewed Aerial Systems (UAS) in post-earthquake ground deformation surveys: Examples from the M6.4 Monte Cristo, Nevada and M6.0 Antelope Valley, California earthquakes

Conni De Masi[1] and Richard D. Koehler[1]

[5]University of Nevada, Reno, Nevada Bureau of Mines and Geology, Reno, NV; U.S.A.

Abstract

One of the primary objectives of rapid field reconnaissance after an earthquake is to document perishable data through the production of georeferenced data and damage maps of the affected area, useful for hazard assessment. Identification of the disaster area and the estimated extent of surface damage is important for determining infrastructure stability and humanitarian relief. Satellite images and Interferometric Synthetic Aperture Radar (InSAR) are useful tools for analyzing the impacts of an earthquake, however they are not always available immediately after the event. For that reason, rapid reconnaissance surveys are typically initiated after every major event. New technology and methods in Uncrewed Aircraft Systems (UAS) have become valuable tools in capturing and assessing the extents and amount of damage after an earthquake.

Data acquisition at specified scales was successfully performed at select locations along the 2020 Mw6.5 Monte Cristo Range, Nevada and the 2021 Mw6.0 Antelope Valley, California earthquakes with small Uncrewed Aerial Vehicles (UAV). For UAV image analyses, a photogrammetric workflow was applied to construct models using the high-resolution images acquired with and without ground control points. The UAS plays an important role in the work of investigating and gathering information about the

primary and secondary effects of the earthquake related to surface rupture and shaking, as well as the location and extent of damage to roads and infrastructure radiating from the epicenter outward on the km scale.

1. Introduction

The natural effects and surface deformation related to earthquakes including ruptures, fissures, lateral spreading, and subsidence can provide key surface data for understanding earthquake processes; however, erosion and deposition (e.g. processes related to wind, rain, etc.) can quickly alter or erase any evidence of these features necessitating rapid documentation. Rapid response teams composed of geoscientists and engineers use Uncrewed Aerial Vehicles to work swiftly and efficiently in order to document any surface deformation and/or damage as a result of the event, preventing data loss. Using UAVs in post-earthquake reconnaissance events are valuable for documenting pertinent visual data quickly to communicate where repairs need to be made to roads and where to block off safety zones.

Uncrewed Aircraft Systems (UAS), also known as Uncrewed Aerial Vehicles (UAVs) or drones and their accompanying software, have been increasingly used over the last decade to investigate the effects of natural disasters including floods, hurricanes, earthquakes, and other events (Greenwood et al., 2020; Ybañez et al., 2021). In post-earthquake reconnaissance studies, UAS technology has been used to provide high resolution images for mapping primary surface fault rupture, secondary effects, such as liquefaction and landslides, as well as damage assessment (Tatham, 2009; Giardino et al., 2012; Meyer et al., 2015; Lei et al., 2018, Franke et al., 2019; Dee et al., 2020; Pierce et al., 2020; Koehler et al., 2021; Kozacı et al., 2021). Satellite images may not be readily available in the hours/days/weeks following the event when assessment of the natural effects and damage is most crucial. The documentation of perishable data in a post-earthquake scenario makes the quick deployment of UAVs essential in assessing the effects of the disaster (Gomez & Purdie, 2016). Drone image acquisition provides the opportunity to gather ground surface deformation data in the form of imagery for stills and Structure for Motion models and allows collecting observations over large distances in a short time frame. Drone flight mission planning, acquisition, data validation and image consolidation can be done entirely in the field ensuring adaptability to the ever-changing situation on the ground post-earthquake.

In this study, quadcopter UAVs were deployed to assess ground surface deformation following the 15 May 2020 Mw6.5 Monte Cristo Range, Nevada and the 8 July 2021 Mw6.0 Antelope Valley, California earthquakes as part of the Nevada Bureau of Mines and Geology earthquake rapid response team (Figures 1 and 2). Flight surveys were successful in imaging surface damage across the highway and landscape for the Monte Cristo Range earthquake. Digital terrane and orthomosaic models were made and from them we were able to collect data measurements on fracture direction and vertical slip. The drone images are a way to preserve evidence for reactivated movement along the “old landslide” in the town of Walker for the Antelope Valley earthquake and will be beneficial for comparison studies of movement of this feature in the future.

2. **Regional Tectonic Setting and Recent Earthquakes**

2.1. Central Walker Lane and The Mina Deflection

The central Walker Lane, specifically the Mina Deflection, is the location for the epicenter of the Monte Cristo Range earthquake (Figures 1 and 2). The central Walker

Lane is part of the larger transtentional Walker Lane Belt (Stewart, 1988) that extends along the eastern side of the Sierra Nevada and western margin of the Basin and Range which accommodates ∼20%–25% of relative dextral shear between the North American and Pacific Plate plates (Bennett et al., 1999; Dixon et al., 2000; Hammond and Thatcher, 2007). The central Walker Lane geodetic measurements indicate that ∼8 mm/yr of northwest directed dextral shear is accommodated in this region (Hammond & Thatcher, 2007; Hammond et al., 2011; Bormann et al., 2016). According to paleomagnetic observations, vertical-axis rotations of tectonic blocks in the west-central Walker Lane show that the west-central Walker Lane is organized into discrete blocks with heterogeneous regional distribution of clockwise vertical-axis rotation, ranging from ~10° to 60° around the Mina Deflection (Carlson et al., 2013). Similar studies were previously conducted to look at dextral shear in the northern Walker Lane (Cashman and Fontaine, 2000) to understand the kinematics and timing of intracontinental strain in the Walker Lane between northwestern Nevada and northeastern California. Northeast of the Mina Deflection, right-lateral shear is accommodated along the Benton Springs fault, Gumdrop Hills fault, and the Petrified Springs fault, a series of northwest-striking faults that extend along both the east and west sides of the Gabbs Valley Range (Figure 2) (Wesnousky, 2005; Angster et al., 2019). South of the Mina deflection, right-lateral shear is accommodated along a series of northwest-striking faults distributed between the Sierra Nevada and the White Mountains, with the White Mountain fault terminating at a fault junction with the Candelaria fault.

The Mina Deflection is characterized by a series of east–west- to northeast-striking left-lateral faults including the Candelaria, Columbus Salt Marsh, Rattlesnake, Excelsoir Mountains, Coaldale, Huntoon Valley, and Anchorite Hills faults (Figure 2) (Stewart, 1988; Wesnousky, 2005; Faulds and Henry, 2008). Tectonic geomorphic evidence for latest Pleistocene and Holocene sinistral displacement along the Mina Deflection faults includes uphill and alternately facing scarps, linear depressions, and deflected drainages. However, basin-facing scarps across alluvial fan and piedmont surfaces indicate a component of extension along the faults where they bend to strike north–northeast along range fronts (Wesnousky, 2005).

2.2. Faults near Antelope Valley, California

The Antelope Valley earthquake epicenter was located in a southwestern sub-basin of Antelope Valley which crosses the California and Nevada state boundary line south of Topaz Lake (Figures 1 and 2). Antelope Valley is a north-northwest oriented basin located between the east central Sierra Nevada and the central Walker Lane, north of the Mina Deflection, which was the location for the Monte Cristo Range earthquake. An approximately 23-km-long active fault trace (Antelope Valley fault) that dips east between 50^{o}-80^{o} bounds the western side of the valley and offsets young Quaternary deposits (Sarmiento et al., 2011; Sawyer et al., 2012; Pierce et al., 2020). Vertical displacement along the Antelope Valley fault (Figure 2) has produced a ~800 m steep range front with triangular facets and has preserved scarps in young alluvial fans. North of the junction of U.S. Highway 395 and California State Route 89, the surface expression of the fault is disturbed by the highway and locally submerged by Topaz Lake. The abrupt and over steepened range front west of Holbrook Junction suggests that the fault system may discontinuously extend to the northwest another ∼7 km, yielding a total length of 30 km or more (Sarmiento et al., 2011). The epicenter of the Antelope Valley earthquake occurred at the southern end of the Slinkard Valley fault near Little Antelope Valley, southwest of the “main” Antelope Valley. The Slinkard Valley fault (Figure 2) is a ~25 km long north-northwest-striking east-dipping normal fault located on the western edge of Slinkard Valley and parallels Antelope Valley to the west (Bryant, 2017). The north end of the Slinkard Valley fault is covered by a large landslide. Slickensides on the surfaces of joints exposed in a gully just south of Slinkard Creek in Antelope Valley are horizontal, indicating a component of strike-slip motion along the fault. The Slinkard Valley range front is associated with steep relief that decreases from north to south, from about 750 m near Highway 89 to less than 100 m near Little Antelope Pack Station (Bryant, 1983; Hayes, 1985).

2.3. Monte Cristo Range Earthquake

The 15 May 2020 Mw6.5 Monte Cristo earthquake was the largest earthquake in Nevada in over 65 years and occurred in a rural area of western Nevada about ~56 km west of the town of Tonopah (Dee et al., 2021; Koehler et al., 2021). The epicenter, located at 38.1626°N, 117.8695°W, was in the Mina Deflection section of the central Walker Lane. Aftershocks occurred across a ~30 km long, east-west oriented zone along the eastward projection of the Candelaria fault (Bormann et al., 2021; Ruhl et al., 2021). Surface ruptures from the Monte Cristo Range earthquake involved simultaneous rupture and slip in left-lateral-oblique and right-lateral-oblique components across a network of faults that form a kinematic link between orthogonal regional faults (Dee et al., 2021; Elliot et al., 2021; Koehler et al., 2021). Coseismic surface faulting was distributed across a width of 2.5–5 km perpendicular to the east–west trend delineated by seismicity and geodetic surface displacements (Ruhl et al., 2021; Hammond et al., 2021; Koehler et al., 2021). The mainshock occurred near the middle of the aftershock zone at the intersection of two distinct zones of seismicity (Ruhl et al., 2021).

The Monte Cristo Range earthquake was broken into two domains, the western and eastern domains (Koehler et al., 2021). In the western domain, numerous shallow, north-northeast-striking faults form a broad flower-structure-like fault mesh that coalesces at depth into a near-vertical, left-lateral fault (Ruhl et al., 2021). The maximum observed left-lateral displacements in the western domain are 20 cm along the northern main traces and 10 cm along the southern main traces, suggesting the total maximum left-lateral displacement was as much as 30 cm (Dee et al, 2021; Koehler et al., 2021). Vertical displacements in the western domain were predominantly down to the northwest typically several centimeters (~2 cm to 6 cm).

In the eastern domain, normal and right oblique slips on north-striking faults occurred along strike of the Benton Springs, Petrified Springs, and Eastern Columbus Salt Marsh faults, as well as older mapped bedrock normal faults (Koehler et al., 2021). Right-lateral displacements range between 3 cm to 5 cm, and vertical displacements range from 2 cm to 5.5 cm (Dee et al., 2021; Koehler et al., 2021). Seismicity east of the mainshock hypocenter occurs in a narrow, near-vertical, east-northeast-striking fault zone (Ruhl et al., 2021).

2.4.Antelope Valley Earthquake

The 8 July 2021, M6.0 Antelope Valley earthquake occurred about 32 km southwest of Smith Valley, NV (USGS, 2021). The epicenter was located at 38.5081^{o}N, 119.5020^{o}W, near the California-Nevada border and within the tectonic margin of the Sierra Nevada and Walker Lane shear zone. The earthquake was the result of normal faulting at approximately 7.5 km depth close the Slinkard Valley and Antelope Valley faults, which extend north-south along the Sierra Nevada range front.

Perceived shaking for the event was widely felt throughout western Nevada. According to the USGS event data webpage (USGS, 2021), shaking was moderate to strong with an intensity near the epicenter of MMV-MMVI. Shaking was felt 120 km north near the Reno-Carson City, Nevada region. There, shaking was light with an intensity of MMIV.

3. Methods

Two drones were used in the flight missions for rapid response field reconnaissance following the earthquake events. A DJI Phantom 4 PRO (FC6310) and a DJI Mavic Pro (FC220) were used in data acquisition for the Monte Cristo Range earthquake, and a DJI Mavic Pro (FC220) was used in data acquisition for the Antelope Valley earthquake. The DJI Phantom 4 PRO has a 20 megapixel camera with 1” (25.4 mm) sensor, a field of view of 84.88^o, and a varying aperture of f2.8-f11 with auto focus at 1 m to ∞. Average flight time is about 28 minutes for a fully charged battery with a battery drop of 1-2% per 30 seconds of active flying. Temperature changes also affect battery life so flying in higher altitudes with cooler atmospheric temperatures can decrease battery life about ~10% per 30 seconds. The DJI Mavic Pro has a 12.35 megapixel camera with 1/2.3” (11.04 mm**)** sensor, a field of view of 78.8^o, and a fixed aperture of f2.2. Distortion for this model is less than 1.5% and auto focus is from 0.5 m to ∞. Average flight time is about 21 minutes for a fully charged battery with similar atmospheric temperatures affecting battery life with that of the Phantom.

An EOS Arrow Gold RTK GNSS receiver was used through Bluetooth® connected to the drones for horizontal and vertical coordinate accuracy. GNSS signals supported by the Arrow Gold are GPS: L1CA, L1P, L1C, L2P, L2C, L5; GLONASS: G1, G2, P1, P2; Galileo: E1BC, E5a, E5b; BeiDou: B1, B2, B3 (without L5); and QZSS: L1CA. L2C, L5, L1C. Battery life on a full charge for the unit is about 7.5 hours. Due to the remote location of field work in the earthquake areas a real-time kinematic network was not established and therefore the unit received Satellite-based Augmentation System (SBAS) corrections Differential GPS with ~15 cm horizontal accuracy and ~30 cm vertical accuracy.

The drone was navigated by two methods. The first method was with the UAV remote control navigation by pilot manually, and the second method was with programmable automatic navigation using the Pix4D Capture software. The drone controllers were attached to an iPad mini 4 and loaded with the DJI controller app, the EOS Gold app, and the Pix4D Capture app. The manual flight mode was used when obstacles where present in the flight path of the UAV such as trees and changes in topography. The UAV pilot avoided potential obstacles while manually activating the drone’s camera and to ensure that adequate overlap was attained for the orthomosaic and model processing. Programmable automatic navigation was generated by using the flight planning feature of Pix4D Capture, in which a specified target area for data acquisition was selected by drawing a fixed or orthogonal shape with the onboard map. The Pix4D Capture software automatically sets the amount of flight paths covering the entire area in consideration of the flight mission altitude, velocity, and image overlap percentage. Once a flight is started, the application forwards the plan to the UAV and the DJI controller app which carries out the flight mission automatically. The drones were flown at an altitude of 50 meters with a flying velocity of 7.4 m/sec and an image overlap of 60% when using programmable automatic navigation.

Images captured by the drone were uploaded from the drone to computer for quality control and model building (Figure 3). Pix4D Mapper was used to build orthomosaic, digital terrane models (DTMs), and subsequent slope and contour maps (Figure 4, 5, and 6). The DTMs were processed with the Pix4D Mapper inverse distance weighting and triangulation algorithms. Model processing included vegetation removal at 1.2 meters and taller. The UAV image coordinate system was WGS 84 (EGM 96 Geoid) and model output coordinate system was WGS 84 / UTM zone 11N (EGM 96 Geoid).

4. Results

4.1. 2020 Monte Cristo Range earthquake

The reconnaissance efforts began on the day of the earthquake. UAS data acquired for this study covered one of the westernmost surface ruptures which extended continuously for over 1.5 km (Figures 5, 7, and 8). Ruptures within this area strike N-NE, are distributed across a ~30–40 m wide zone and are characterized by sinuous overlapping fractures with 0.5–3 cm openings (Figure 8) and common down-to the-east and southeast vertical separations of 2–5 cm. Individual fractures are up to 20–45 m long and exhibit an overall left-stepping pattern (Figure 5). UAS data was also acquired for the area adjacent to US HWY 95 and within the Columbus Salt Marsh. Deformation in this area included radial fractures with a radius of about 20 meters across and around HWY 95, and circular liquefaction features within the Columbus Salt Marsh (Figures 9, 10 and 11). Radial cracks that formed on the east side of the road contain micrograbens with a range in vertical displacement of 4 cm to 14 cm (Figure 10).

The images produced for this study, were combined with data acquisitions from other parts of the rupture and used to compile a comprehensive map of the surface rupture (Koehler et al., 2021; Dee et al., 2021). Additionally, images produced in areas of settlement damage to the highway were used to guide subsequent liquefaction studies (GEER, 2021).

The results for the EOS Arrow Gold GNSS GPS coordinates in this study were collected with the EOS application on the iPad mini 4 using the DJI Phantom 4 Pro. Atmospheric conditions allowed for the GNSS receiver to have a horizontal accuracy of 0.20 m (20 cm) and vertical accuracy within 0.301 m (30 cm). 29 satellites were in view with 26 of those being used. The differential status was set at Differential GPS with a differential age of 3. The drone was flown using the automatic navigation software through Pix4D Capture with ground control points used to determine the flight mission perimeter (Table 1). The flight survey consisted of 26 flight paths and was completed in ~3.5 hours. 775 images were captured over a 705 m x 125 m area (Figure 4).

Two models were produced using the Pix 4D Mapper software. The Average Ground Sampling Distance was 0.73 cm. Point clouds and textured mesh models were built to produce the DTM and orthomosaic images (Figures 4 and 5). The software mean reprojection error was 0.115 for all models. A sharp type noise filter was used for surface smoothing of the DTM. The final image resolution for both the DTM and orthomosaic was 0.727 cm/pixel.

The UAV image resolution quality was detailed enough to identify ground surface deformation of 2 cm to 5 cm fractures from 50 m in altitude for the Mw6.5 Monte Cristo Range earthquake event (Figure 5) on the digital terrain model and the still imagery (Figure 7). However, fractures smaller than 2 cm were not picked up in the aerial imagery or models due to the limitations in pixel resolution. This became a factor with the slope model as the width or "gap" of the fractures were mostly less than 2 cm wide and the surface lacked enough vertical exaggeration at the fractures for the model to define differences in slope. In other words, there was no discernable change in slope across the model (Figure 6).

4.2. 2021 Antelope Valley earthquake

Post-earthquake field teams did not find evidence of primary surface ruptures along previously mapped traces of the Antelope Valley and Slinkard Valley faults. However, there was evidence for secondary shaking related effects such as moved/tossed boulders and rockfall near roads, as well as new fracturing at the ends of pre-existing cracks in the "old landslide" (termed coined by local residents). Boulders were dislodged along US Highway 395 and toppled on to the highway in the Walker River Canyon south of the town of Walker. A few boulders also moved down slope on the range front bounding the western margin of Antelope Valley. Most of the surface deformation documented by the team occurred to the northeast of Antelope Peak, at the mouth of Mill Creek canyon as it opens into Little Antelope Valley, in the form of small landslides and canyon wall sloughing (Figures 12 and 13) (images can also be viewed on https://nevada-earthquake-clearinghousenbmg.hub.arcgis.com/pages/antelope-valley-earthquake), and at the "old landslide" located at the Lost Cannon Creek tributary going into Mill Creek canyon as short new fractures propagating along the ends of pre-existing landslide scarps and older slumping (Figures 14, 15, and 16). There were no surface ruptures noted by the team across the large landslide that buries the trace of the Slinkard Valley fault to the north near Highway 89. Results from the drone imagery combined with field observations helped to determine which pre-existing fractures had reactivated during the earthquake and were useful in quantitatively measuring the crack openings (Figures 14B and 14C). Field measurements indicate that the new fracture propagations range between ~1.25 meters and 2 meters respectively within the "old landslide". Pre-existing fractures that went across a dirt road on the landslide showed recent movement along a head scarp and the road directly, in the form of fresh soil and ground disturbance including finer particles such as silt and fine sand, and lack of compacted surface near the fractures (Figures 15 and 16). These fractures had re-openings of less than 1 cm (Figure 16).

The data for the RTK unit and drone GPS coordinates were collected using the EOS Arrow Gold and DJI Mavic Pro Quadcopter. Ellipsoidal height at the location of the RTK receiver above the "old landslide" in Walker, CA resulted in a measurement of 1872 m (near truck in Fig.15A). The horizontal accuracy for the location was within a measurement of 0.156 m (15.6 cm) and vertical accuracy was within 0.293 m (29.3 cm). 29 satellites were in view with 18 of those being used. The differential status was set at Differential GPS with a differential age of 6. For this post-earthquake investigation, the drone was manually flown within the canyon and above the landslide obtaining an altitude between 20 and 30 meters.

5. Discussion

Viewing the drone images while in the field during the post-earthquake reconnaissance helped guide the investigation teams to locations captured by the UAV but not yet explored on the ground. The use of fractures as a proxy for surface deformation can lead to a larger surface displacement measurement from the UAV imagery relative to field measurements when conducting quantitative analyses with the models, especially when the fractures are smaller than or near the pixel resolution (Goulet et al., 2020). This is due to the interpretation of pixel colors subjected to blurring effects especially with thin or small objects such as a surface fracture.

High-resolution optical satellite imagery of 1 meter or less would complement the visual data acquired from drones for post-earthquake investigations by providing pre-event surface data. The correlation of satellite, drone, and field data is ideal for measuring the near-fault horizontal and vertical surface displacement fields in order in recognize significant differences with previous geodetic- and geologic-based measurements (Antoine et al., 2021). The downside to the use of satellite imagery in this case would be the lack of recently acquired visual data for the hazard location pre-event. Storms bring rain and wind which can erode the landscape erasing any prior evidence of events in between when satellite tours capture the landscape. The most recent imagery of the Mw 6.5 Monte Cristo Range and the Mw6.0 Antelope Valley earthquakes was taken in 2017. That created a 3 to 4 year absence in which the landscape has changed to when post-event imagery data was collected. While that does not seem like much time for a landscape to change, one flash flood within that time period could wipe out any prior evidence of surface deformation. This reiterates the need for UAS in the field for post-earthquake rapid response deployment. Furthermore, the application of UAS surveys in general fault research can provide valuable datasets of surface conditions prior to an earthquake from which to compare rapid response data acquisitions after the next earthquake.

Use of the UAV was helpful for documenting earthquake effects over longer distances and getting to places normally inaccessible by foot. Reviewing the images in the field provided observations of the liquefaction features that formed in the Columbus Salt Marsh west of Hwy 95 which were not accessible on foot, and to see the extent of damage across Hwy 95 (Figures 9 and 11). The DTM and orthomosaic models were made into base maps utilized for measuring fracture lengths in the field which were published in Koehler et al. (2021) and Dee et al. (2021).

The UAV surveys conducted immediately after the Mw6.0 Antelope Valley earthquake provided an aerial view of the unstable “old landslide” near Walker, CA and afforded an opportunity to look for evidence of surface deformation in the form of new fractures and scarps. Based on inspection of the drone images in the field it was determined which sections of the landslide needed further investigation on the ground. Several existing landslide fractures and slumps showed fresh ruptures at their ends, as well as some newly exposed and re-opening of fractures less than 1 cm across. However, it was unclear if those fresh cracks were directly associated with the earthquake event due to shaking or if they were associated with on-going movement of the landslide in general.

6. Conclusions

This chapter highlights the importance of Uncrewed Aerial Systems, in addition to other image-based data such as satellite imagery and rapidly processed InSAR, for post-earthquake rapid response reconnaissance work. The UAS allow for quick review of aerial imagery for pin-pointing critical investigation locations, such as the road damage to Highway 95, radial features in the marsh west of the highway and surface fractures east of the highway from the Monte Cristo Range earthquake, and the increase in cracks along landslide scarps in Walker, CA from the Antelope Valley earthquake. This allows for greater ground distance to be covered in a shorter amount of time, helping cut down on response costs and assists in directing ground crews. Offsite processing of UAV data allows for the creation of DTM and photo orthomosaic models that can be used for quantitative analyses within the pixel resolution.

The use of UASs were helpful in identifying areas near the event epicenters that experienced surface ruptures (Mw6.5 Monte Cristo Range earthquake) and those areas that did not (Mw6.0 Antelope Valley earthquake). The reliability on the DTM and orthomosaic models depends on pixel resolution. However, the UAV images set at the parameters defined in this study allowed for sufficient detail in the models to match the 2 cm or larger surface ruptures that were seen by field ground crews for the Monte Cristo Range event, and to view the recent activity along pre-existing fractures and scarps within the “old landslide” for the Antelope Valley event.

Acknowledgements

We thank Evan Hartshorn for assistance during UAV field work. Non-UAV data was collected using Avenza Maps and Field Move software versions available in 2020. Support for De Masi and Koehler was provided by the Nevada Bureau of Mines and Geology.

References

Angster, S. J., Wesnousky, S. G., Figueiredo, P. M., Owen, L. A., and Hammer, S.J., 2019, Late Quaternary slip rates for faults of the central Walker Lane (Nevada, USA): Spatiotemporal strain release in a strike-slip fault system, Geosphere 15, no. 5, 1460–1478.

Bennett, R. A., Davis, J. L. and Wernicke, B. P., 1999, Present-day pattern of Cordilleran deformation in the western United States, Geology 27, no. 4, 371–374.

Bormann, J., Hammond, W.C., Kreemer, C., and Blewitt, G., 2016, Accommodation of missing shear strain in the central Walker Lane, western North America—constraints from dense GPS measurements: Earth and Planetary Science Letters, v. 440, p. 169–177.

Bormann, J. M, Morton, E.A., Smith, K.D., Kent, G.M., Honjas, W.S., Plank, G.L., and Williams, M.C., 2021, Nevada Seismological Laboratory rapid seismic monitoring deployment and data availability for the 2020 M6.5 Monte Cristo Range, Nevada earthquake sequence: Seismological Research Letters, v. 92, p. 810-822.

Bryant, W.A., 1983, Faults in Antelope Valley, Slinkard Valley, and along the West Walker River, Mono County: California Division of Mines and Geology, Fault Evaluation Report FER-154, 14 p.

Bryant, W.A., compiler, 2017, Fault number 474, Slinkard Valley fault, in Quaternary fault and fold database of the United States: U.S. Geological Survey website, https://earthquakes.usgs.gov/hazards/qfaults, accessed 10/19/2021.

Carlson, C., Pluhar, C., Glen, J. and Farner, M., 2013, Kinematics of the west-central Walker Lane: Spatially and temporally variable rotations evident in the Late Miocene Stanislaus Group. Geosphere. 9. 10.13140/2.1.2394.9442.

Cashman, P.H., and Fontaine, S.A., 2000, Strain partitioning in the northern Walker Lane, western Nevada and northeastern California: Tectonophysics, v. 326, p. 111–130, doi: 10.1016 /S0040 -1951 (00)00149-9.

Dee, S., Koehler, R.D., Elliott, A.J., Hatem, A.E., Pickering, A.J., Pierce, I., Seitz, G.G., Collett, C.M., Dawson, T.E., De Masi, C., dePolo, C.M., Hartshorn, E.J., Madugo, C.M., Trexler, C.C., Verdugo, D.M., Wesnousky, S.G., and Zachariasen, J.., 2021, Surface Rupture Map of the 2020 M 6.5 Monte Cristo Range earthquake, Esmeralda and Mineral counties, Nevada: Nevada Bureau of Mines and Geology Map 190, 2 sheets, scale 1:14,000, 26p.

Dixon, T. H., Miller, H., Farina, F., Wang, H., and Johnson, D., 2000, Present-day motion of the Sierra Nevada block and some tectonic implications for the Basin and Range Province, North America Cordillera, Tectonics 19, no. 1, 1–24.

Faulds, J. E., and Henry, C.D., 2008, Tectonic influences on the spatial and temporal evolution of the Walker Lane: An incipient transform fault along the evolving Pacific–North American plate boundary, in Ores and Orogenesis: Circum-Pacific Tectonics, Geologic Evolution, and Ore Deposits, J. E. Spencer and S. R. Titley (Editors), Arizona Geological Society Digest 22, 437–470.

Franke, K.W., and Koehler, R.D., with contributing authors Atalay, F., Beyzaei, C.Z., Cabas, A., Christie, S., Dickenson, S., Hastings, N., Pierce, I., Stuedlein, A., Wang, X., Yang, Z., et al., 2019, Geotechnical Engineering Reconnaissance of the 30 November 2018 Mw 7.1 Anchorage, Alaska Earthquake, GEER Report GEER-059, v 2.1.

Giardino, M., Perotti, L., Lanfranco, M. and Perrone, G., 2012, GIS and geomatics for disaster management and emergency relief: a proactive response to natural hazards. Appl Geomat 4, 33–46. https://doi.org/10.1007/s12518-011-0071-z

Gomez, C., and Purdie, H., 2016, UAV-based photogrammetry and geocomputing for hazards and disaster risk monitoring—a review. Geoenviron Disasters 3(1):23

Goulet, C. A., Wang, Y., Nweke, C.C., Tang, B., Wang. P., Hudson, K.S., Ahdi, S.K., Meng, X., Hudson, M.B., and Donnellan, A., et al., 2021, Comparison of Near-Fault Displacement Interpretations from Field and Aerial Data for the M 6.5 and 7.1 Ridgecrest Earthquake Sequence Ruptures, Bull. Seismol. Soc. Am. 111, 2317–2333, doi: 10.1785/012020022

Greenwood, F., Nelson, E.L., and Greenough, P.G., 2020, Flying into the hurricane: a case study of UAV use in damage assessment during the 2017 hurricanes in Texas and Florida. PLoS ONE 15(2):e0227808

Hammond, W.C., and Thatcher, W., 2007, Crustal deformation across the Sierra Nevada, northern Walker Lane, Basin and Range transition, western United States measured with GPS, 2000–2004: Journal of Geophysical Research-Solid Earth, v. 112, B05411, 26 p.

Hammond, W. C., Blewitt, G., and Kreemer, C., 2011, Block modeling of crustal deformation of the northern Walker Lane and Basin and Range from GPS velocities, J. Geophys. Res. 116, doi:10.1029/2010JB007817.

Hammond, W. C., Blewitt, G., Kreemer, C., Koehler, R.D., and Dee, S., 2021, Geodetic observation of seismic cycles before, during, and after the 2020 Monte Cristo Range earthquake using the MAGNET GPS network, Seismol. Res. Lett., doi:10.1785/0220200338.

Koehler, R. D., Dee, S., Elliott, A., Hatem, A., Pickering, A., Pierce, I., and Seitz, G., 2021, Field Response and Surface-Rupture Characteristics of the 2020 M 6.5 Monte Cristo Range Earthquake, Central Walker Lane, Nevada, Seismol. Res. Lett. 92, 823–839, doi:10.1785/0220200371.

Kozacı, Ö., Madugo, C.M., Bachhuber, J.L., Hitchcock, C.S., Kottke, A.R., Higgins, K., Wade, A., and Rittenour, T., 2021, Rapid Postearthquake Field Reconnaissance, Paleoseismic Trenching, and GIS-Based Fault Slip Variability Measurements along the Mw 6.4 and Mw 7.1 Ridgecrest Earthquake Sequence, Southern California, Bull. Seismol. Soc. Am. 111, 2334–2357, doi:10.1785/0120200262

Tianjie Lei, Yazhen Zhang, Jingxuan Lu , Zhiguo Pang, Jun’e Fu, Guangyuan Kan, Wei Qu, and Yang Wang, 2018, The application of UAV remote sensing in mapping of damaged buildings after earthquakes, Proc. SPIE 10806, Tenth International Conference on Digital Image Processing (ICDIP 2018), 1080651 (9 August 2018); https://doi.org/10.1117/12.2503163

Meyer, D., Hess, M., Lo, E., Wittich, C.E., Hutchinson, T.C. and Kuester, F., 2015, UAV-based post disaster assessment of cultural heritage sites following the 2014 South Napa Earthquake, 2015 Digital Heritage, pp. 421-424, doi: 10.1109/DigitalHeritage.2015.7419539.

Pierce, I., Williams, A., Koehler, R.D., and Chupik, C,. 2020, High-Resolution Structure-From- Motion Models and Orthophotos of the Southern Sections of the 2019Mw 7.1 and 6.4 Ridgecrest Earthquakes Surface Ruptures, Seismol. Res. Lett. 91, 2124–2126, doi:10.1785/0220190289.

Pierce, I. K. D., Wesnousky, S. G., Owen, L. A., Bormann, J. M., Li, X., and Caffee, M., 2021, Accommodation of plate motion in an incipient strikeslip system: The Central Walker Lane. Tectonics, 40, e2019TC005612. https://doi.org/10.1029/2019TC005612.

Sarmiento, A. C., Wesnousky, S. G., & Bormann, J. M., 2011, Paleoseismic Trenches across the Sierra Nevada and Carson Range Fronts in Antelope Valley, California, and Reno, Nevada. Bulletin of the Seismological Society of America, 101, 2542–2549. https://doi.org/10.1785/0120100176.

Ruhl, C.J., Morton, E.A., Bormann, J.M., Hatch-Ibarra, R., Ichinose, G., and Smith, K., 2021, Complex fault geometry of the 2020 Mww6.5 Monte Cristo Range, Nevada earthquake sequence: Seismological Research Letters xx.

Sawyer, T.L., Adams, K., Bryant, W.A., and Haller, K.M., compilers, 2012, Fault number 1287, Antelope Valley fault zone, in Quaternary fault and fold database of the United States: U.S. Geological Survey website, https://earthquakes.usgs.gov/hazards/qfaults, accessed 09/23/2021 02:14 PM.

Stewart, J.H., 1988, Tectonics of the Walker Lane belt, western Great Basin Mesozoic and Cenozoic deformation in a zone of shear. In W. G. Ernst (Ed.), Metamophism and crustal evolution of the Western US (pp. 685–713). Englewood Cliffs, NJ: Prentice Hall.

Tatham, P., 2009, An investigation into the suitability of the use of unmanned aerial vehicle systems (UAVS) to support the initial needs assessment process in rapid onset humanitarian disasters. *International Journal of Risk Assessment and Management, 13,* 60-78.

Wesnousky, S.G., 2005, Active faulting in the Walker Lane, Tectonics 24, TC3009, doi: 10.1029/2004TC001645.

United States Geologic Survey, 2021, "M 6.0 - Antelope Valley, CA". earthquake.usgs.gov. Retrieved 23 September 2021.

Ybañez, R.L., Ybañez, A.A.B., Lagmay, A.M.F.A., and Aurelio, M.A., 2021, Imaging ground surface deformations in post-disaster settings via small UAVs. Geosci. Lett. 8, 23. https://doi.org/10.1186/s40562-021-00194-8

FIGURES

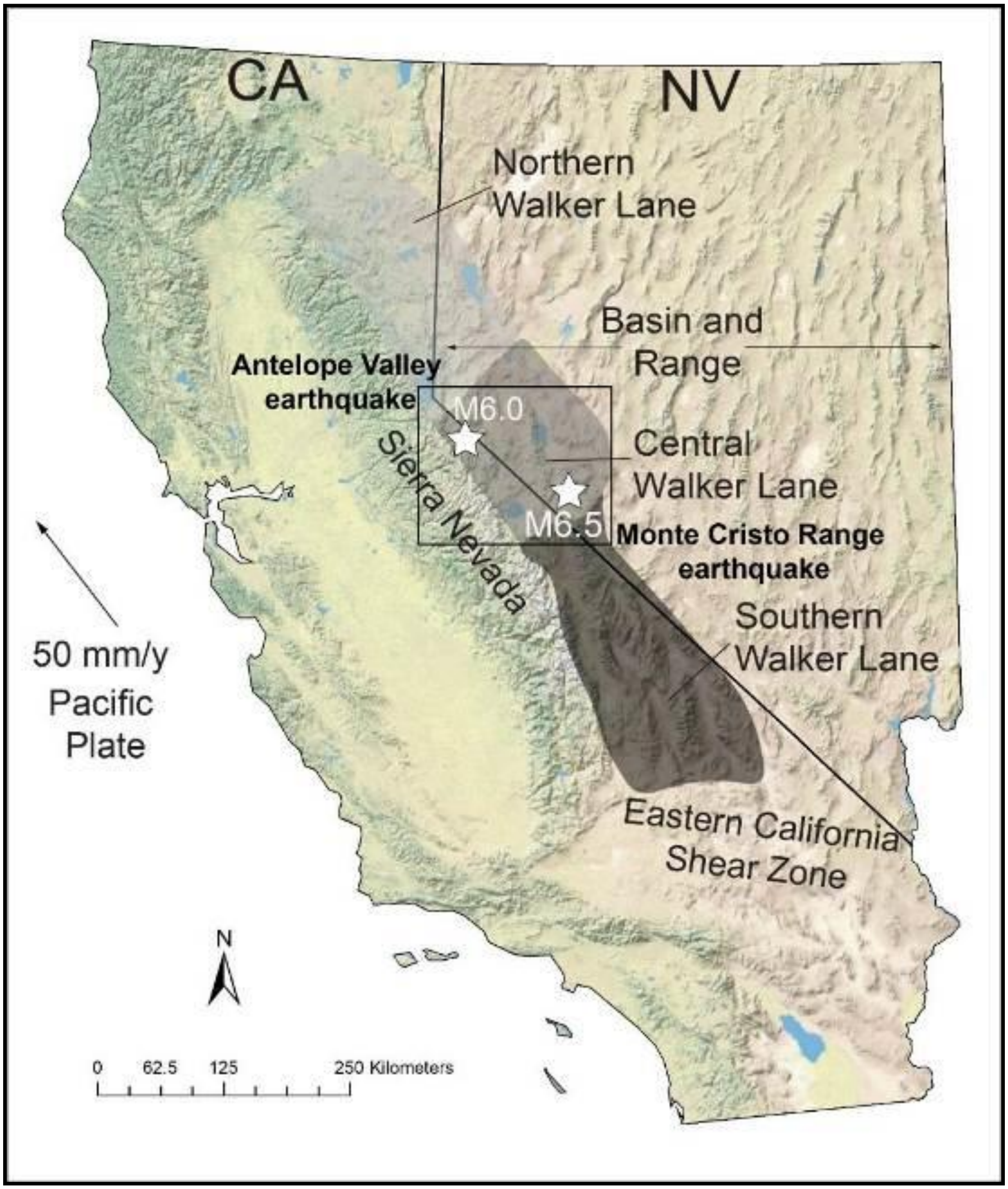

Figure 1. Regional map of the Walker Lane showing the locations of the M6.5 Monte Cristo Range and M6.0 Antelope Valley earthquakes (white stars). Outlined box represents the location of Figure 2. Shaded regions indicate the location of the southern Walker Lane (dark gray), central Walker Lane (gray), and northern Walker Lane (light gray).

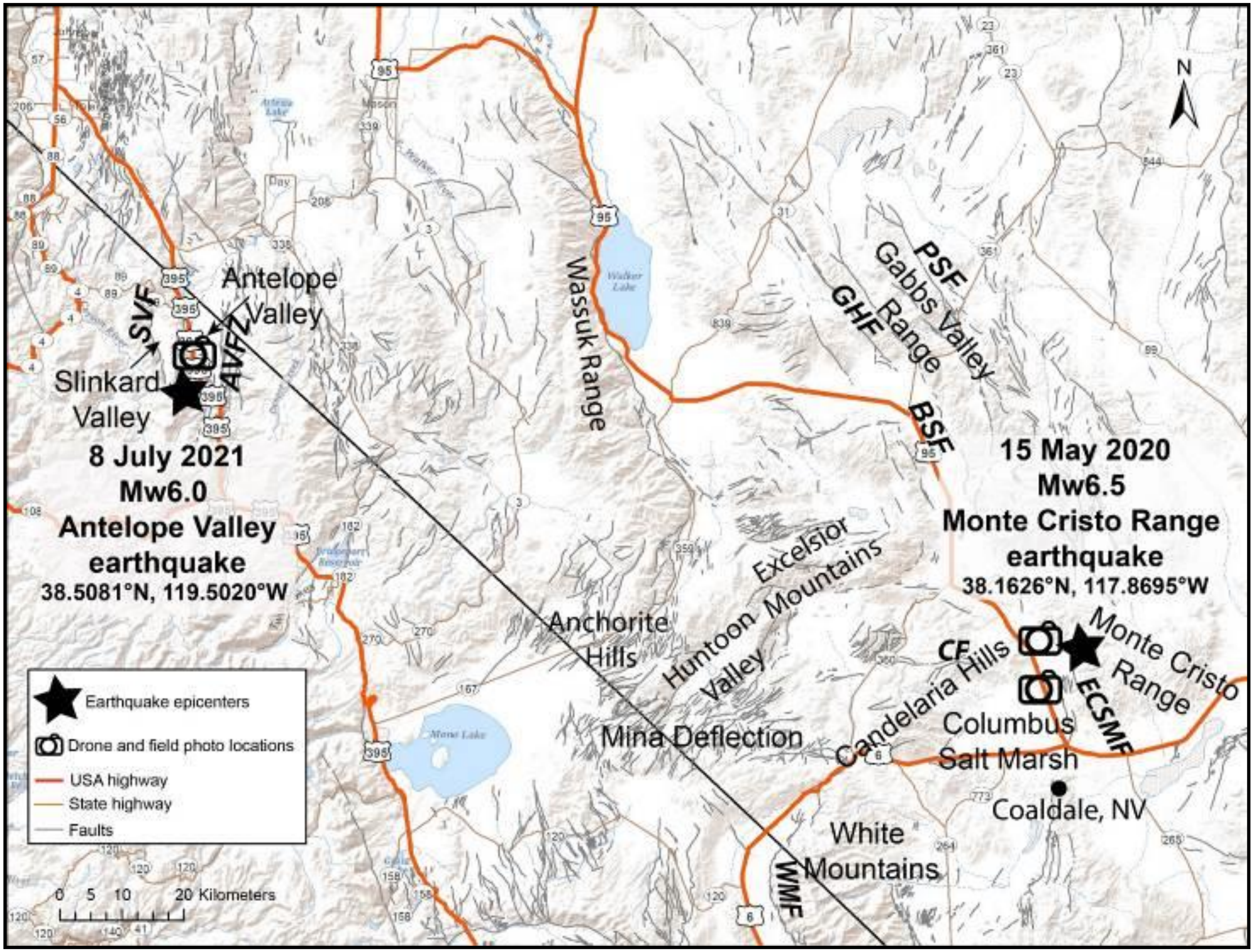
N
8 July 2021
Mw6.0
Antelope Valley
earthquake
38.5081°N, 119.5020°W
15 May 2020
Mw6.5
Monte Cristo Range
earthquake
38.1626°N, 117.8695°W
Antelope Valley
Slinkard Valley
SVF
AVFZ
Wassuk Range
PSF
Gabbs Valley Range
GHF
BSF
Excelsior Mountains
Anchorite Hills
Huntoon Valley
Mina Deflection
CF
Candelaria Hills
Monte Cristo Range
ECSMF
Columbus Salt Marsh
Coaldale, NV
White Mountains
WMF
Earthquake epicenters
Drone and field photo locations
USA highway
State highway
Faults
0 5 10 20 Kilometers

Figure 2. Shaded relief map of the Central Walker Lane 15 May 2020 Mw6.5 Monte Cristo Range and 8 July 2020 Mw6.0 Antelope Valley earthquake epicenter locations. Map includes major roads (orange lines) and faults (light gray lines). AVFZ: Antelope Valley Fault Zone; BSF: Benton springs fault; CF: Candelaria fault; ECSMF: Eastern Columbus Salt Marsh fault; GHF: Gumdrop Hills fault; PSF: Petrified springs fault; SVF: Slinkard Valley fault; WMF: White Mountain fault. (Source of faults: USGS Quaternary Faults and Fold Database).

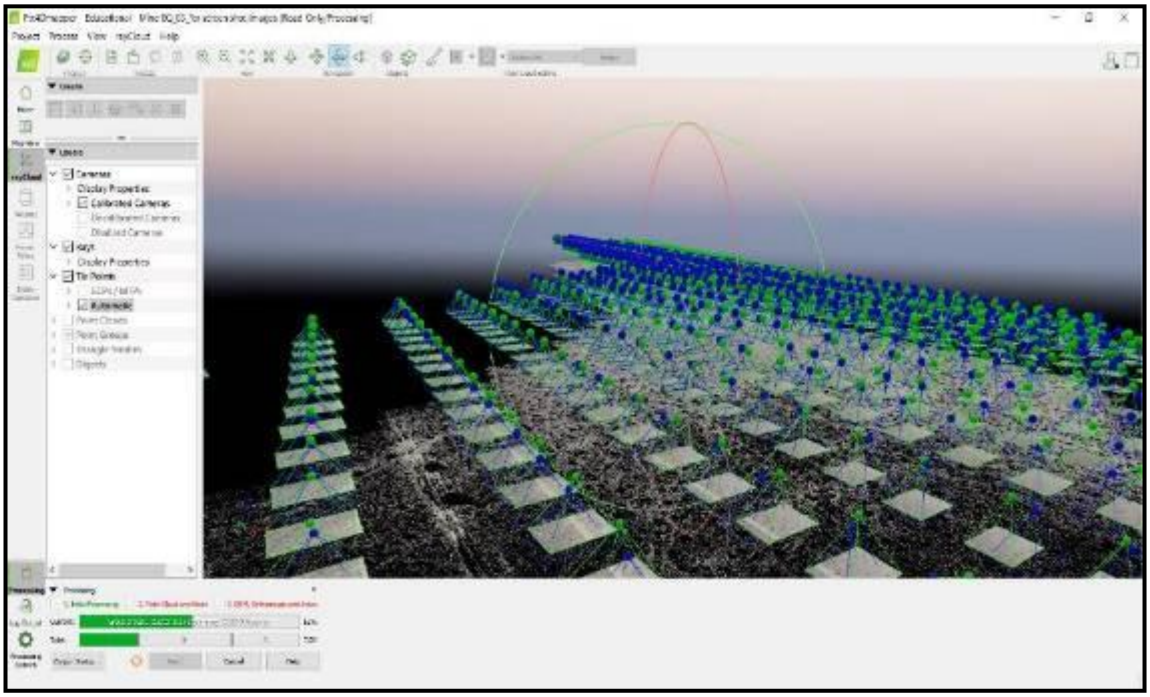

Figure 3. Image of the ray cloud in Pix4D Mapper. Drone photos are being matched to their geographical positions for building a georeferenced DTM and orthomosaic.

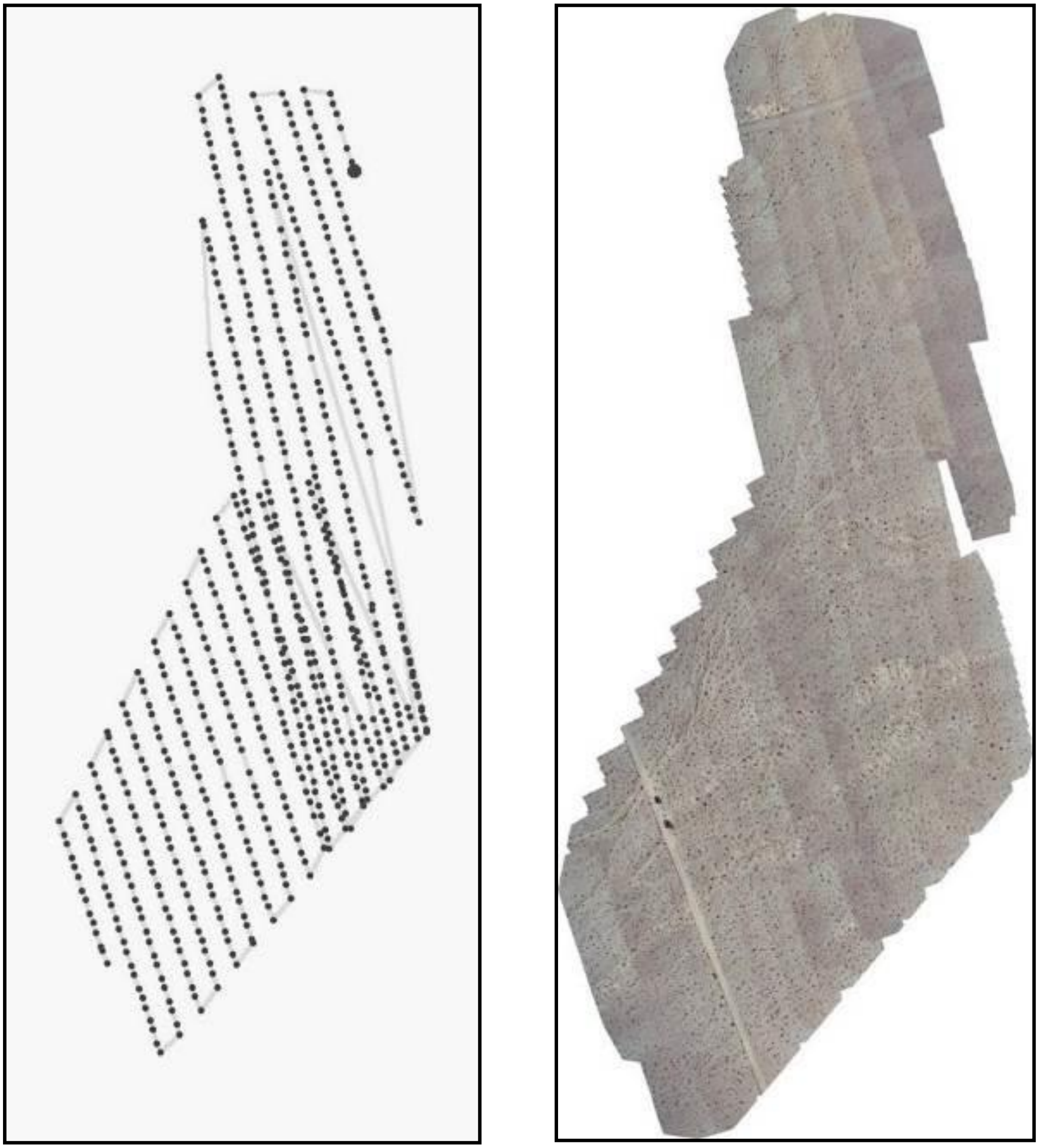

Figure 4. Pix4D Mapper models. A) UAV mission flight path lines and camera points. B) Photo orthomosaic model produced in Pix4D Mapper. Note two black specks on road are field vehicles.

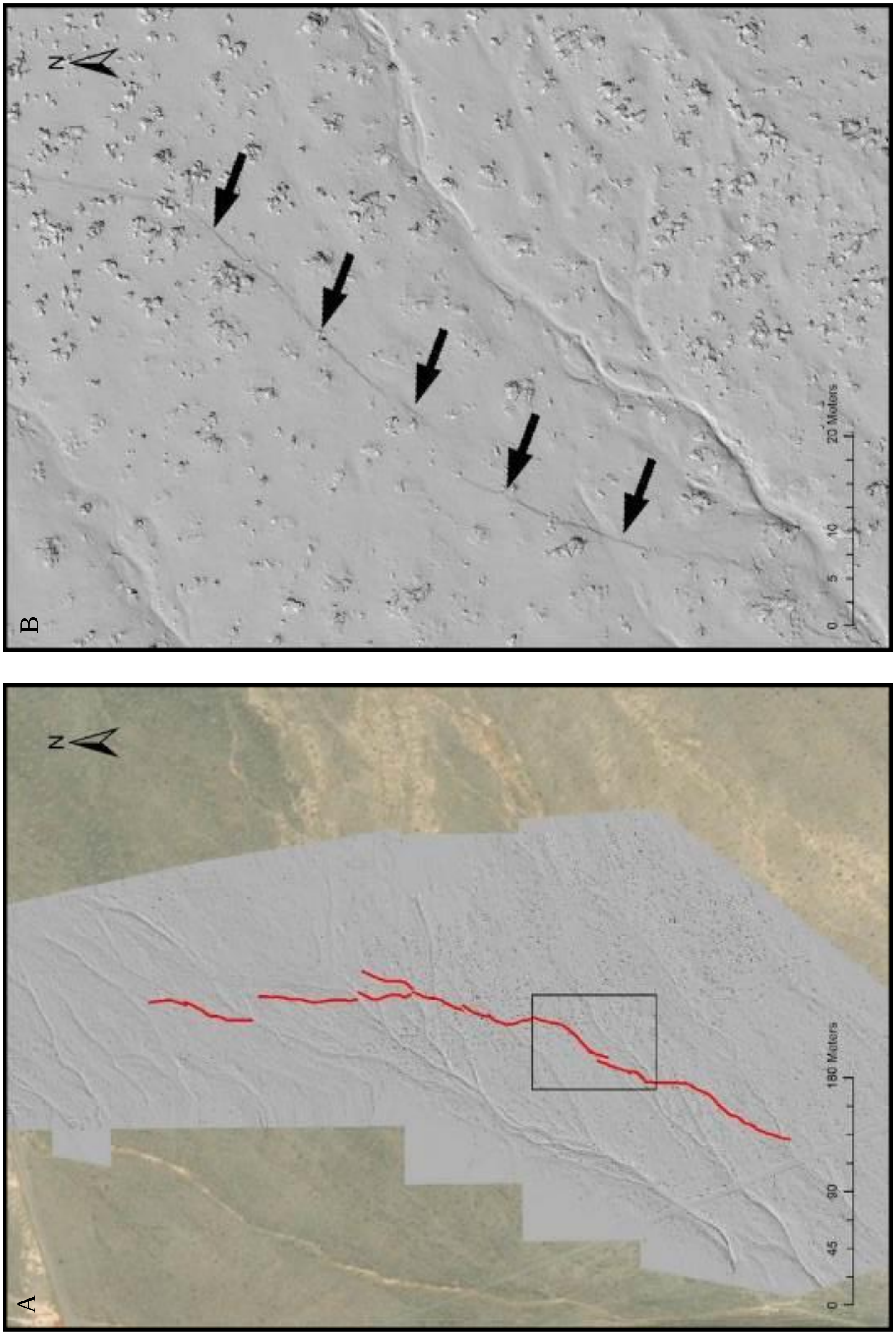
B
N
0
5
10
20 Meters
A
N
0
45
90
180 Meters

Figure 5. A) A Digital Terrane Model of surface deformation from the Monte Cristo Range earthquake located in the southern extent. Red line marks surface ruptures and the black box outlines Figure 3B. B) Arrows point to surface ruptures that have a vertical offset of 2 to 5 cm.

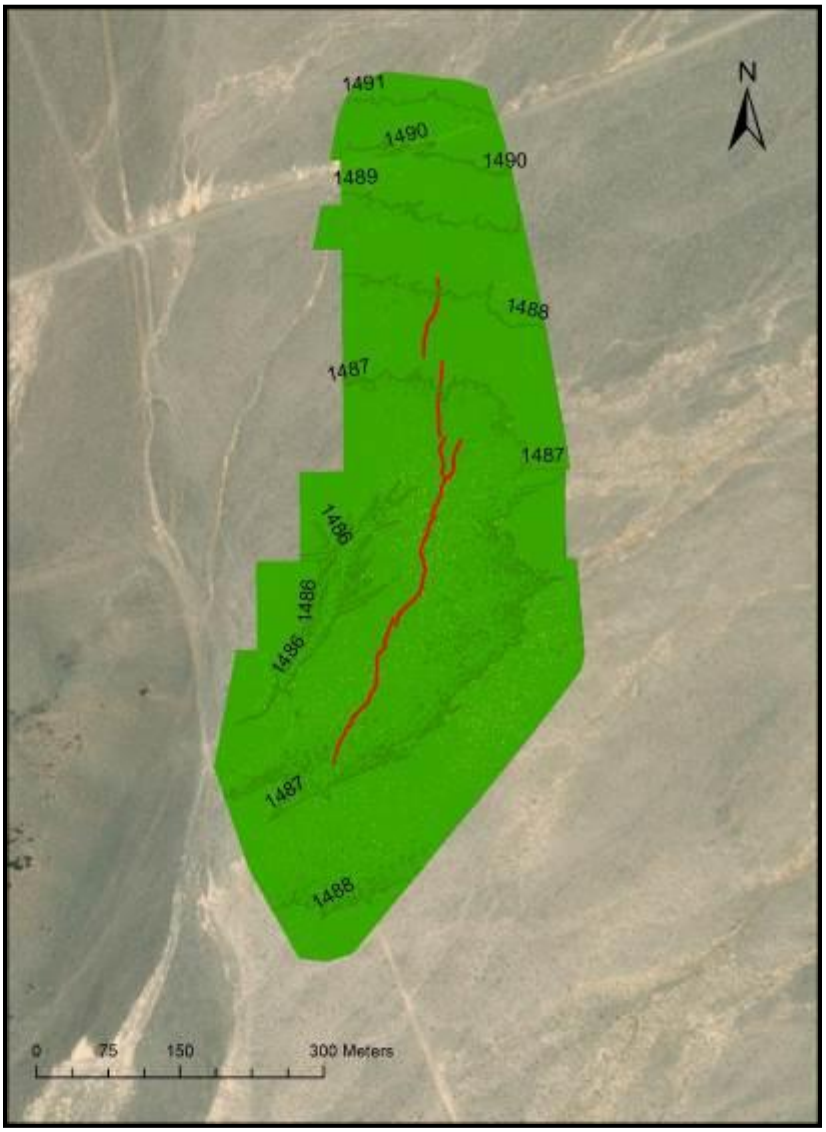

Figure 6. Slope and contour map derived from the drone DTM model produced with Pix4D Mapper. Green is the ground. Yellow specs mark the vegetation. Red lines are fractures.

Figure 7. Drone image of surface rupture produced during the Monte Cristo earthquake expressed as a left-stepping 45 m-long fracture. Black arrows point to fracture.
Drone height is ~20 m above ground. The northern end of the Monte Cristo Range is in the background.

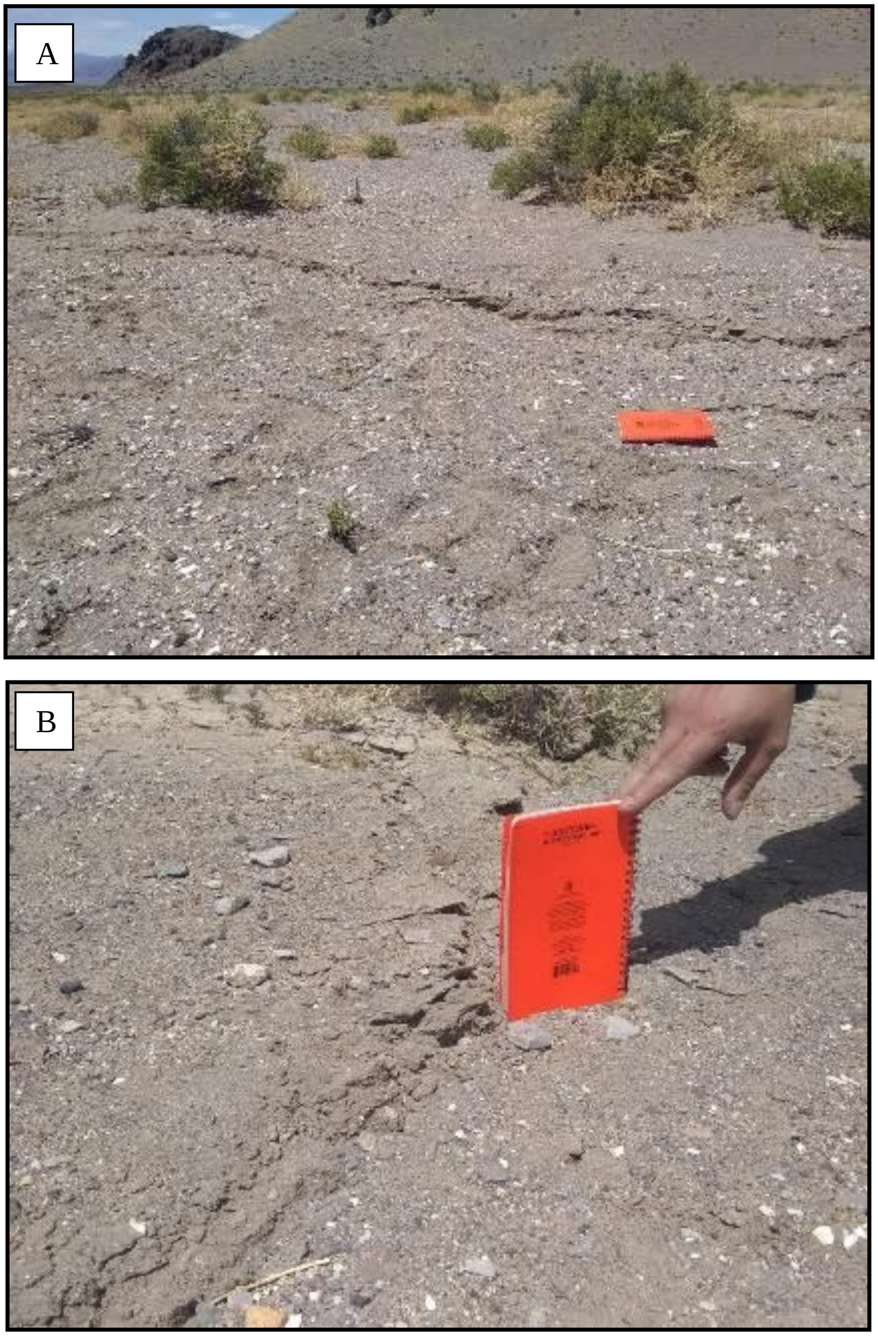

Figure 8. Field photos of fractures from the M6.5 Monte Cristo Range earthquake located on the western side of Highway 95. Coordinates of A and B 38.15114^{o}N, 117.93654^{o}W

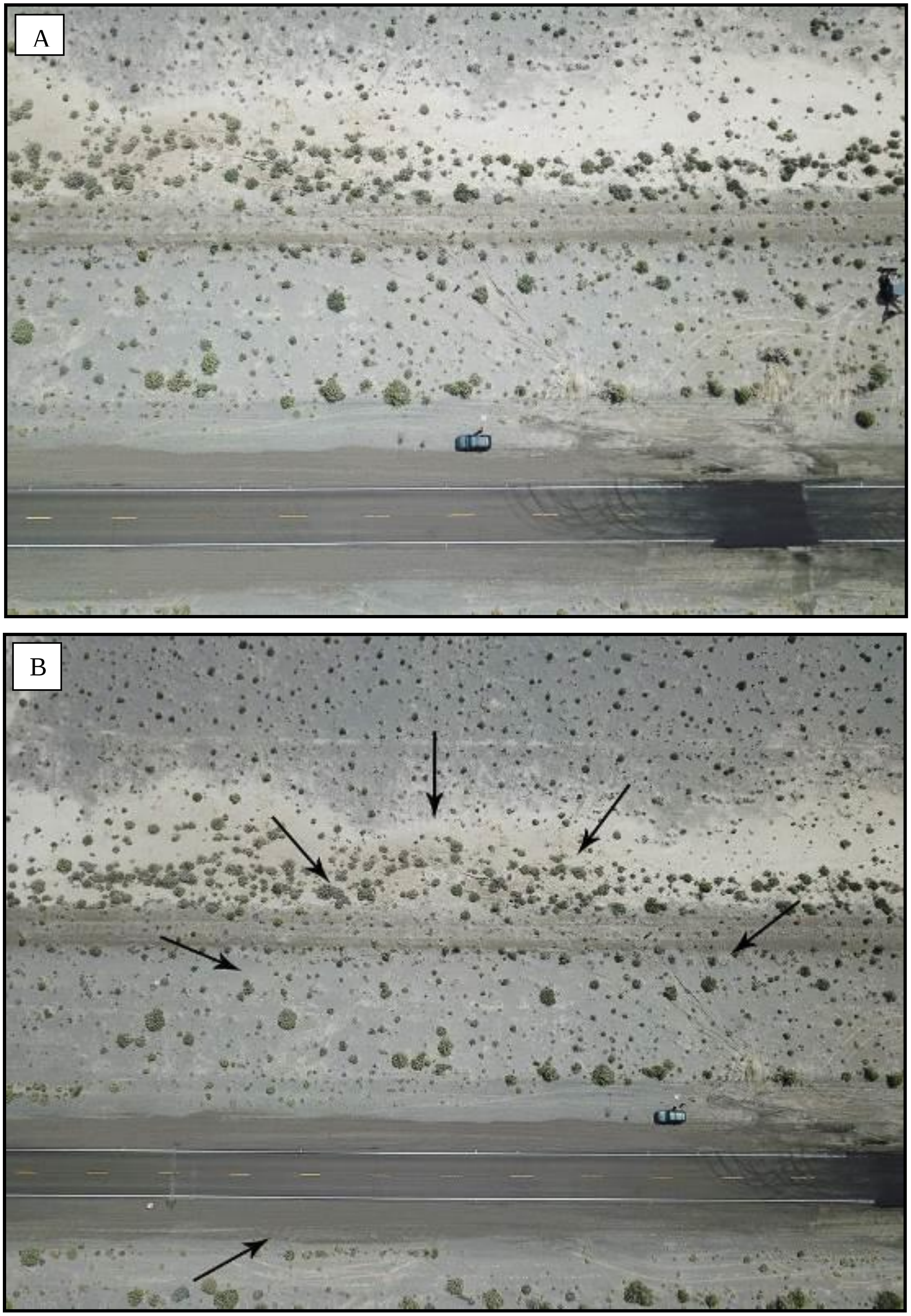
A
B

Figure 9. UAV aerial view of surface deformation found along Highway 95 at the eastern margin of the Columbus Salt Marsh. A) The lower right side of the image shows where NDOT repaired the road. B) shows black arrows pointing to radial cracks that formed on the east side of the road. Radial cracks range in vertical displacement of 4 cm to 14 cm.

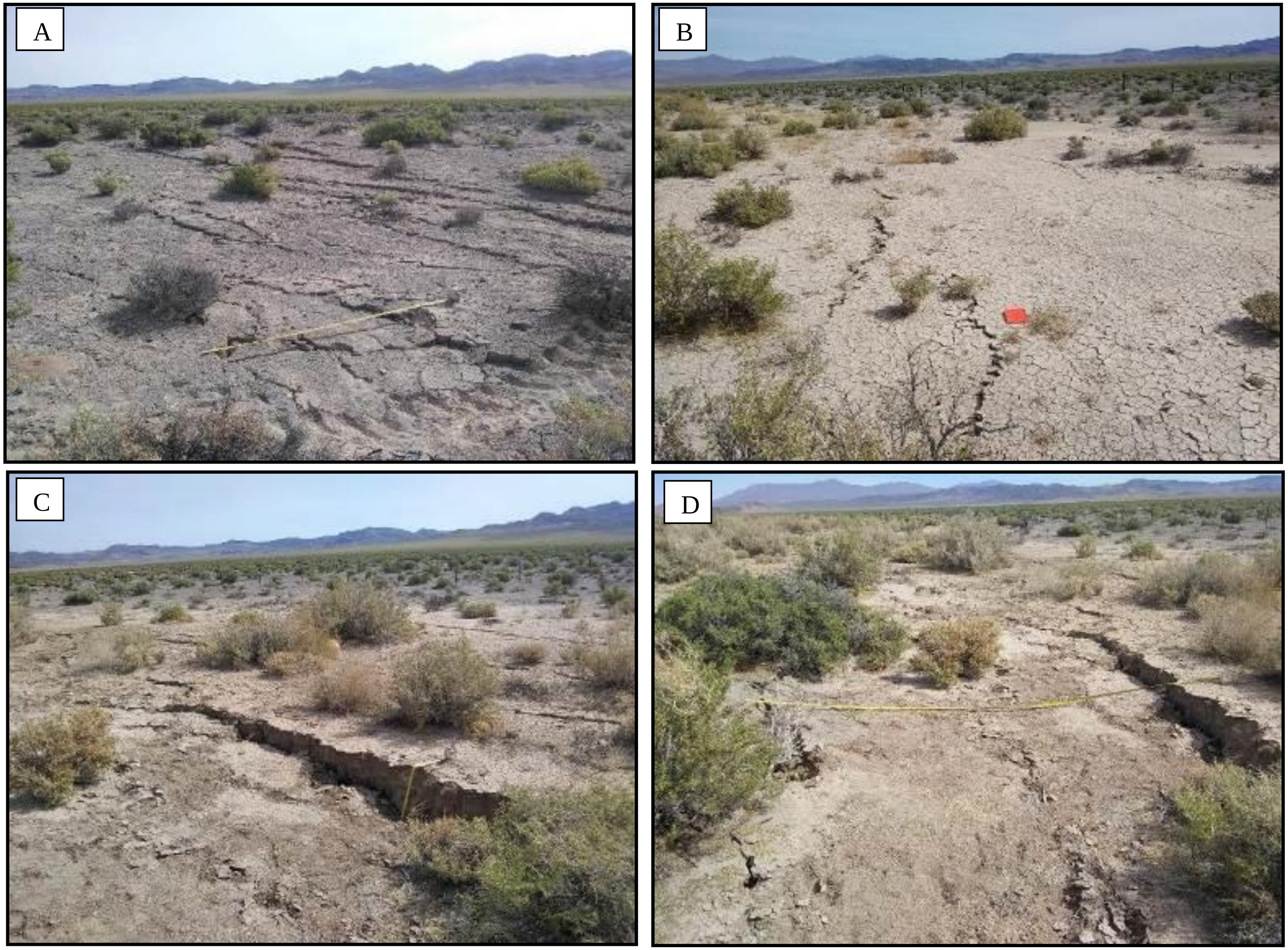
A
B
C
D

Figure 10. Field photos of radial fractures along Highway 95. A) An image showing the vertical offset and width of micro-grabens. B) This image is of fractures that propagate to the northeast. C) This image shows a fracture with 14 cm of vertical offset on the south side of a micro-graben and D) shows the whole graben.

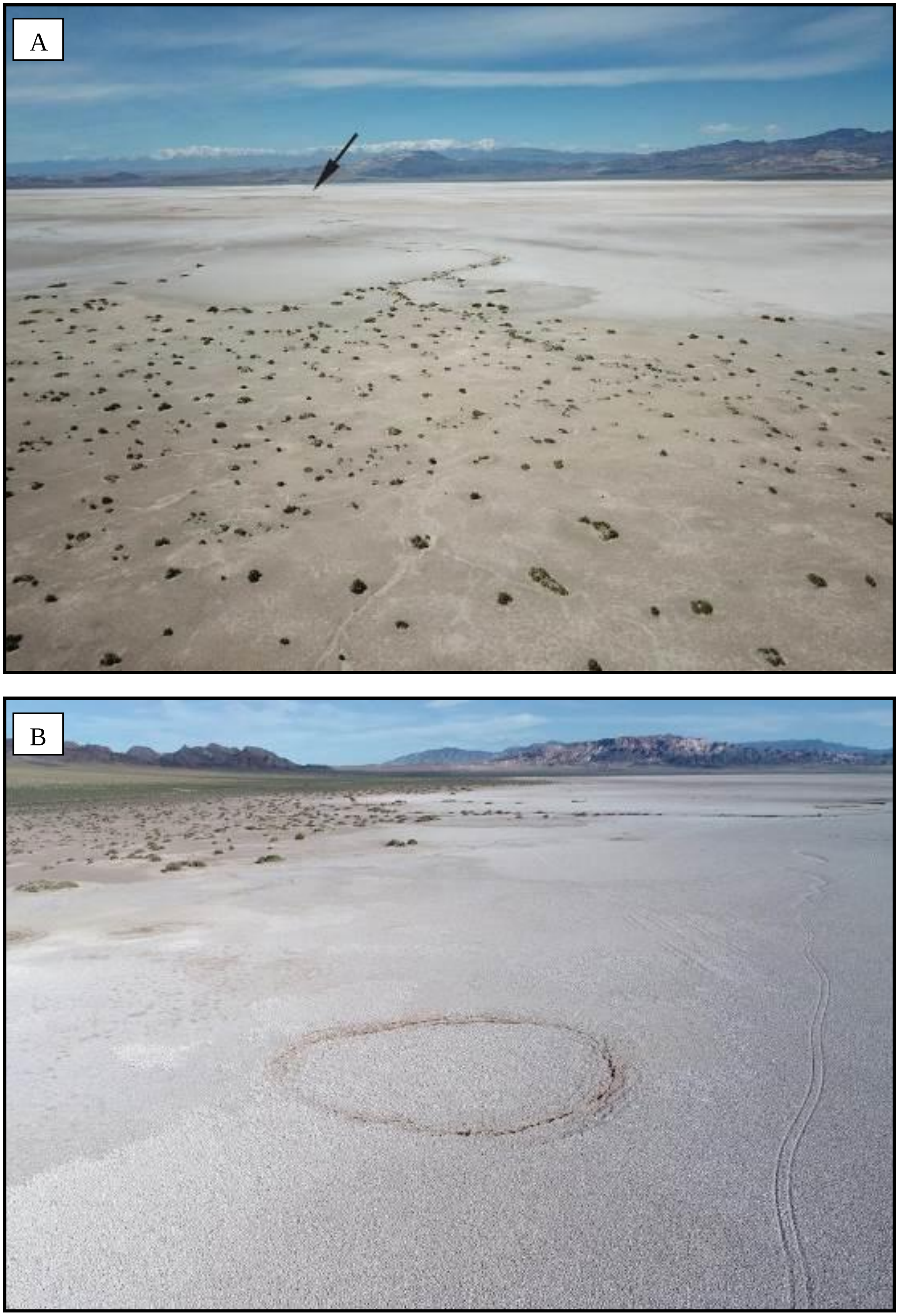
A
B

Figure 11. UAV aerial images of liquefaction features taken along the western side of Highway 95 in the Columbus Salt Marsh. A) The black arrow is pointing to a radial liquefaction feature associated with the Monte Cristo Range earthquake. B) This image shows a close-up of the radial liquefaction feature.

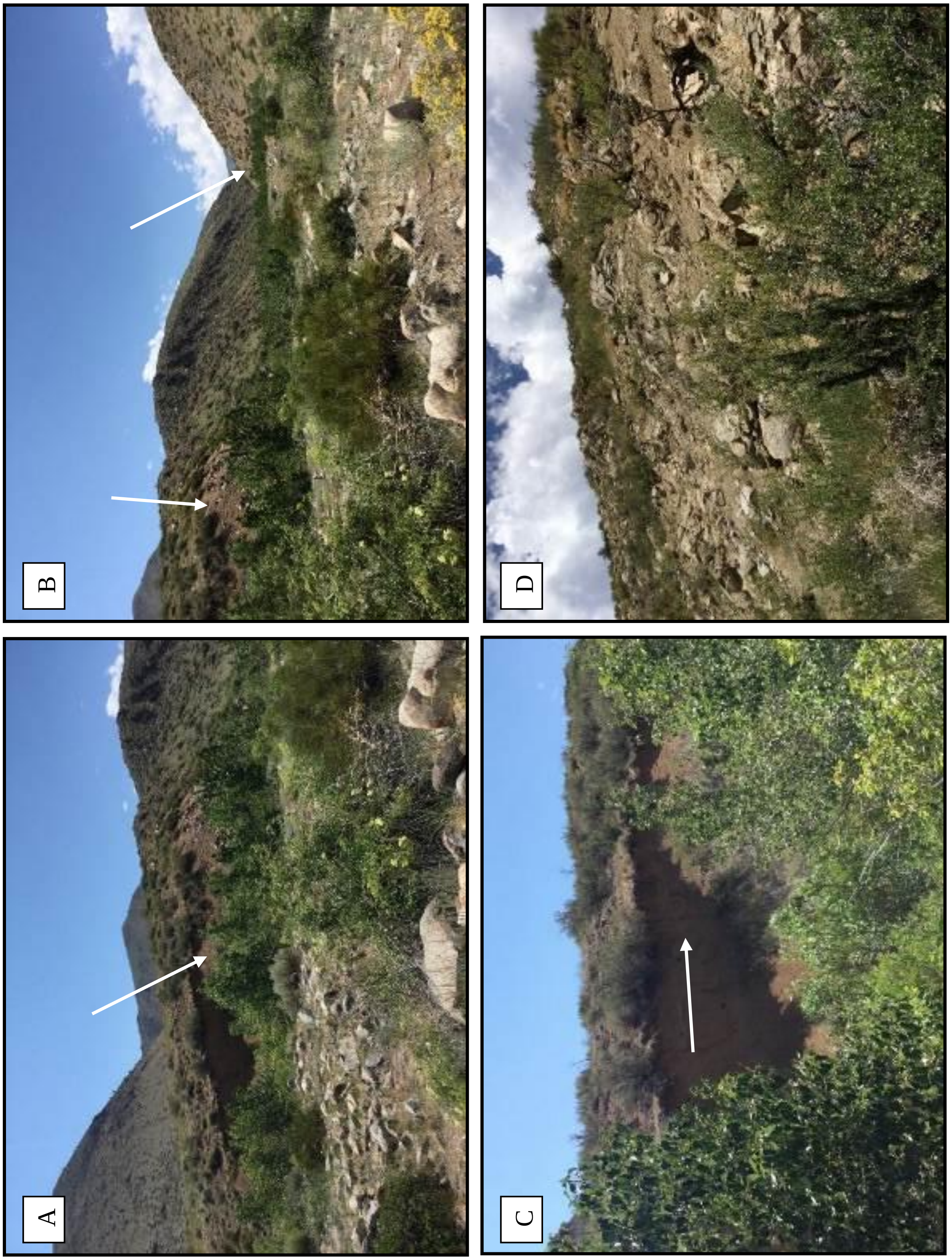
A
B
C
D

Figure 12. Evidence of surface movement in Mill Creek Canyon. A) Image shows recent sloughing of the south side wall of Mill Creek Canyon located at the end of Mill Creek Rd. The owner of the property said he saw a large dirt cloud come from this spot after he exited the house once shaking stopped. He did not have any rock falls near his house, but observed multiple dust clouds from landslides in the creek canyon. B) The left arrow points to a disturbed slope near the sloughing of the south side of Mill Creek. The right arrow points to where the homeowner observed the landslide dust cloud from the north wall of the Canyon. C) The arrow pointing to the scarp in this image shows a close-up of the recent slumping and sloughing of the south side wall of Mill Creek. This is at the mouth of the canyon opening into Antelope Valley. D) This image shows the location where the “dust cloud” landslide occurred on the north wall of Mill Creek Canyon.

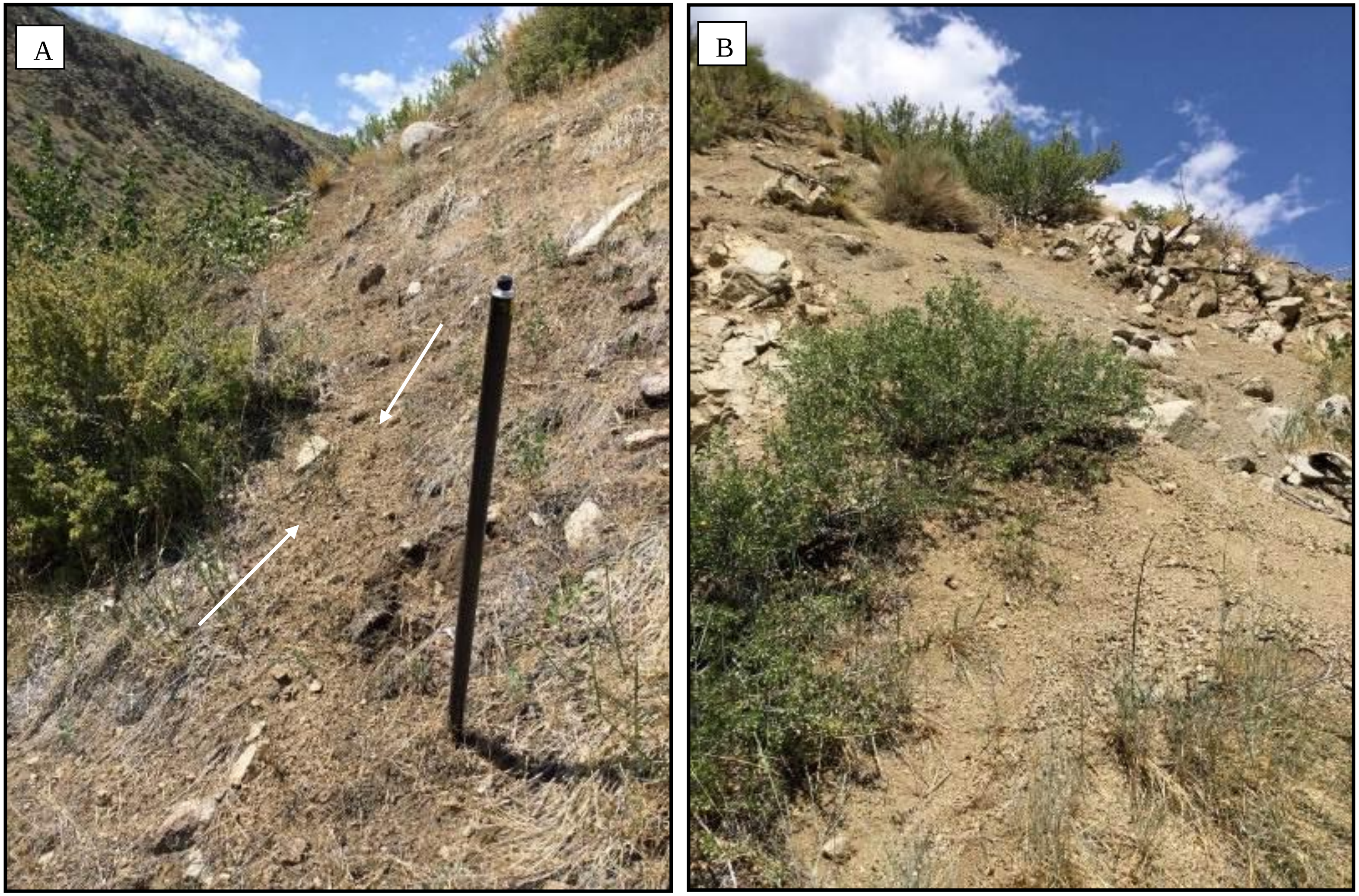

Figure 13. A) The arrows in this image are pointing to a freshly disturbed surface located on the north wall of Mill Creek Canyon. B) This is a close-up image of the landslide on the north side of the canyon wall from Figure 12B.

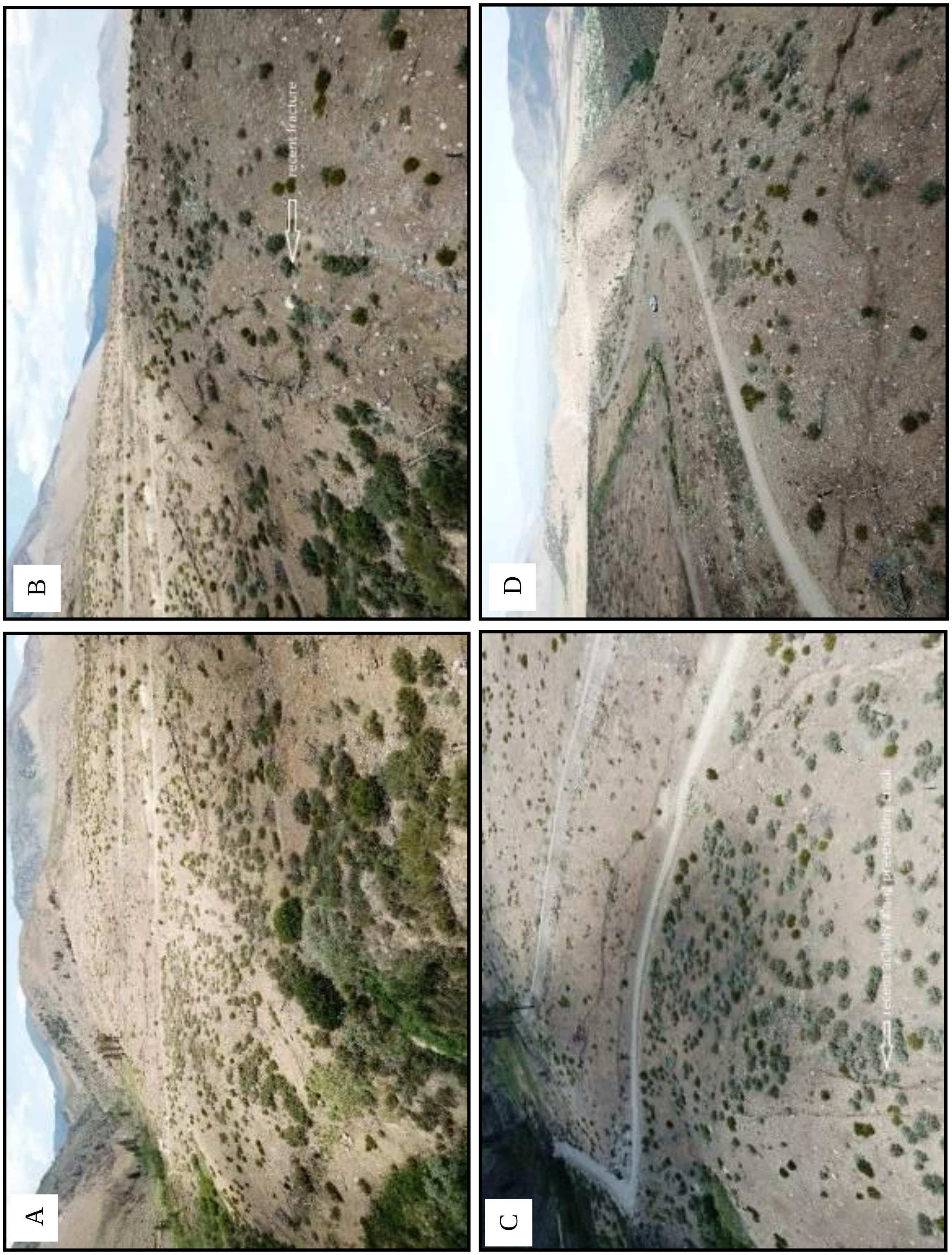
A
B
C
D
recent fracture
recent activity along pre-existing fault

Figure 14. Oblique view drone images of the "old landslide". A) Image of the canyon wall where the 'old landslide' reactivated, view to the northwest. B) Northeast fractures along landslide scarp showing recent fracturing. C) Plan view of pre-existing cracks within the "old landslide" that show evidence for reactivation. D) Plan view looking towards the eastern side of the landslide scarp.

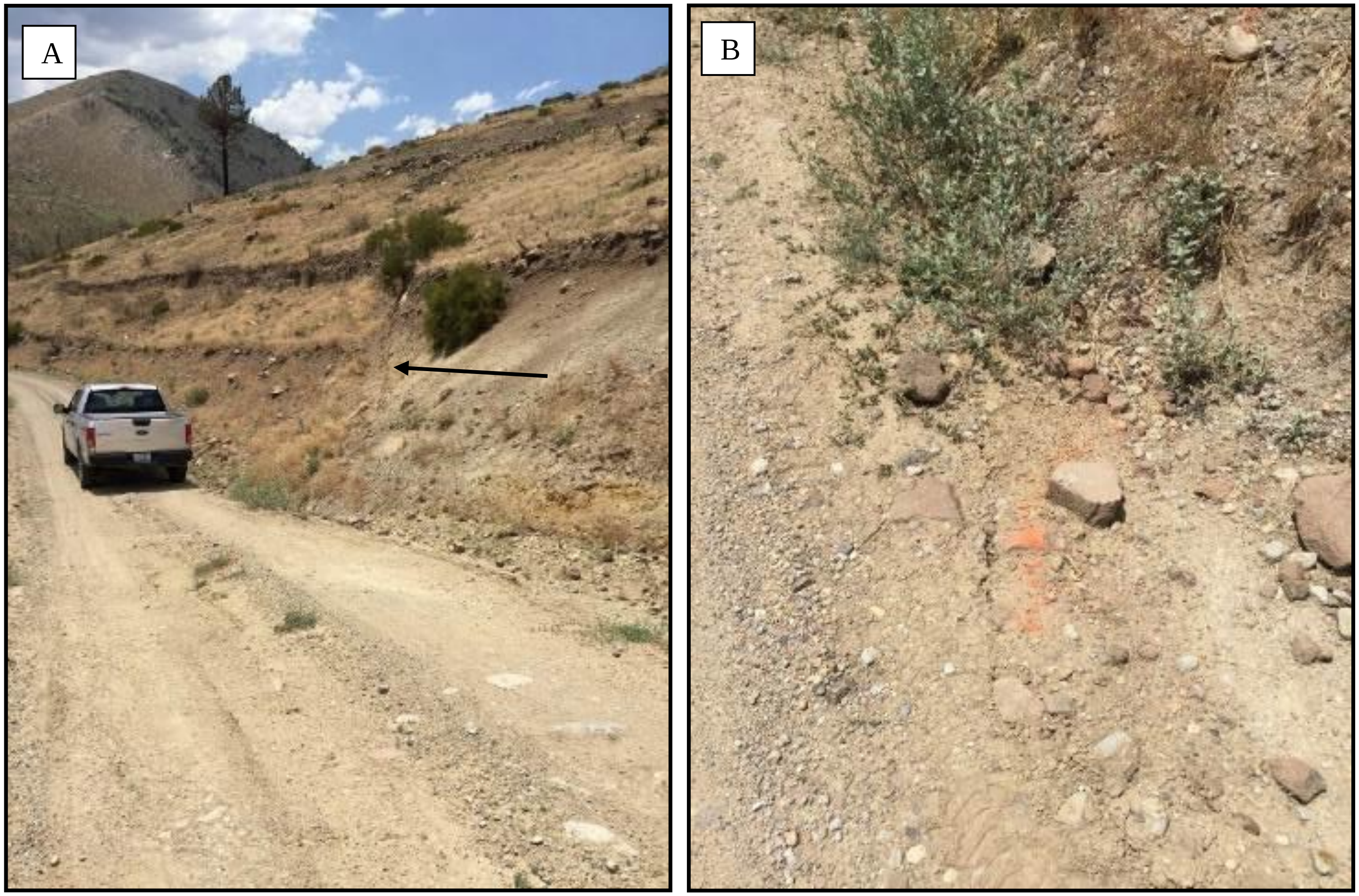

Figure 15. A) The black arrow is pointing to freshly disturbed soil along an older landslide scarp. B) Spray paint marks the length of an old fracture that has lengthened since the paint was applied. Age of paint is unknown.

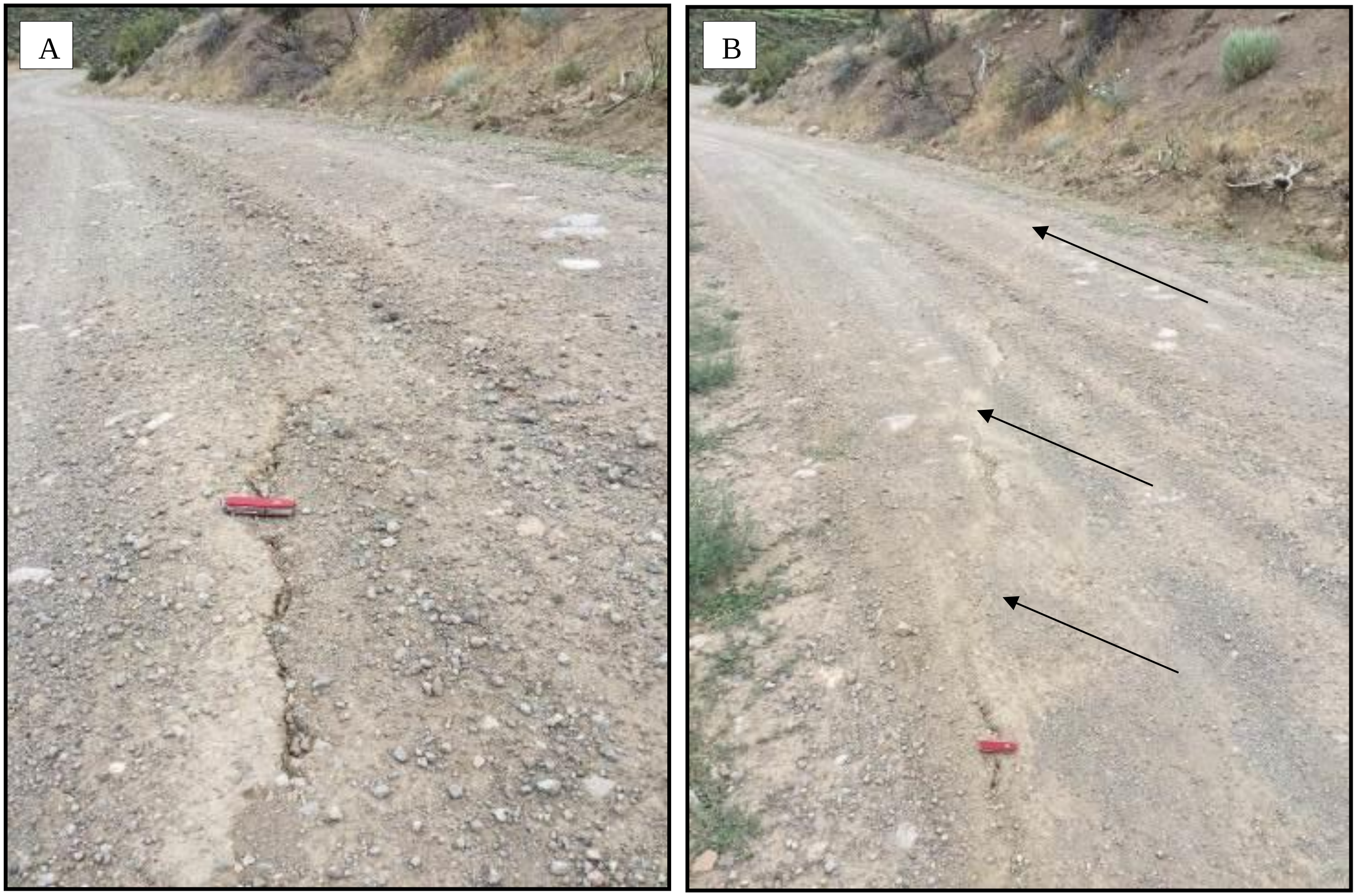

Figure 16. Pictures taken along the dirt road that goes through the “old landslide”. A) The pocketknife is placed across a fracture that has recent vertical movement. B) This image shows the length of the fracture across the road. Black arrows are pointing to the fracture. This fracture is just below the truck in Figure 15A.

Table 1. Monte Cristo Range Earthquake UAV survey

Ground control points	Latitude	Longitude	Altitude (m)	Horizontal error (±) cm	Vertical error (±) cm
GCP01	38.147905°	-117.937447°	1373	20	30
GCP02	38.148889°	-117.938083°	1374	20	30
GCP03	38.148585°	-117.936849°	1375	20	30
GCP04	38.149562°	-117.937722°	1375	20	30
GCP05	38.149468°	-117.935841°	1377	20	30
GCP06	38.151022°	-117.936828°	1377	20	30
GCP07	38.151431°	-117.936124°	1378	20	30
GCP08	38.152184°	-117.936858°	1378	20	30
GCP09	38.152884°	-117.936161°	1379	20	30
GCP10	38.153689°	-117.937100°	1380	20	30
GCP11	38.153713°	-117.936481°	1380	20	30

Appendix C.
Expanded OSL methods and results from the Petersen Mountain fault paleoseismic trench study from Chapter 1

Appendix C.
Expanded OSL methods and results from the Petersen Mountain fault paleoseismic trench study from Chapter 1

1. Introduction and Background

In paleoseismic studies, optically stimulated luminescence (OSL) ages obtained for stratigraphic deposits have been used to determine the estimated timing of fault displacement, slip rates, and earthquake recurrence intervals (Rittenour, 2008; Rhodes, 2011; McAuliffe et al., 2013; Fattahi, 2014). Currently, the most widely used method for luminescence geochronology in Quaternary research is quartz single aliquot regenerative dose (SAR) OSL because quartz is easily bleached (Godfrey-Smith et al., 1988; Gray et al., 2015), provides accurate age results (Murray and Wintle 2000; Wintle and Murray, 2006), and because the SAR method provides an easily modified procedure for multiple luminescence measurements (Rhodes, 2011). OSL provides an estimate of the time passed since the last exposure of sand and silt grains to sunlight, which is assumed to have occurred during sediment transport (Gray et al., 2015). Therefore, OSL ages represents the time of deposition of the sediment or transport event of interest. Gray et al., (2015) describes in more detail luminescence methods and how their application in paleoseismology has evolved over the past three decades. This appendix expands on the OSL methods and results from the Petersen Mountain fault paleoseismic trench study found in Chapter 1.

2. Methods

2.1. Field collection methods

A trench excavated across the Petersen Mountain fault for a paleoseismic study provided an exposure of stacked alluvial fan stratigraphy (De Masi et al., 2021). Six units were selected from both walls of the trench for OSL analyses to evaluate differences in the age of the stratigraphic units. Quartz sand was targeted as it was abundantly distributed throughout the trench and on both sides of the fault zone. Detailed soil and sedimentary descriptions were conducted for individual stratigraphic units exposed in the trench. The thickness, color, grain size, and structure were recorded, and cross sections were made of both sides of the trench to document the stratigraphic relations.

Stratigraphic units sampled from the trench exposure include Units 1, 2, 3, 4, and 8 (Figure C1) (De Masi et al., 2021). Samples were collected by tube and block sampling procedures in areas void of bioturbation to the best extent possible following Gray et al. (2015) (Figure C2and C3). The samples were collected and handled to minimize light exposure during transport.

2.2. Laboratory procedure methods

Lab preparation and data analyses were completed at the Desert Research Institute Luminescence Laboratory (DRILL). All preparatory analyses were conducted in the darkroom under red safelights appropriate for luminescence measurements (Figure C4). Light exposed portions of samples were removed and used for dose rate measurements. The samples were chemically treated with 10% HCl to remove carbonates, rinsed, and then treated with 30% H2O2 to remove organic material. Samples were sieved to isolate 180-250 µm sized quartz grains, dried, and then the magnetic portion was removed. Quartz was isolated from the sediment sample using a solution of Lithium heteropolytungstate and then treated with hydrofluoric acid to remove the outer α-irradiated rim of the grains.

2.3. Analysis

Bulk samples collected from the light-exposed end of the sample tubes were used to determine the background radiation dose rate. Dose rates were determined by measuring elemental concentrations of U, Th, and K via ICP-MS/AES from ~20 g of sample milled to powder consistency. These were sent to ALS Geochemistry in Reno, Nevada for analysis. The values from the dose rate measurements were used to calculate the age.

Sample OSL measurements were performed using an automated Risø TL-DA-20 luminescence reader fitted with a 7 mm-thick Hoya U-340 UV transmitting filter. Samples were measured using a modified single-aliquot regenerative-dose (SAR) protocol with an IR check (Murray and Wintle, 2000; Duller, 2003) (Table A1) on quartz grains in a 4 mm aliquot mounted on stainless steel discs. Dose recovery tests were performed with different preheat temperatures ranging from 160 to 300°C on 12 aliquots from two samples (PMF001 and PMF006) in order to test the reliability of the modified SAR protocol and determine the optimal preheat temperature for OSL measurement (Murray and Wintle, 2003) (Figure C5). A preheat temperature of 240°C and a cut heat temperature of 160°C produced a dose closest to the given dose and was used in subsequent D_e measurements.

2.4. Age models

Age models run in R Language using the Luminescence package version 0.9.3 were applied to determine the appropriate D_e for age calculation (Kreutzer et al, 2019). Sample equivalent dose was modeled using the central age model (CAM) (Galbraith et al., 1999) and minimum age model (MAM) (Galbraith and Laslett, 1993). Modeled D_e was then entered into the Dose Rate and Age Calculator for trapped charge dating (DRAC) by Durcan et al. (2015) to calculate an age.

3. Results

OSL testing showed that samples were able to reproduce a given dose using the SAR protocol. The OSL signals were bright and dominated by the fast component (Figure C6A). Growth curves had an early saturating component ranging from ~1 to 100 dose seconds and a slow saturating component from ~300 to 500 dose seconds (Figure C6B). A mean recycling ratio of 0.99 ± .04 support the use of the SAR protocol applied to these samples. A representation of D_e distributions for sample PMF004 are displayed in the kernel density and radial plots presented in Figure C7.

MAM was applied to sample PMF001 based on a high overdispersion initially run with the central age model. All other samples had less than 20% overdispersion and CAM was used. Locations of samples are shown with OSL ages on the fault trench log in Figure C1. The age results from these models are shown in Table C2.

Age results aligned with expected Pleistocene age of ~30 ka for samples PMF002, PMF004, PMF005, and PMF006 which were dated at 28 ka, 32 ka, 28 ka, and 20 ka respectively. Partial bleaching and mixing with modern soil are assumed for units that contained samples PMF001 and PMF003. Sample PMF001 was collected in the fine sand of Unit 8 (Figure C1) suggesting a sheet wash- alluvial fan environment which is consistent with field observations. Sample PMF003 was collected at the base of Unit 4 (Figure C1), a sandy soil close to the surface which would be consistent with bioturbation at an earlier ground surface. The extremely young age of ~3 ka for sample PMF003 is likely a result of partial bleaching related to mixing in the pedoturbation zone.

The ~10-20 ka age determined for the sandy alluvial deposits near the surface (but beneath the pedoturbation zone) in both the footwall and hanging wall suggests a late Pleistocene age for the surfaces. This age is consistent with the geomorphic characteristics of the surface and ages for other intermediate Qfi alluvial fan deposits in the region (Dee et. al., 2018; Chupik et al, 2021).

4. Discussion and Conclusion

Results show that there is some degree of variability in OSL ages depending on where the sample was collected within the alluvial unit. Sample PMF003 was collected in the hanging wall near the basal contact of a sandy soil approximately 40 cm from the top surface of the trench. For this study, that places the sample within the pedoturbation zone and has been affected by mixing of partially bleached grains likely related to bioturbation and particle infiltration from the overlying units from surface water during rain events (Bateman et al., 2003) yielding a false young age of ~3 ka.

Sample PMF001 was collected in the footwall at a depth of ~1.25 m from the surface of the trench in fine sand mimicking that of a large sheet wash event that likely results in the observed distribution of De which appears to show partial bleaching. This could also be the case for sample PMF006 at an OSL age of ~20, which is at similar depths to sample PMF001 at ~10 ka but on opposing walls of the fault scarp.

The OSL age of sample PMF001 from Unit 8 on the footwall was compared to the OSL ages of PMF006 from Unit 3 and PMF004 from Unit 2 on the hanging wall. As previously stated, PMF001 was collected at a depth of ~1.25 m. Sample PMF006 was collected at a depth of ~0.7 m and PMF004 was collected at a depth of ~1.65 m. The OSL ages are vastly older for the samples collected in the units on the hanging wall with PMF006 at an age of ~20 ka and PMF004 at an age of ~32 ka.

Acknowledgements

I thank Amanda Keen-Zebert and Cristina Neudorf of the Desert Research Institute E.L. Cord Luminescence Laboratory for assisting me in the lab. Funding was provided through USGS NEHRP Cooperative Agreement G18AP00007.

References

Adamiec, G., and Aitken, M.J., 1998, Dose-rate conversion factors–update: Ancient TL, v. 16, no. 2, p. 37-50.

Aitken, M.J., Tite, M.S. & Reid, J., 1963, Thermoluminescent dating: progress report, Archaeometry, 6, 65–75p. doi:10.1111/j.1475-4754.1963.tb00581.x.

Bailiff, I. K. ,2007. Methodological developments in the luminescence dating of brick from English late-medieval and post-medieval buildings. Archaeometry 49, 827-851.

Barnett, S.M., 2000. Luminescence dating of pottery from later prehistoric Britain. Archaeometry 42, 431-457.

Bateman, M.D., Frederick, C.D., Jaiswal, M.K., and Singhvi, A.K., 2003, Investigations into the potential effects of pedoturbation on luminescence dating: Quaternary Science Reviews, v. 22, no. 10, p. 1169-1176.

Bateman, M.D., Boulter, C.H., Carr, A.S., Frederick, C.D., Peter, D., and Wilder, M., 2007, Detecting post-depositional sediment disturbance in sandy deposits using optical luminescence. Quaternary Geochronology 2, 57–64.

Chupik, C., Koehler, R., and Keen-Zebert, A., 2021, Complex Holocene Fault Ruptures on the Warm Springs Valley Fault in the Northern Walker Lane, Nevada–Northern California. *Bulletin of the Seismological Society of America* 2021; doi:https://doi.org/10.1785/0120200271.

Dee, S., Ramelli, A.R., and Koehler, R.D., 2018, Pilot paleoseismic investigation of faults in the North Valleys, Reno, NV, Final Technical Report, U.S. Geological Survey National Earthquake Hazards Reduction Program (Award # G16AP00060).

Dee, S., 2019, Preliminary geologic map of the Granite Peak quadrangle, Washoe County, Nevada: Nevada Bureau of Mines and Geology Open-File Report 19-2, 1:24,000 scale, X p.

Duller, G.A.T., 2003, Distinguishing quartz and feldspar in single grain luminescence measurements. Radiat. Meas. 37, 161–165.

DuRoss, C.B., Personius, S.F., Crone, A.J., Olig, S.S., and Lund, W.R., 2011, Integration of paleoseismic data from multiple sites to develop an objective earthquake chronology–Application to the Weber segment of the Wasatch fault zone: Bulletin of the Seismological Society of America, v. 101, p. 2765–2781.

Durcan, J.A., King, G.E., Duller, G.A.T., 2015, DRAC: Dose rate and age calculator for trapped charge dating. Quaternary Geochronology, 28, 54-61. doi:10.1016/j.quageo.2015.03.012.

Fattahi, M., 2014, Luminescence, earthquake, and tectonic activity, *in* Rink, J.W., and Thomas, J., editors, Encyclopedia of scientific dating methods: Springer, p. 1-8.

Galbraith RF and Laslett GM, 1993, Statistical models for mixed fission track ages. Nuclear Tracks and Radiation Measurements 21: 459–470, DOI 10.1016/1359-0189(93)90185-C.

Galbraith, R. F., Roberts, R. G., Laslett, G. M., Yoshida, H., and Olley, J. M., 1999. Optical dating of single and multiple grains of quartz from Jinmium rock shelter, northern Australia: part I, experimental design and statistical models. *Archaeometry*, **41**, 339–364.

Galbraith, R.F., and Roberts, R.G., 2012, Statistical aspects of equivalent dose and error calculations and display in OSL dating—An overview and some recommendations: Quaternary Geochronology, v. 11, p. 1-27.

Godfrey-Smith, D.I., Huntley D.J., and Chen, W.H., 1988, Optical dating studies of quartz and feldspar sediment extracts: Quaternary Science Reviews, v. 7, p. 373–380.

Gray, H.J., Mahan, S.A., Rittenour, T., and Nelson, M.S., 2015, Guide to luminescence dating techniques and their application for paleoseismic research, In: Lund, W.R. (ed.), 2015, Proceedings volume, Basin and Range Province Seismic Hazards Summit III, Utah Geological Survey, Miscellaneous Publication 15-5.

Huntley, D.J., Godfrey-Smith, D.I., and Thewalt, M.L.W., 1985, Optical dating of sediments, Nature, 313 (5998): 105–107.

Jain, M., Murray, A.S., and, Botter-Jensen, L., 2004, Optically stimulated luminescence dating: how significant is incomplete light exposure in fluvial environments. Quaternaire, v. 15, no. 1, p. 143-157.

Keen-Zebert, A., Tooth, S., Rodnight H., Duller, G.A.T., Roberts, H.R., Grenfell, M., 2013, Late Quaternary floodplain reworking and the preservation of alluvial sedimentary archives in unconfined and confined valleys of mixed bedrock-alluvial rivers in the eastern interior of South Africa. Geomorphology 185: 54-66.

Keen-Zebert, A., 2015, Luminescence, Fluvial Sediments. In Rink, W.J., Thompson, J.W. (Eds.) Encyclopedia of Scientific Dating Methods, Springer-Verlag, Berlin-Heidelberg. 465-469. doi:10.1007/978-94-007-6326-5_3-1.

Kreutzer, S., Burow, C., Dietze, M., Fuchs, M., Schmidt, C., Fischer, M., Friedrich, J., Mercier, N., Smedley, R.K., Christophe, C., Zink, A., Durcan, J., King, G.E., Philippe, A., Guerin, G., Riedesel, S., Autzen, M., Guibert, P., and Fuchs, M., 2019, *Luminescence: Comprehensive Luminescence Dating Data Analysis*. R package version 0.9.3.

Liritzis, I., Stamoulis, K., Papachristodoulou, C., and Ioannides, K., 2013, A re-evaluation of radiation dose-rate conversion factors. Mediterranean Archaeology and Archaeometry, 13, 1-15.

Long, Hao & Lai, ZhongPing & Wang, NaiAng & Zhang, Jingran., 2011, A combined luminescence and radiocarbon dating study of Holocene lacustrine sediments from arid northern China. Quaternary Geochronology. 6. 1-9. 10.1016/j.quageo.2010.06.001.

McAuliffe, L.J., Dolan, J.F., Kirby, E., Rollins, C., Haravitch, B., Alm, S., and Rittenour, T.M., 2013, Paleoseismology of the southern Panamint Valley fault—Implications for regional earthquake occurrence and seismic hazard in southern California: Journal of Geophysical Research—Solid Earth, v. 118, p. 5126-5146.

Murray, A.S., Olley, J., and Caitcheon, G.G., 1995, Measurement of equivalent doses in quartz from contemporary water-lain sediments using optically stimulated luminescence. Quat. Sci. Rev. 14, 365–371.

Murray, A.S., Olley, J.M., 2002, Precision and accuracy in the optically stimulated luminescence dating of sedimentary quartz: a status review. *Geochronometria* 21:1–16

Murray, A.S., Wintle, A.G., 2000, Luminescence dating of quartz using an improved single-aliquot regenerative-dose protocol. Radiat. Meas. 32, 57–73.

Murray, A.S., Wintle, A.G., 2003, The single aliquot regenerative dose protocol: potential for improvements in reliability. Radiat. Meas. 37, 377–381.

Nelson, M.S., and Rittenour , T. M., 2015, Using Grain-size Characteristics to Model Soil Water Content: Application to Dose-rate Calculation for Luminescence Dating. Radiation Measurements, doi.org/10.1016/j.radmeas.2015.02.016

Olley, J.M., Caitcheon, G.G., and Roberts, R.G., 1999, The origin of dose distributions in fluvial sediments, and the prospect of dating single grains from fluvial deposits using optically stimulated luminescence: Radiation Measurements, v. 30, no. 2, p. 207-217.

Prescott, J.R., and Hutton, J.T., 1994, Cosmic ray contributions to dose rates for luminescence and ESR dating: large depths and long-term time variations. Radiation Measurements, 23, 497-500.

Rittenour, T.M., 2008, Luminescence dating of fluvial deposits—Applications to geomorphic, paleoseismic, and archaeological research: Boreas, v. 37, no. 4, p. 613-635.

Rhodes, E.J., Bronk-Ramsey, C., Outram, Z., Batt, C., and Willis, L., 2003, Bayesian methods applied to the interpretation of multiple OSL dates: high precision sediment age estimates from Old Scatness Broch excavations, Shetland Isles. *Quat. Sci. Rev.* 22:1231–44.

Rhodes, E.J., 2011, Optically stimulated luminescence dating of sediments over the past 200,000 years: Annual Review of Earth and Planetary Sciences, Annual Reviews, v. 39, p. 461-488, doi: 10.1146/annurev-earth-040610-133425.

Rodrigues, K., Rink, W.J., Collins, M.B., Williams, T.J., Keen-Zebert, A., and Lopez, G.I., 2016, OSL ages of the Clovis, Late Paleoindian and Archaic components at Area 15 of the Gault Site, Central Texas, U.S.A. Journal of Archaeological Science Reports 7: 94-103. doi:10.1016/j.jasrep.2016.03.014

Wintle, A.G., and Murray, A.S., 2006, A review of quartz optically stimulated luminescence characteristics and their relevance in single-aliquot regeneration dating protocols. Radiat. Meas. 41, 369–391.

FIGURES

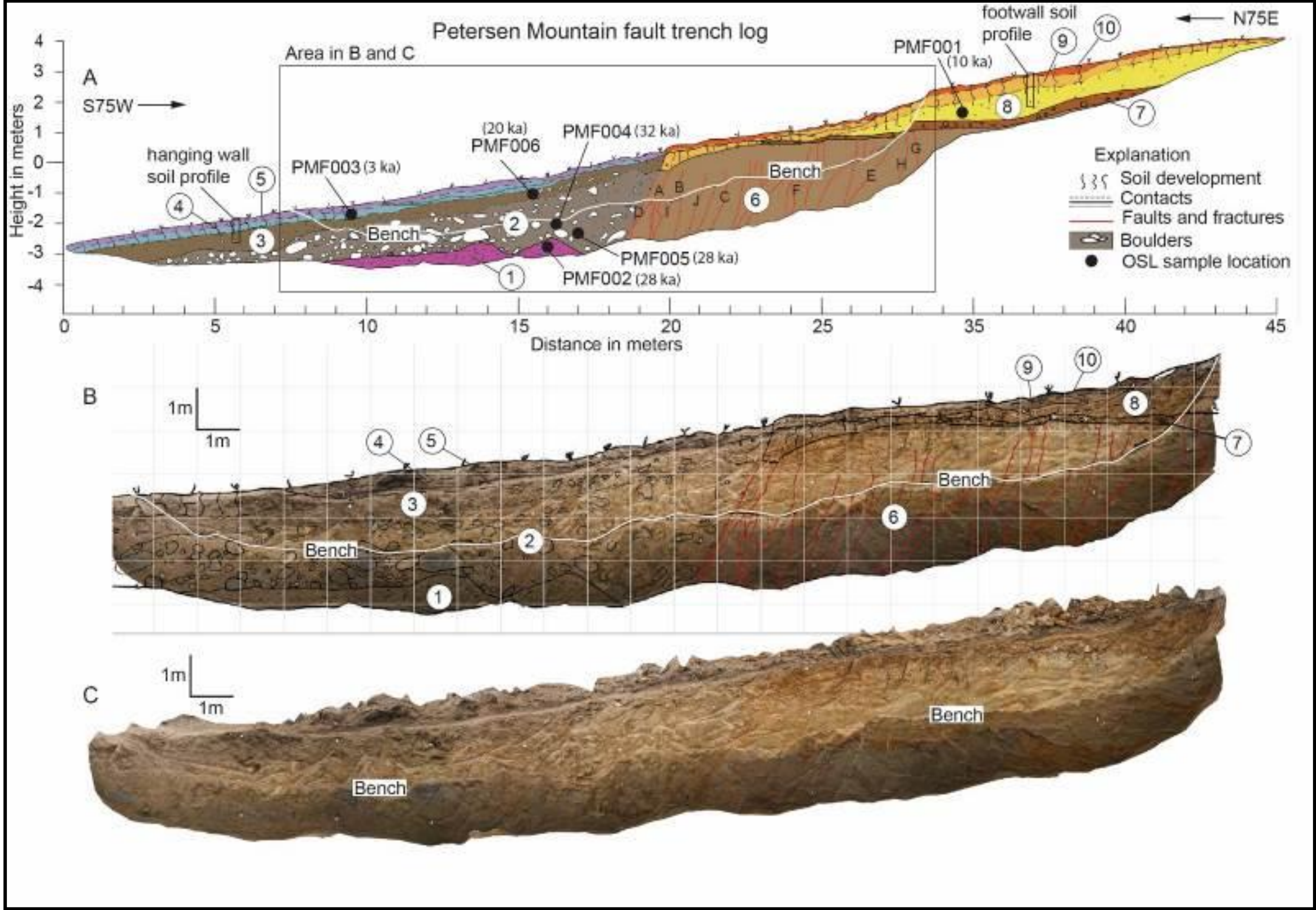
Petersen Mountain fault trench log
A
S75W
N75E
Area in B and C
Height in meters
Distance in meters
hanging wall soil profile
footwall soil profile
PMF001 (10 ka)
PMF002 (28 ka)
PMF003 (3 ka)
PMF004 (32 ka)
PMF005 (28 ka)
PMF006 (20 ka)
Bench
1
2
3
4
5
6
7
8
9
10
A B C D E F G H I J
Explanation
Soil development
Contacts
Faults and fractures
Boulders
OSL sample location
B
C
1m
1m

Figure C1. A) Log of Petersen Mountain trench exposure (south wall) showing stratigraphic and structural relations. Open circles show unit numbers, solid black circles are OSL samples, and letters are fracture attitude locations. Black box outlines figures A1B and A1C. B) Interpreted photomosaic. C) Uninterpreted photomosaic.
(Figure modified from De Masi et al., 2021)

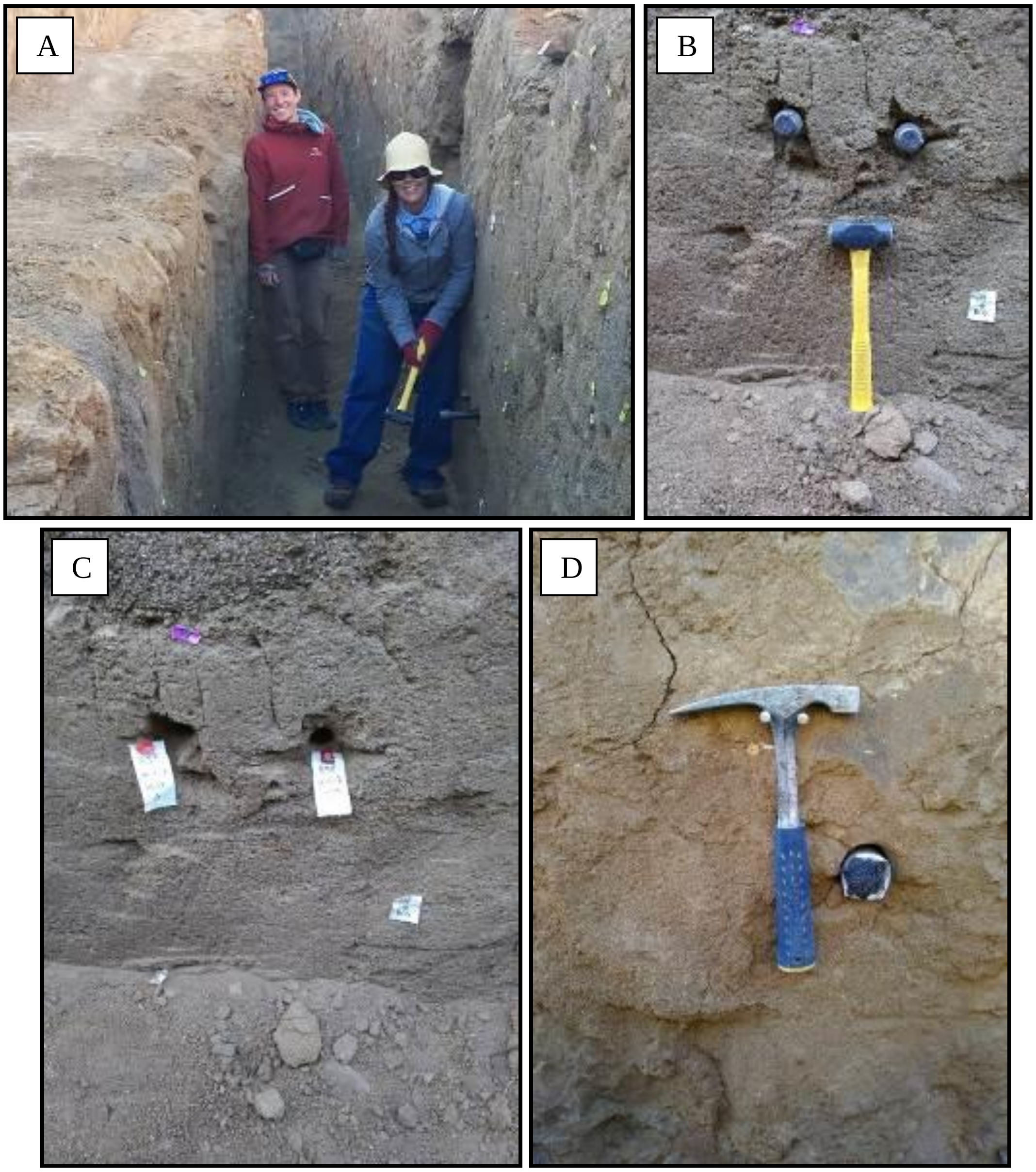

Figure C2. Photographs of OSL sample collection. A) Hammering in tube. B) Two collection tubes hammered and sealed before removal. C) Sample site after tube removal. D) Sample collected in cemented sand.

Figure C3. Photographs of OSL block sample collection. A) Using the electric hand saw to cut out block sample. B) Measuring height of collection to surface. C) Measuring size of block. D) Covering sample with 4 mil light proof plastic.

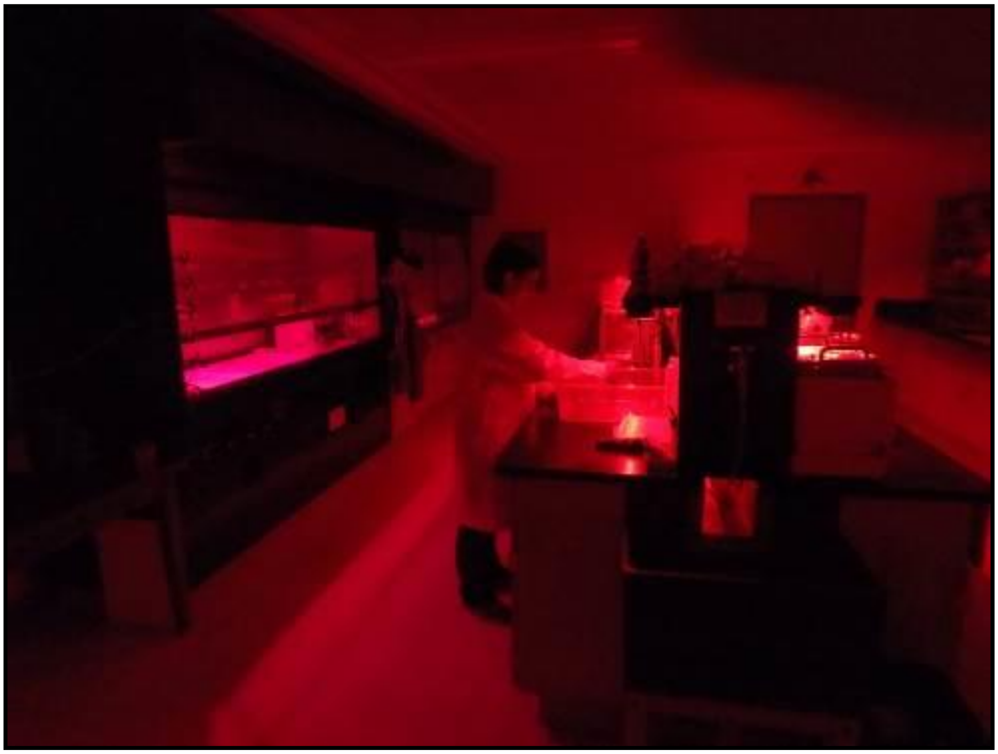

Figure C4. Laboratory procedures were performed in a red safelight darkroom at the DRI Luminesce Laboratory in Reno, NV.

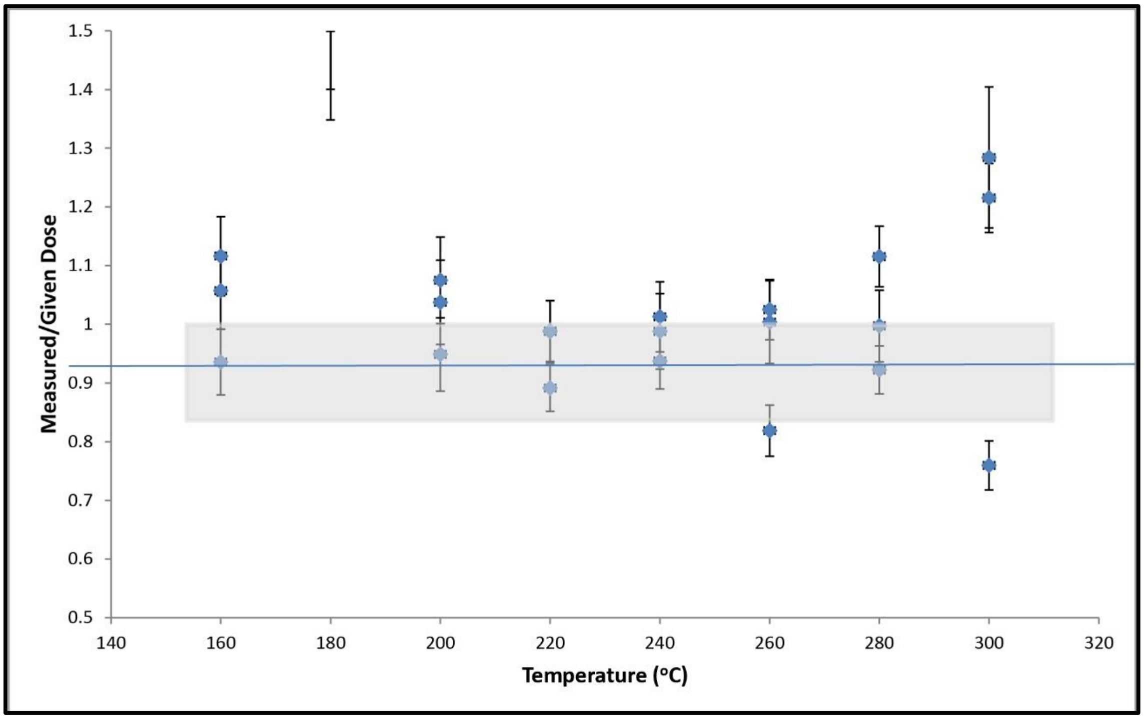

Figure C5. Results of dose recovery at varied preheat temperatures from sample PMF006.

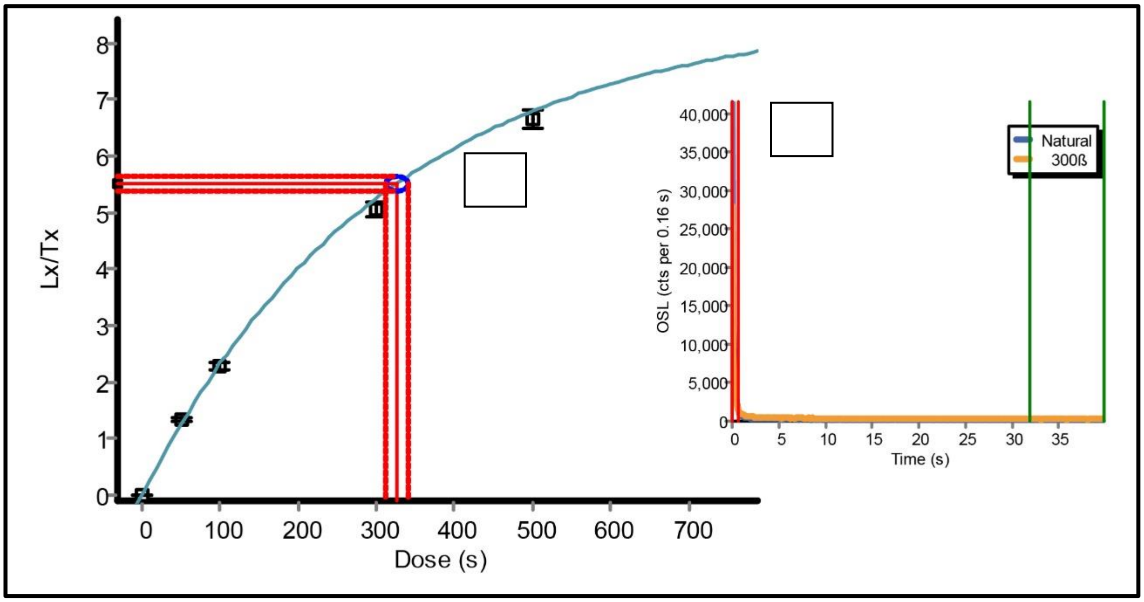

Figure C6. Representative dose response curve (A) and decay curve (B) for sample PMF006.

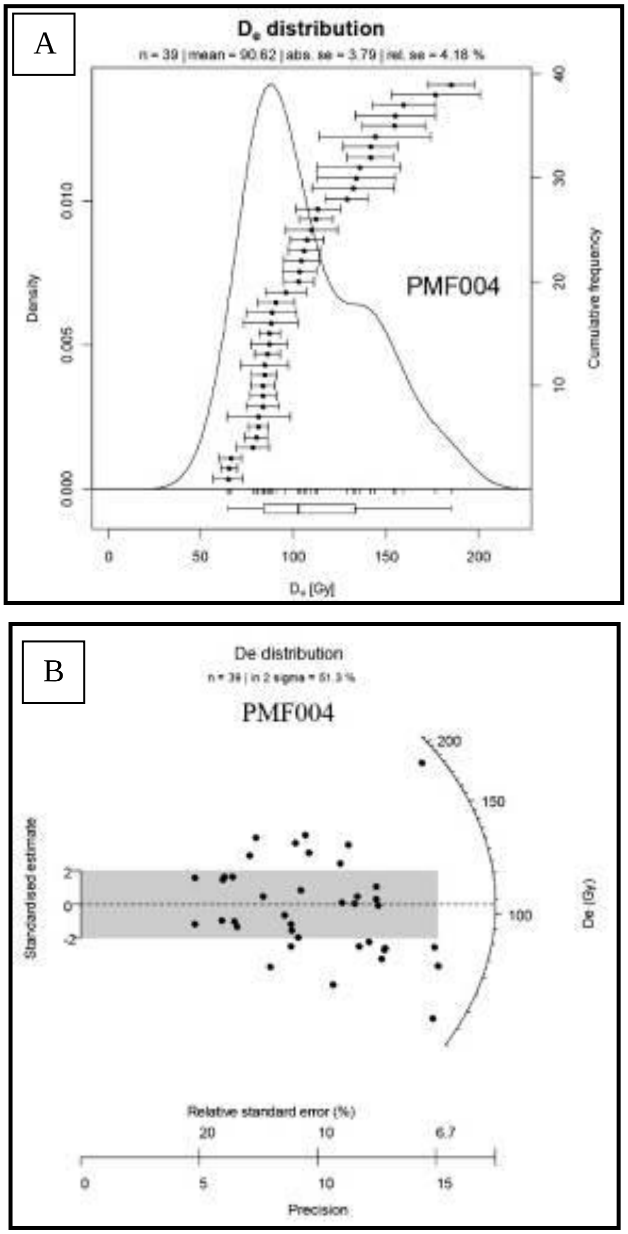

Figure C7. KDE (A) and Radial plot (B) for sample PMF004.

Table C1. SAR protocols applied in this study.

Step	OSL SAR protocol
1	Natural/Regenerative Dose
2	Preheat (240^{o}C, 10 s)
3	Blue (470 nm) LED Diodes (125^{o}C, 100 s)
4	Test Dose (100 Gy s)
5	Cut Heat (160^{o}C, 0 s)
6	Blue (470 nm) LED Diodes (125^{o}C, 100 s)
7	Hot Wash Blue (470 nm) LED Diodes (260^{o}C, 40 s)
8	Return to step 1.

Table C2. OSL age data. Samples were collected at 39.7828° N, 119.9411° W at elevation 2535 m.

Sample number	Trench unit	Depth (m)	N accepted (N analyzed)[a]	Over-dispersion (%)	CAM D_b (Gy)[b]	U (ppm)[c]	Th (ppm)[c]	K (%)[c]	External beta dose rate wet (Gy/ka)	External gamma dose rate wet (Gy/ka)	Cosmic dose rate (Gy/ka)[d]	Total dose rate (Gy/ka)[e]	Age (ka)[f]
PMF001	8	1.2	23/48	29	55.3 ± 3.64	4.58	14.00	1.15	1.62	1.39	0.30	3.31 ± 0.15	16.71 ± 1.33
PMF002	1	3.0	36/48	22	96.83 ± 4.36	3.54	14.30	1.60	1.82	1.40	0.24	3.46 ± 0.17	27.99 ± 1.84
PMF003	4	0.4	26/48	47	12.23 ± 1.17	3.54	18.05	1.72	1.97	1.60	0.36	3.93 ± 0.19	3.11 ± 0.33
PMF004	2	1.7	39/48	23	103.2 ± 4.6	3.55	13.40	1.43	1.68	1.32	0.28	3.28 ± 0.15	31.48 ± 2.03
PMF005	2	2.3	34/48	8	101.4 ± 2.96	3.95	14.25	1.71	1.93	1.47	0.26	3.67 ± 0.18	27.66 ± 1.55
PMF006	3	0.7	38/38	14	96.92 ± 3.07	4.65	23.60	2.05	2.45	2.05	0.32	4.82 ± 0.23	20.12 ± 1.15

[a] n is the number of D_e determinations accepted after screening; in parentheses are the total number of aliquots measured.

[b] The error shown on the burial dose, D_b, is the error modeled with the central age model (CAM) (Galbraith et al., 1999).

[c] U and Th samples were fused with lithium borate and measured with ICP-MS. K2O was measured on bulk sample with ICP-AES and converted to % K.

[d] Cosmic dose rates (Gy/ka) are calculated according to Prescott and Hutton (1994).

[e] Dose rates (Gy/ka) were calculated using the conversion factors of Liritzis et al. 2013 and are shown rounded to two decimal places; ages were calculated using values prior to rounding; central values are given for dose-rates and errors are incorporated into that given for the total dose-rate. Water content of 5% ± 2.5% was used for all dose rate calculations.

[f] Luminescence ages were calculated using DRACv1.2 (Durcan et al., 2015) and are expressed as thousands of years before 2019 and rounded to the nearest 10 years.

Error is 2 sigma.

FINAL SUMMARY, CONCLUSIONS AND RECOMMENDATIONS

Summary

This dissertation brings together a comprehensive look at geologic hazards in rural areas in the tectonically active Walker Lane and the technology and methods used to analyze them. Studying faults in rural localities creates the opportunity to see how faults interact with other landforms such as alluvial fans and shorelines, which are not preserved in urban environments. Post-earthquake reconnaissance gives us an idea of how these processes affect the local environment and landscape which can be used to understand events of the past. These studies can help answer questions regarding 1) When, why, and how plate tectonics (faults) evolve? 2) Where and when earthquakes occur? 3) What are the differences between fault scarps and shorelines 4) How can Earth science research reduce the risk and toll of geohazards? I summarize the conclusions of the three hazards studies, discuss broader impacts, and suggest directions for future work.

Concluding Remarks

Chapter 1

The Petersen Mountain fault in the northern Walker Lane has been re-characterized as having dextral-oblique slip. Geologic and geomorphic mapping along the fault, and trench study, aided in determining the fault’s style of deformation. The trench exposed the juxtaposition of stratigraphic units across the fault and ages of faulted deposits estimated from OSL analyses indicate the occurrence of at least one earthquake in the late Pleistocene that was associated with lateral displacement on an east dipping fault.

The study concludes that the Petersen Mountain fault accommodates components of both normal and dextral slip, possibly along a pre-existing Basin and Range normal fault system. Quaternary deformation may be related to the development of Riedel shearing that is responding to regional northwest directed shear as part of the Walker Lane tectonic regime. Active deformation along Riedel shears is an important component in the development of youthful or incipient strike-slip fault systems and the Petersen Mountain fault may be an important kinematic link between the Sierra Nevada Frontal Fault system and faults of the northern Walker Lane. More studies could be done along north-oriented youthful fault systems in the Walker Lane to test for a right-lateral slip component to help understand how the North American-Pacific Plate boundary is evolving.

Chapter 2

Fault scarps and shoreline features such as wave-formed terraces can be identified by looking at their morphology and depositional components. In this study we were able to correlate previous studies of the Lake Lahontan late Pleistocene highstands in the region to match tephra bed stratigraphy and highstand elevations along the Smoke Creek channel to constrain the timing of earthquakes along the Bonham Ranch fault in the northern Walker Lane. We compared the results in this study to that of the previous Weick study to determine that at least one earthquake has occurred along the Bonham Ranch fault since ~12 ka and likely since ~3.4 ka. Future paleoseismic trench work is needed to define slip characteristics of the Bonham Ranch fault, and to provide a deeper outcrop for matching tephras from around the Smoke Creek Desert basin to tease out the frequency of earthquakes in the region.

Chapter 3

This chapters highlights the importance of Uncrewed Aerial Systems for post-earthquake rapid response reconnaissance work. Quick review of UAS aerial imagery helps for pin-pointing critical investigation locations after the disaster event. Greater ground distance can be covered in a shorter amount of time, helping cut down on response costs and assists in directing ground crews. Offsite processing of drone data allows for the creation of digital terrain models and photo orthomosaic models which can be used for quantitative analyses.

UASs are helpful in identifying areas near event epicenters that experience surface ruptures, such as for the Mw6.5 Monte Cristo Range earthquake, and those areas that do not, such as the Mw6.0 Antelope Valley earthquake. The reliability of mapping surface deformation with the models depends on pixel resolution. UAV images set at the parameters defined in this study allow for sufficient detail in the models to match the 2 cm or larger surface ruptures that were seen by field ground crews for the Monte Cristo Range event, and to view the recent activity along pre-existing fractures and scarps within the “old landslide” for the Antelope Valley event. More quantitative work needs to be done with drone usage for evaluating damage after a disaster that involves understanding the width of the drone camera and height of the drone during image capture to accurately model and measure objects.